

University of Bath



PHD

First principles calculations of the interaction of rare-gas atoms with transition metal surfaces

Betancourt, Angel E.

Award date:
2000

Awarding institution:
University of Bath

[Link to publication](#)

General rights

Copyright and moral rights for the publications made accessible in the public portal are retained by the authors and/or other copyright owners and it is a condition of accessing publications that users recognise and abide by the legal requirements associated with these rights.

- Users may download and print one copy of any publication from the public portal for the purpose of private study or research.
- You may not further distribute the material or use it for any profit-making activity or commercial gain
- You may freely distribute the URL identifying the publication in the public portal ?

Take down policy

If you believe that this document breaches copyright please contact us providing details, and we will remove access to the work immediately and investigate your claim.

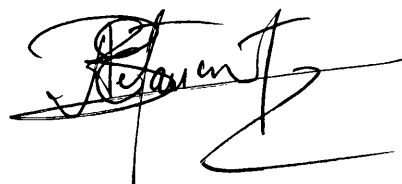
FIRST PRINCIPLES CALCULATIONS OF THE INTERACTION OF RARE-GAS ATOMS WITH TRANSITION METAL SURFACES

Submitted by Ángel E. Betancourt
for the degree of
Doctor of Philosophy
of the University of Bath
2000

COPYRIGHT

Attention is drawn to the fact that copyright of this thesis rests with its author. This copy of the thesis has been supplied on condition that anyone who consults it is understood to recognise that its copyright rests with its author and no information derived from it may be published without the prior written consent of the author.

This thesis may be made available for consultation within the University library and may be photocopied or lent to other libraries for the purposes of consultation.



UMI Number: U601564

All rights reserved

INFORMATION TO ALL USERS

The quality of this reproduction is dependent upon the quality of the copy submitted.

In the unlikely event that the author did not send a complete manuscript and there are missing pages, these will be noted. Also, if material had to be removed, a note will indicate the deletion.



UMI U601564

Published by ProQuest LLC 2013. Copyright in the Dissertation held by the Author.
Microform Edition © ProQuest LLC.

All rights reserved. This work is protected against
unauthorized copying under Title 17, United States Code.



ProQuest LLC
789 East Eisenhower Parkway
P.O. Box 1346
Ann Arbor, MI 48106-1346

Preface

This dissertation describes work done between April 1997 and September 2000 in the condensed matter theory group at the University of Bath, under the supervision of Professor David Bird. This dissertation is the result of my own work and has not been submitted in whole or in part for degree or diploma at this or any other university before.

Ángel E. Betancourt
Bath, September 2000

Dedicated to my wife Novelly and our child Rafael

Acknowledgements

I thank my supervisor Professor David Bird for his enthusiasm and interest in my work and for having introduced me to one interesting field of condensed matter physics.

I am grateful to the Venezuelan Research Council (CONICIT) and the Universidad de Oriente for a Ph.D studentship.

I acknowledge Dr. Simon Crampin for providing copies of the Troullier-Martins pseudopotential and Murnaghan fit programs.

I thank Professor Mats Persson for providing the data for the Barker and Rettner potential shown in Figure 4.11.

Thanks are due to John Ipe and John Trail for sharing offices with me and creating a friendly and pleasant workplace.

Finally, I thank my family for their love and support during this long and sometimes difficult time.

Abstract

We have studied the interaction between rare-gas atoms and transition metal surfaces for the systems Xe/Pt, Ne/Rh and He/Rh. All the calculations were carried out using models supported by first principles. Pseudopotentials for each element were constructed using the Troullier-Martins scheme and they were carefully tested by calculations of equilibrium geometry properties. The exchange-correlation effects were described with local density approximation (LDA) and generalised gradient approximation (GGA). A pseudopotential-mixed basis method was used as the main model to obtain the ground-state energy. For all studied systems, the binding mechanism was studied in terms of the projected density of states, which allows a determination of the charge transfer between the adsorbate and the metal surface. In the case of Xe adsorbed on the Pt(111) surface, we found a remarkable difference in the interaction potential curves between the exchange-correlation approximations. The results obtained with the LDA are in better agreement with experiment than the GGA, which contrasts with the observation that the GGA usually improves the LDA's results. Both approximations predicted that the on-top site is the most favourable place for adsorption of an Xe atom. For the cases of He and Ne on Rh(110), the GGA provided a better description of the adsorption parameters (well depth, vibrational energy and equilibrium adsorption height). Our results reproduce the anticorruating effect observed experimentally for He.

Also we have studied the interaction of a molecule of CO with the Pt(110) surface, in this case an ultrasoft potential scheme was used due to the difficulty of constructing efficient norm-conserving potentials for the elements that form the carbon monoxide molecule. Adsorption was studied as a function of the coverage of CO at the high symmetry sites and two possible structures for the Pt substrate were considered (an unreconstructed structure and a missing row structure). The equilibrium geometry structure was calculated which allowed us to determine the distortion of the clean substrate due to the adsorption of CO. Our estimations of the binding energies are larger than those reported in the literature.

Contents

1	Introduction	1
2	Theoretical Background	12
2.1	Introduction	12
2.2	Density functional theory	15
2.2.1	Exchange-correlation energy	18
2.3	Pseudopotentials	21
2.3.1	Norm-conserving pseudopotentials	22
2.3.2	Pseudopotential generation	23
2.3.3	Troullier and Martins pseudopotentials	25
2.3.4	Kleinman-Bylander form	25
2.3.5	Core-valence exchange-correlation	27
2.4	Total crystal energy for periodic systems	27
2.4.1	Plane wave basis sets	29
2.4.2	Brillouin zone integration	30

2.4.3	Kohn-Sham Hamiltonian within a plane wave basis set . . .	32
2.4.4	Conjugate gradients	33
2.4.5	Symmetrised charge density	33
2.4.6	Metallic systems and free energy	34
2.4.7	Supercell approximation	35
2.5	Mixed basis approach	36
2.5.1	Self-consistent field	38
2.5.2	Broyden's method	40
2.5.3	Kerker's mixing scheme and preconditioning	42
2.5.4	Projected density of states	43
2.6	Ultrasoft pseudopotentials	44
3	Validation of the pseudopotentials	47
3.1	Introduction	47
3.2	Pseudopotential construction	49
3.2.1	Electronic configuration	49
3.2.2	Core radii	50
3.2.3	Semi-relativistic pseudopotentials	55
3.2.4	Testing the Kleinman-Bylander form	57
3.3	Exchange-correlation energy	58

3.3.1	Core-valence exchange-correlation correction	60
3.4	Testing pseudopotentials	61
3.4.1	Core radius for Cu	63
3.4.2	Pseudopotential-plane-wave results	64
3.4.3	Testing core-radii	67
3.4.4	GGA pseudopotentials	69
3.4.5	Pseudopotential-mixed-basis results	69
3.4.6	He and Ne core radii	72
3.5	Conclusions	75
4	Interaction of Xe atoms with the Pt(111) surface	77
4.1	Introduction	77
4.2	The commensurate $(\sqrt{3} \times \sqrt{3})R30^\circ$ structure	81
4.3	Convergence of total energy	82
4.4	Convergence of the interaction potential	85
4.4.1	Testing the cut-off energies	86
4.4.2	Testing k-point sampling	87
4.4.3	Testing the super cell parameters	88
4.4.4	Fitting the potential data	89
4.5	Interaction potential	92

4.5.1	Dependence of the interaction potential with parameters of the calculation	95
4.6	Binding mechanism	98
4.6.1	Adsorption at the top site	98
4.6.2	Adsorption at the hollow site	102
4.7	Work function change	103
4.8	Conclusions	106
5	Interaction of light rare-gas atoms with the Rh(110) surface	108
5.1	Introduction	108
5.2	Computational details	111
5.2.1	Relaxation of the Rh(110) surface	112
5.2.2	Testing convergence	115
5.3	He and Ne interacting with the Rh(110) surface	118
5.3.1	Corrugation of the potential	120
5.4	Induced charge density	123
5.5	Conclusions	128
6	Chemisorption of CO on the the Pt(110) surface	130
6.1	Introduction	130
6.2	Computational details	133

6.2.1	CO molecule	133
6.2.2	Missing row and unreconstructed (110) surface	134
6.3	Chemisorption of CO	138
6.3.1	Adsorption at the unreconstructed surface	139
6.3.2	Adsorption at the missing-row surface	144
6.4	Conclusions	148
7	Conclusions	150
	Appendix A. Generalised Gradient Functionals	153
	References	157

List of Figures

3.1	Relativistic logarithmic derivatives in (Bohr radii) ⁻¹ for Rh wave functions around the atomic eigenvalues. Solid lines represent all-electron wave function results; dashed lines represent pseudo-atom results. Bullet symbols indicate the position of the eigenvalues. . . .	52
3.2	Pseudo (solid line) and all-electron (dashed line) for Pt 6 <i>p</i> valence wave functions.	53
3.3	σ in (Bohr radii) ⁻¹ as a function of the core radius for <i>s</i> _{1/2} (upper left) and <i>d</i> _{3/2} (upper right) pseudopotentials for Rh and <i>s</i> _{1/2} (lower left) and <i>p</i> _{1/2} (lower right) pseudopotentials for Xe. The solid line represents a fitted curve using a fourth degree polynomial and the calculated values are denoted by diamond symbols.	54
3.4	σ in (Bohr radii) ⁻¹ as a function of the core radius for the <i>s</i> _{1/2} (left panel) and <i>d</i> _{3/2} (right panel) pseudopotential of Cu. Solid line represents the fitted curve using a fourth degree polynomial and the calculated values are denoted by diamond symbols.	55
3.5	Relativistic ionic pseudopotential for Rh.	56
3.6	Comparison of the logarithmic derivatives in (Bohr radii) ⁻¹ of Rh between the average pseudopotential (solid line) and the Kleinman-Bylander form (dashed line). Arrows indicate the position of the eigenvalues.	58

3.7	The average ionic pseudopotentials in real space for Pt using the GGA approximation. Left corresponds to GGA-PW91 results and right to GGA-PBE. In both cases, the strongest oscillations close to the nucleus (small panel) were removed.	59
3.8	s pseudopotential in real space for Pt close to the nucleus using GGA-PBE and GGA-PW91.	60
3.9	s and d components of the ionic pseudopotential for Pt without (solid line) and with (dashed line) the non-linear core-valence exchange-correlation correction. The exchange-correlation energy was calculated with the GGA-PW91 approximation.	61
3.10	d pseudopotential for Pt at a selected set of core radii. (a) $r_c = 1.17$, (b) $r_c = 1.20$, (c) $r_c = 2.00$, (d) $r_c = 3.00$ and (d) $r_c = 4.00$. Units are Bohr radii.	68
3.11	Interaction potential energy for Xe_2 calculated with the LDA (solid line) and GGA-PBE (dashed line) approximations. Diamond symbols represent the calculated points.	72
4.1	Phase diagram of $\text{Xe}/\text{Pt}(111)$ from Kern <i>et al.</i> (1988). C, SI, HI, and HIR denote the commensurate $(\sqrt{3} \times \sqrt{3})R30^\circ$, the striped incommensurate, the hexagonal incommensurate and the hexagonal incommensurate rotated phase. G and L denote the two-dimensional gas and liquid phases respectively. T_c is the critical temperature, T_s is the substrate temperature and θ_{Xe} is the coverage of Xe.	78
4.2	Real space commensurate $(\sqrt{3} \times \sqrt{3})R30^\circ$ structure of Xe on the $\text{Pt}(111)$ surface and the sites available for adsorption. The subscript s denotes the substrate lattice vectors and a denotes the adlayer lattice vectors. Red circles represent the Xe atoms. White, yellow and green circles represent top, second, and third layers of the Pt substrate respectively.	81

4.3	Convergence of the charge density (left) and the total energy (right) for $(\sqrt{3} \times \sqrt{3})R30^\circ$ Xe/Pt(111) for a selected set of values of the A parameter within a self-consistent calculation. $G_0 = 1.5 \text{ \AA}^{-1}$	83
4.4	Convergence of the charge density (left) and the total energy (right) for $(\sqrt{3} \times \sqrt{3})R30^\circ$ Xe/Pt(111) structure for a selected set of values of the G_0 parameter within a self-consistent calculation. $A = 0.2$	84
4.5	Convergence of the total energy for the $(\sqrt{3} \times \sqrt{3})R30^\circ$ Xe/Pt(111) structure with the inclusion of a metric in the evaluation of the scalar products for self-consistent calculations. Black line represents the results without preconditioning.	85
4.6	Two-dimensional Brillouin zone for a hexagonal lattice. The irreducible wedge ($\Gamma K M \Gamma$ area) was used in the total energy calculation at the top, fcc-hollow, and hcp-hollow sites while a 1/4 of the Brillouin zone ($\Gamma K K' M' \Gamma$ area) was used for the bridge site.	88
4.7	Interaction potential energy for the $(\sqrt{3} \times \sqrt{3})R30^\circ$ Xe/Pt(111) structure at the top site fitted to fifth degree polynomial. Blue line corresponds to the case with $x = 1/z$ used as the independent variable in equation(4.3) while the red line corresponds to a fifth degree polynomial with $x = z$. The LDA was used to describe exchange-correlation effects. Diamond symbols represent the calculated points.	90
4.8	Interaction potential energy for the $(\sqrt{3} \times \sqrt{3})R30^\circ$ Xe/Pt(111) structure as a function of the height above the first surface layer, fitted to different orders of polynomial equation (4.3). Left panel corresponds to calculations made with the LDA and right with the GGA-PBE. Diamonds correspond to the calculated points; the solid lines represent curves obtained with polynomials of order 4 (green line), 5(blue line), and 6(red line) respectively. For both cases the inverse of z was used as the independent variable.	91
4.9	Fitted interaction potential energy around the equilibrium point.	92

4.10	Interaction potential energy for the $(\sqrt{3} \times \sqrt{3})R30^\circ$ Xe/Pt(111) structure at selected adsorption points over the surface (see Figure 4.2). Left corresponds to results with LDA approximation and right with GGA-PBE approximation.	94
4.11	Interaction potential energy as a function of height from the first surface layer. Left at the on-top, centre fcc-hollow and right bridge site.	95
4.12	Effect of non-linear core-valence exchange-correlation corrections on the interaction potential energy. Left corresponds to results obtained with the LDA and right with the GGA-PBE. Solid line represents results without non-linear core-valence corrections and dashed line including non-linear core corrections.	96
4.13	Interaction potential energy for the $(\sqrt{3} \times \sqrt{3})R30^\circ$ Xe/Pt(111) structure for consistent and non-consistent calculations. The first acronym before the dash indicates the approximation used for the exchange-correlation energy in the pseudopotential construction and the second one corresponds to that used in the total energy calculation. The lattice constant used for all case was the value obtained with LDA approximation, 3.93 Å.	97
4.14	Electronic charge density difference induced by the adsorption of Xe atoms at the on-top site. Positive values are shown by solid lines and negative values with dashed lines. The contour lines represent densities given by $\pm 2^n \times 10^{-3} e \text{ \AA}^{-3}$ with $n = 1, \dots, 5$. The position of the Xe and Pt atoms are shown by the cross and bullet symbols respectively.	98
4.15	Adsorption of Xe on Pt(111) and some key directions in the (111) surface. Xe atoms are represented by dashed circles and the Pt atoms in the first layer by full circles.	99

4.16	Local density of states projected onto the orbitals of selected Pt atoms; the Pt atom directly below the Xe atom is represented by a red line, the inequivalent Pt atom in the top layer is represented by green line and a Pt atom in the bottom layer is represented by a blue line.	101
4.17	The local density of states projected onto Xe orbitals (left panel). $5s$, $5p$ and $5d$ are represented by green, blue and red lines respectively. Close-up around the Fermi level (right panel).	102
4.18	Electronic charge density difference induced by the adsorption of Xe atoms at the hcp-hollow site. Positive values are shown by solid lines and negative value with dashed lines. The contour lines represent densities given by $\pm 2^n \times 10^{-3} e \text{ \AA}^{-3}$ $n = 0, ..5$. The position of the Xe and Pt atoms are shown by the cross and bullet symbols respectively.	103
4.19	Planar-averaged potentials as a function of the distance perpendicular to the surface. Red curve corresponds to the potential produced by five Pt layers, blue curve is the potential of the Pt slab with an adsorbed Xe and the green curve is the difference between the curves.	104
4.20	Work function change as a function of the adsorption height.	105
5.1	Schematic diagram of the (110) surface showing the unit cell used for (1×2) and (1×1) structures and the high symmetry sites available for adsorption. T : on-top, SB : short bridge, LB : long bridge, and H : hollow.	113
5.2	Variation of the total energy for the (1×1) Rh(110) structure as a function of the first interplanar spacing using the GGA-PBE approximation. The lattice constant used was 4.02 Å, Table 3.9.	114

5.3	Interaction potential energy for the He/Rh(110) structure at the top site as a function of the cut-off energy for the pseudo-atomic orbital expansion (equation 2.37). The additional plane-wave cut-off energy was fixed at 60 eV. The exchange-correlation energy was approximated with the GGA-PBE.	116
5.4	Interaction potential energy of He/Rh(110) (top right and top left) and Ne/Rh(110) (bottom right and bottom left) at on-top (green line), short bridge (blue line) and long bridge (red line) sites. Left LDA and right GGA-PBE.	119
5.5	Corrugation amplitude of the potential for He (left) and Ne (right) atoms over the Rh(110) surface, using the GGA-PBE approximation. The blue line corresponds to the corrugation along the closed-packed rows while the red line corresponds to the perpendicular direction, see Figure 5.1.	121
5.6	Electronic charge density difference induced by an He atom over the on-top site at three different heights from the topmost surface layer. The cut is along $[1\bar{1}0]$, see Figure 5.1. Left panel at 5.0 Å, middle panel at 3.75 Å (equilibrium height) and right panel at 2.16 Å (corresponds to a turning point of 150 meV). Positive values are shown by solid lines and negative values with dashed lines. Contour lines represent electronic charge densities given by $\pm 2^n \times 10^{-4} e \text{ \AA}^{-3}$ $n = 1, \dots, 5$, except for the right panel where each contour is multiplied by 10. The position of the He and Rh atoms are shown by the cross and bullet symbols respectively.	123
5.7	Electronic charge density difference induced by a Ne atom over the on-top site at three different heights from the topmost surface layer along $[1\bar{1}0]$, see Figure 5.1. Left panel at 5.0 Å, middle panel 3.61 Å (equilibrium height) and right panel at 2.51 Å (corresponds to a turning point of 150 meV). Positive values are shown by solid lines and negative values with dashed lines. Contour lines represent electronic charge densities given by $\pm 2^n \times 10^{-4} e \text{ \AA}^{-3}$ $n = 1, \dots, 5$, except for the right panel where each contour is multiplied by 10. The position of Ne and Rh atoms are shown by the cross and bullet symbols respectively.	124

5.8	Projected density of states for $5s$, $5p$ and $4d$ for the Rh atom below the incoming He atom. Green line corresponds to a He atom placed at a height of 5.0 \AA , blue line corresponds to a turning point of 150 meV (He at a height of 2.16 \AA).	125
5.9	Projected density of states for $5s$, $5p$ and $4d$ for the Rh atom below the incoming Ne atom. Green line corresponds to a Ne atom placed at a height of 5.0 \AA , blue line corresponds to a turning point of 150 meV (Ne at a height of 2.51 \AA).	126
5.10	Projected density of states for He (left panel) and Ne (right panel).	127
6.1	Top view of a fcc(110) (2×1) missing row structure and its high symmetry sites. The red circles represent the top layer of atoms, the green circles the second layer and the yellow circles the third. T: atop site, SB: short bridge site, LB: long bridge site and H: four-fold hollow site.	134
6.2	Convergence of the total energy (top left), displacement (top right), force on the movable atoms (bottom left), and the contraction/expansion of the separation of three subsequent atomic layers (bottom right) for the Pt(110) missing row structures. For the bottom right panel, green line: contraction of the first atomic layer; blue line: contraction of the second layer and red line: expansion of the third layer. The relaxation was defined as the percentage distortion of the layer divided by the bulk interlayer spacing.	135
6.3	Relaxed missing row structure of Pt(110). d_{ij} represents the perpendicular distance between the atoms i and j and l_i is the lateral distance between two equivalent atoms in the same layer. $d_{12} = 1.145 \text{ \AA}$, $d_{23} = 1.268 \text{ \AA}$, $d_{3'4} = 1.223 \text{ \AA}$, $d_{34} = 1.515 \text{ \AA}$, $d_{45} = 1.420 \text{ \AA}$, $l_2 = 4.032 \text{ \AA}$ and $l_4 = 4.117 \text{ \AA}$. The atoms move in the direction indicated by the arrows.	136

6.4	Top view of a fcc(110) unreconstructed surface and its high symmetric sites. The red circles represent the first layer of atoms and the green circles the second one. T: atop site, SB: short bridge site, LB: long bridge site and H: four hollow site.	138
6.5	Side view of stationary Pt (2 × 1) substrate and the CO adsorbate. d_{CO} is the distance between C and O, d_{PtC} denotes the distance between Pt and C.	141
6.6	A schematic diagram of the relaxation of the Pt(110) unreconstructed surfaces ((2×1) structure top and (1×2) structure bottom) when a CO molecule is adsorbed at the long bridge site. The atoms move in the direction indicated by the arrows.	142
6.7	A schematic diagram of the relaxation of the Pt(110) unreconstructed surface (1×2) when a CO molecule is adsorbed at the top site (left) and short bridge site (right). The atoms move in the direction indicated by the arrows.	143
6.8	A schematic diagram of the relaxation of the Pt(110) (2×1) missing row structure when a CO molecule is adsorbed at the long bridge site.	146

List of Tables

3.1	Electronic configurations used to generate pseudopotentials for He, Ne, Cu, Rh, Pt, and Xe atoms. The ionic configuration was taken from Bachelet <i>et al.</i> (1982). a for $l = 1$, b for $l = 2$	50
3.2	Core radii optimised from relativistic logarithmic derivative calculations for Pt, Rh, Cu, and Xe atoms. Core radii denoted with an asterisk were not optimised with equation (3.1). The Wigner-Seitz radius r_{ws} was taken from Moruzzi & Sommers (1995). Units are in Bohr radii.	53
3.3	Calculated lattice constant and bulk modulus for Cu using the local density approximation as a function of the plane wave cut-off energy and the d core radius.	63
3.4	Calculated lattice constant and bulk modulus for Cu, Rh, and Pt using the local density approximation, and the gradient generalised approximations (GGA-PW91 and GGA-PBE) as a function of the plane wave cut-off energy.	65
3.5	Calculated lattice constant and bulk modulus for Cu, Rh, and Pt the with local density approximation and the gradient generalised approximations (GGA-PW91 and GGA-PBE). Numbers in parentheses indicate the percentage error relative to experiment.	66
3.6	Calculated lattice constant, a , and bulk modulus, B , for Pt as a function of the core radius, r_c , and the cut-off energy. Numbers in parentheses indicate percentage relative error with respect to all-electron results (Khein <i>et al.</i> , 1995).	68

3.7	Total energy, E_{total} , as a function of the lattice constant for Pt using the GGA-PW91 approximation and a plane wave cut-off energy of 550 eV. The first column corresponds to a pseudopotential with oscillations at the origin while the second one corresponds to a pseudopotential with oscillations removed (see section 3.3). In the first case, the calculated lattice constant and the bulk modulus were 4.026 Å and 237.0 GPa respectively whereas in the second, they were 4.023 Å and 237.2 GPa.	69
3.8	Calculated lattice constant and bulk modulus for Rh as a function of the plane wave cut-off energy.	70
3.9	Calculated lattice constant and bulk modulus for Pt and Rh and calculated bond length and binding energy for the Xe dimer using a pseudopotential-mixed basis approach. CC denotes results for which non-linear core corrections are included.	71
3.10	Calculated binding energy (meV) for Ne ₂ as a function of the p core radius using the mixed basis method. Exchange-correlation effects were approximated with the GGA-PBE.	73
3.11	Calculated binding energy (meV) for He ₂ as a function of the s core radius using the mixed basis method. Exchange-correlation effects were approximated with the GGA-PBE.	73
3.12	Calculated bond length and binding energy for He and Ne dimers using the LDA and GGA-PBE approximations.	74
4.1	Interaction potential energy, V , for a Xe atom located at a height of 3 Å above the top site of the Pt(111) as a function of cut-off energies $E_{cut_{pw}}$ and $E_{cut_{ao}}$. The super cell consisted of five Pt layers and a vacuum gap equivalent to nine layers. Exchange-correlation effects were treating using the LDA.	86

4.2	Interaction potential energy for a Xe atom located at a height of 3 Å above the top site of the Pt(111) surface as a function of the number of special \mathbf{k} -points in the irreducible Brillouin zone (IBZ). The calculations were performed using $E_{cut_{ao}} = 500$ eV and $E_{cut_{pw}} = 60$ eV. WBZ represents the number of \mathbf{k} -points in whole Brillouin zone. The super cell consisted of five Pt layers and a vacuum gap equivalent to nine layers. Exchange-correlation effects were treated using the LDA.	88
4.3	Interaction potential energy, V , for an Xe atom located at a height of 3 Å above the top site of Pt(111) surface as a function of the number of Pt layers and equivalent vacuum layers. The irreducible Brillouin zone was sampled with 6 \mathbf{k} -points. The LDA was used for describing exchange correlation effects. The calculations were performed using $E_{cut_{ao}} = 500$ eV and $E_{cut_{pw}} = 60$ eV.	89
4.4	Calculated well depth, V_0 , equilibrium height, Z_0 , and vibrational energy, E_v , for Xe atoms adsorbed on the Pt(111) surface as a function of the interpolating polynomial.	91
4.5	Calculated well depth, V_0 , equilibrium height, Z_0 , and vibrational energy, E_v , for Xe atoms adsorbed on the Pt(111) surface in different adsorption sites.	94
4.6	Calculated potential well depth, V_0 , equilibrium height, Z_0 , and vibrational energy, E_v , for Xe atoms adsorbed on the Pt(111) surface at the on-top site. Lattice constant used for LDA calculations was 3.93 Å and for GGA-PBE, 4.02 Å. Numbers in parentheses indicate the absolute error with respect to result without non-linear core corrections (NLCC).	96
4.7	Difference of the charge Q^i (in $10^{-1}e$) upon Xe adsorption at the on-top site for Xe and Pt orbitals. For Xe and Pt we refer to the 5s, 5p, 5d and 6s, 6p, 5d orbitals respectively. The Pt atom was directly below the adsorbed Xe.	99

4.8	Difference of the charge Q^i (in $10^{-1}e$) upon Xe adsorption at the hcp-hollow site for Xe and Pt orbitals. For Xe and Pt we refer to the $5s$, $5p$, $5d$ and $6s$, $6p$, $5d$ orbitals respectively. Pt_{tl} and Pt_{sl} represent Pt atomic in the top layer and second layer respectively.	102
5.1	Contraction/expansion of the separation of two subsequent atomic layers for the Rh (110) surface using the LDA and GGA-PBE. Δd is the change in the distance between two consecutive atomic layers, d_0 is the interlayer distance in the bulk. US-LDA represents an LDA calculation based on the ultrasoft pseudopotential method.	115
5.2	Equilibrium height and potential well depth for He atoms interacting with the Rh(110) surface as a function of the degree of the interpolating polynomial.	117
5.3	Potential well depth, V_0 , and equilibrium height, Z_0 , for He and Ne interacting over the Rh(110) surface. Rh(110)(1×2)H corresponds to a hydrogen covered (110) surface of Rh.	118
5.4	Comparison of amplitudes of corrugation from the interaction potential of He and Ne with Rh(110). ξ_{10} corresponds to the amplitude of corrugation parallel to the closed-packed rows and ξ_{01} to the perpendicular direction. Kinetic energy of the incoming atom is 64 meV except the values marked with an asterisk that correspond to 34 meV.	122
5.5	Difference of the charge in $10^{-1}e$ associated with the $5s$, $5p$ and $4d$ orbitals of the Rh atom at the on-top (T) and short bridge (SB) sites.	127
6.1	Distortions of atomic positions for the Pt(110) (2×1) missing row structure. Δd_{ij} is the change in the layer spacing between the i th and j th layers, p_i represents pairing in layer i and b_3 represents buckling in the third layer.	137

6.2	Calculated adsorption properties of CO chemisorbed on the unreconstructed Pt (110) surface. Numbers in parentheses refer to calculations with substrate atoms fixed at their clean surface relaxed positions. The CO molecule is upright on the surface with the C end down. E_b denotes the binding energy, d_{CO} represents the C-O bond length and d_{PtC} denotes the C-Pt bond length, that is measured from the nearest Pt atom underneath the C atom (see Figure 6.5).	140
6.3	Comparison of adsorption properties: binding energy, E_b , C-O bond length, d_{CO} , and C-Pt bond length, d_{PtC} , for CO chemisorbed on the Pt (110) unreconstructed surface at a coverage of 0.5 ML.	144
6.4	Calculated adsorption properties (binding energy, C-O bond length and C-Pt bond length) of CO chemisorbed on the Pt (110) missing row surface. Numbers in parentheses refer to an unrelaxed Pt substrate.	145

Chapter 1

Introduction

First principles theory provides a framework for understanding the complexities associated with surface phenomena. Typically, first principles calculations on adsorbate-metal systems provide information as a function of the adsorption site and adsorbate geometry on the total energy, adsorption energy, wave functions, electronic charge distribution, projected density of states, work function, vibrational frequency and dipole moment. On the other hand, knowledge of the energy as a function of the atomic coordinates allows the determination of the equilibrium geometry, minimum energy reaction pathway and transition state energy. In general, a first principles formalism is quite demanding, but within density functional theory (DFT) (Kohn & Sham, 1965) high quality solutions can be obtained.

Any fundamental understanding of the microscopic properties of a solid surface requires a reasonably detailed model of the atomic geometry. Generally, the simplest structural model is usually chosen. It is assumed that the surface geometry is that which would result from a truncation of the bulk with no other changes. In general, the truncation model will not represent the most stable configuration (Masel, 1996). Rearrangements of the surface atoms and of the electronic charges

may occur for a real surface. If the rearrangement leads to changes in the interlayer spacing perpendicular to the surface, it is referred to as a relaxation, but if it results in a different two-dimensional geometry of one or more surface layers, it is called a reconstruction. Traditionally, the supercell geometry approximation has provided the most powerful way to represent these changes and to study the interaction between adsorbate atoms and a metal clean surface. The use of a slab enables us to obtain reliable results not only because it represents a real system more accurately than a small cluster, but also because the calculated results converge well with respect to the number of surface layers in the slab and the separation between slabs.

When atoms or molecules are adsorbed on an ordered crystal surface, they usually are assembled in ordered surface structures over a wide range of temperature and coverage (Lundqvist, 1990; Somorjai, 1994). By considering separately adsorbate-adsorbate interactions and adsorbate-substrate interactions, two well-defined features are distinguished. In the first case, the adsorbate-adsorbate forces are smaller than the adsorbate-substrate bonding, in this situation the bond involves a significant sharing of electrons between the adsorbate and the substrate (chemisorption). However, the adsorbate-adsorbate interaction can still control the long-range ordering of the over-layer. In the second case, the adsorbates do not create strong chemical bonds with substrate atoms. This situation is called physical adsorption or physisorption. For these adsorbates, the adsorbate-adsorbate interactions can dominate the adsorbate-substrate interactions, and in some cases incommensurate structures are formed, where the over-layer and the substrate have independent lattices. From an energetic point of view, the phenomena described above (chemisorption and physisorption) are usually defined in term of an arbitrary binding energy $|E_b| = 0.5$ eV/atom, which is accepted as the upper limit for physisorption and as the lower one for chemisorption (Spanjaard & Desjonquères, 1990).

The surface coverage of an adsorbate is another important parameter for understanding the geometry of the adsorbed layer. At very low coverages, some adsorbates gather together into two-dimensional islands. This effect is caused by short-ranged, attractive adsorbate-adsorbate interactions combined with easy diffusion along the surface. Other adsorbates repel each other, leading to disordered over-layers, where atoms or molecules are adsorbed in a series of distinct sites on the surface but the sites do not form any particular order. When the coverage is increased, the mean inter-adsorbate distance decreases, and the mutual interactions often strongly influence the ordering, favouring certain adsorbate configurations over others (Masel, 1996).

Physical adsorption is frequently found for rare-gas atoms and saturated molecules. The interaction potential of a physisorbed atom with a surface presents two well-defined regions (see Bruch *et al.* (1997)). First, at distances not far away from the surface ($\approx 5 \text{ \AA}$), the incoming atom is attracted by a van der Waals force. This force is a product of fluctuations in the dipole moment of the incoming atom that induces an image charge in the metal surface. Second, closer to the surface, there is a strong and repulsive interaction as a result of the overlap between wave functions of the impinging atom and the atoms of the surface. A fundamental aim of physisorption theory is to develop a unified framework that can completely describe the interaction potential energy for an impinging particle at any distance as it approaches the surface. Often, these potentials are constructed from empirical models which are parametrised to reproduce the binding energy and other observable properties.

The first attempt to calculate the interaction of rare-gas atoms with a surface in a direct manner that follows a more rigorous theoretical model was made by Zaremba & Kohn (1977). They used the Hartree-Fock approximation to describe the repulsive part of the potential and added an asymptotic van der Waals potential

for the long-ranged part. With such a scheme, only a rough description of the interaction could be obtained. Following Zaremba and Kohn's ideas, Holmberg & Apell (1984) endeavoured to find a better estimation of the attractive part of the potential by taking into account multipolar expansions for the dielectric response of the metal. However, the success obtained with these developments was limited in comparison with the results obtained with empirical methods (Hoinkes, 1980).

There have been relatively few attempts to calculate the interaction potential from first principles. One problem here is that it is not clear how to model the rare-gas surface interaction within DFT. The first works were made by Lang (1981) and Lang & Nørskov (1983), who reported that the local density approximation (LDA) provides a reasonable description of the interaction potential energy between rare-gas atoms and metal surfaces, although it does not give the correct asymptotic van der Waals tail. Liebsch (1987) made a time-dependent extension of the density functional approach in order to calculate the response function of the metal, but only a rough estimation of the metal response can be obtained using a local dielectric function. New functionals have recently been developed in order to include the van der Waals interaction within a density functional formalism (Andersson *et al.*, 1998; Dobson *et al.*, 1998; Hult *et al.*, 1999). However few calculations have been carried out with such schemes and these are limited to simple systems. Their application to complex systems (for instance an atom or molecule interacting with a surface) is still not clear, due to the difficulty of defining the electrodynamic effects within an unified treatment for different sizes of interacting objects (Lundqvist *et al.*, 1998).

On the other hand, Petersen *et al.* (1996) using a full-potential linear augmented plane wave method found that the generalised gradient approximation (GGA) provides a good description of the interaction of Ne and He with the Rh(110) surface and that LDA results are in worse agreement with experiment. Recently Trioni

et al. (1998b), using an embedding method, found that the LDA reproduces in a reasonable way the interaction of He and Ne over a surface of Ag. Our study of Xe/Pt(111) has demonstrated that the LDA gives more accurate potentials than the GGA (Betancourt & Bird, 2000). It seems that it is still not clear which approximation is the best for describing the interaction between rare-gas atoms and metallic surfaces. It is now well established that chemical bond energies calculated with the LDA have been improved systematically with the GGA (Hammer *et al.*, 1999; Perdew *et al.*, 1999; Patton *et al.*, 1997; Bird & Gravil, 1997; Hammer & Nørskov, 1997; García *et al.*, 1992; Ortiz & Ballone, 1991). However for systems with weak interactions, such as the van der Waals force between rare-gas diatomic molecules, the improvement of GGA over LDA is not completely successful. Here, the GGA reduces the over-binding of the LDA but the results still show a substantial deviation from experiment (Zhang *et al.*, 1997; Patton & Pederson, 1997). In principle, it is not expected that either the LDA or GGA should give an accurate description of the long-ranged part of the van der Waals interaction. This is because the LDA considers the charge density as a homogeneous distribution and therefore any possible effect between separated charge densities is removed. In the GGA, the long-ranged contributions are removed in the cut-off procedure that restores the exact conditions in the exchange-correlation hole (Burke *et al.*, 1998). Despite these shortcomings, the LDA and GGA are still used for studying the interaction of gas-rare atoms with metallic systems (Montalenti *et al.*, 1996; Petersen *et al.*, 1996; Trioni *et al.*, 1998b; Clarke *et al.*, 1998; Betancourt & Bird, 2000) and often show good agreement with experiment.

It is well-known that the description of the electron-ion interaction by *ab-initio* pseudopotentials has become a powerful tool in many areas of condensed matter physics (Ihm, 1988; Fuchs *et al.*, 1998). The separation of core and valence states allows balancing different length and energy scales making it possible to simplify many types of calculations. Additionally, the formalism of density functional

theory has played an important role in pseudopotential methods for electronic structure schemes, providing efficiency for large-scale calculations. However, it is surprising to find few rare-gas systems studied with this technique. This situation has encouraged us to undertake a study of the interaction of rare-gas atoms with transition metals using pseudopotentials. In particular, the systems Xe/Pt(111), He/Rh(110) and Ne/Rh(110) are studied.

Xe is one of the rare-gas atoms whose interaction with metallic surfaces has been widely studied both theoretically and experimentally (Küppers *et al.*, 1979; Lang, 1981; Lang *et al.*, 1982; Kern *et al.*, 1988; Barker & Rettner, 1992; Malafsky, 1992; Pérez *et al.*, 1994; Kulginov *et al.*, 1996; Bertel, 1996; Clarke *et al.*, 1998) and therefore provides a good test for different theoretical approaches. The Xe shows a significant degree of chemisorption which implies that the description of the bond cannot be explained only in terms of a van der Waals force (Ishi & Viswanathan, 1991). Large changes in the work function of the metal surface have been observed, which suggests a possible charge transfer mechanism for the adsorption of Xe atoms.

In the specific case of the system Xe/Pt there has been a long-running discussion of the adsorption site. Gottlieb (1990) found experimental evidence that indicated that the adsorption of Xe on Pt(111) occurs at the on-top site, which was confirmed by Müller (1990) using an LDA cluster calculation. However, his calculation shows a strong tendency for the clustering of Xe, which introduces doubts about whether the cluster used by Müller is adequate to describe the lateral interactions. Studies based on spin-polarised low-energy electron diffraction have questioned the on-top site, favouring the hollow site but with large adsorption height of 4.2 Å (Potthoff *et al.*, 1995). This contrasts with the value of 3.1 Å reported by Black & Janzen (1988). More recently, another low-energy electron diffraction (LEED) study (Seyller *et al.*, 1999) has favoured top-site adsorption.

In order to help clarify this point, we have studied the interaction between Xe and Pt(111) in the commensurate $(\sqrt{3} \times \sqrt{3})R30^\circ$ structure. Basically, our aim is to extend Muller's work by considering the interaction of the adsorbate with the substrate through the supercell approximation, which should provide a more reliable description of the lateral interactions. Additionally, we are interested in whether the standard approximations used to describe the exchange-correlation effects (i.e. LDA and GGA) are able to provide a reasonable model of the adsorption of Xe atoms.

In the last few years there has been a considerable interest for understanding the interaction of light rare-gas atoms with crystalline surfaces (see Farías & Rieder (1998) for a recent review of the subject). In the case of the light rare-gas atoms (He and Ne), their importance is due to the development of the scattering of low-energy neutral particles as a technique for studying the structural characteristics of clean and adsorbate-covered surface. Here, the interaction potential energy is the fundamental quantity that is needed to provide an accurate interpretation of diffraction measurements and it is important to construct potentials that accurately reflect the details of the atom-surface potential. Few first principles calculations of the interaction potential for He and Ne have been made for understanding the anti-corrugating effect observed from diffraction experiments (Rieder & García, 1982; Rieder *et al.*, 1993). The corrugation profile shows that He atom got closer to the top position than to the bridge position with respect to the distance obtained from Ne diffraction. Petersen *et al.* (1996) using all-electron calculations explain this phenomenon in terms of the hybridisation between rare-gas orbitals and the *d*-band states of the metal (Petersen *et al.*, 1996). We have selected the systems He/Rh(110) and Ne/Rh(110) in order to confirm the results reported by Rieder *et al.* (1993) and also to reveal the accuracy of the *ab-initio* pseudopotentials for these rare-gas atom systems.

All calculations for Xe/Pt, He/Rh and Ne/Rh were carried out using models based on first principles, which are free of phenomenological parameters. Pseudopotentials were constructed following the Troullier-Martins model (Troullier & Martins, 1990). All information about the rare-gas surface potential was obtained with total energy calculations (Ihm, 1988) within the DFT formalism (Kohn & Sham, 1965). The Kohn-Sham equations were solved by expanding the electronic wave function in terms of a mixed basis set, that consists of localised orbitals and plane waves (Louie *et al.*, 1979; Gülseren *et al.*, 1998). We will demonstrate that the mixed basis set can compete in accuracy with more familiar plane wave methods, while additionally having the advantage of using a chemical language (Mulliken, 1955). Another point that will be emphasised is related to the question of which exchange-correlation approximation provides the best description for the interaction of rare-gas atoms.

We now turn to the chemisorption case, which can be classified in two areas: atomic and molecular chemisorption (Nørskov, 1990). Atomic chemisorption is the simplest, where a single atom binds to the metal surface. It is perhaps less important than molecular chemisorption, but the main features of our current understanding of chemisorption have been extracted from single-atom adsorbates. General trends have been determined, concerning the variation of binding energy with the nature of the adsorbate and the substrate (Hammer & Nørskov, 1997). In the case of molecular chemisorption, when molecules impinge upon a surface molecular bonds may be broken (dissociative chemisorption), or not (associative adsorption). Therefore, it is important to know whether a molecule approaching a surface will dissociate or not. But this question is a complicated problem and its answer will depend on the dynamical motion of the impinging molecule at the surface and on energy transfer between the molecule and substrate (Darling & Holloway, 1995). In general, the adsorption of diatomic molecules on a surface is a more complex process than the adsorption of simple atoms, but it represents a key step for understanding the

behaviour of more complex molecular adsorbates.

The adsorption of CO molecules on a variety of metal surfaces has been intensively studied both experimentally and theoretically (Whitten & Yang, 1996; Hammer *et al.*, 1996, 1997; Pacchioni *et al.*, 1997; Ma *et al.*, 1998; Scheffler & Stampfl, 1999; Lynch & Hu, 2000, and reference therein). However, there are still many outstanding issues relating to the favoured adsorption site, the structure of the CO layer at high and low coverage, the interpretation of the spectroscopic properties, and the type of bonding of CO on different metals.

The bonding of CO to metal surfaces has usually been understood in term of Blyholder's model (Blyholder, 1964). Within this model the bonding is assumed to be derived from the donation of 5σ orbital (completely full in the gas phase) to the metal and the back donation of the metal to the 2π orbital (originally empty). Hammer *et al.* (1996) have developed a more quantitative model than that also considers the importance of the metal d and sp states. They have claimed that the interaction with the metal sp electrons causes a down shift and broadening of both 2π and 5σ states, while the coupling to the metal d states causes bonding and anti-bonding states below and above the two original states.

In the particular case of CO on Pt surfaces, the general interest in the adsorption is due to its importance in understanding catalytic CO oxidation (Tappe *et al.*, 1997; von Oertzen *et al.*, 1998; Scheffler & Stampfl, 1999; Patchett *et al.*, 2000). Although in the literature there are several works about adsorption of CO on Pt surfaces, the Pt(110) surface has not received so much attention. One problem with this system, that it is disordered for most coverages, making it difficult to apply the usual surface structure techniques for exploring the adsorbate structure (Schwegmann *et al.*, 1995). The CO/Pt(110) system is also important as a prototype of the adsorbate-induced structural transformation. The clean Pt(110) substrate is

(2×1) reconstructed, but undergoes a transition into a (1×1) structure when CO is adsorbed on it (Comrie & Lambert, 1976; Gritsch *et al.*, 1989; Schwegmann *et al.*, 1995).

The CO/Pt(110) system shows features that are quite different to the rare-gas atom systems described above, due to the strong chemisorption bond between CO and the metal which can induce a reconstruction of the Pt surface. Also C and O pseudopotentials are deep and although the Troullier-Martins scheme provides optimised pseudopotentials these are not really suitable for these elements, because of the very large computational effort that is required to calculate of the equilibrium geometry of the CO/Pt(110) system. Because of this, all the calculations for the CO/Pt(110) system were made with ultrasoft pseudopotentials (Vanderbilt, 1990).

The thesis is organised as follows. Chapter 2 provides the theoretical background used throughout the present work. An outline of the density functional formalism and the most widely used exchange-correlation approximations (LDA and GGA) is presented, together with *ab-initio* pseudopotential theory and strategies for solving the Kohn-Sham equations in term of plane wave basis sets, and mixed basis sets. In Chapter 3 we describe how the pseudopotentials were constructed and tested. The adsorption of Xe atoms over the surface (111) of platinum is analysed in Chapter 4. Different adsorption sites are considered and comparisons made between the interaction potentials for the local and the non-local exchange-correlation functionals. The binding mechanism is studied in term of induced charge density and the projected density of states. In Chapter 5, the interaction between light rare-gas atoms (He and Ne) and the Rh(110) surface is considered. A similar study to the previous chapter is made, finding in this case that the non-local functional seems to give a better description of the interaction, in contrast to the results found for Xe/Pt(111). In Chapter 6, the adsorption of CO over the Pt(110) surface is treated using ultrasoft pseudopotentials. The binding energy is studied as a function of

the coverage of CO for the unreconstructed and the missing row surfaces. Finally, a summary of the main conclusions are presented in Chapter 7.

Chapter 2

Theoretical Background

2.1 Introduction

The theoretical study of the properties of materials through electronic-structure calculation is a very active area in condensed matter field. Much of the progress is a consequence of the success of the density functional theory (Kohn & Sham, 1965) as an approach to describe many-electron systems using the electron charge density as the natural variable. The Kohn-Sham idea has been extended to multicomponent systems, to electronic and magnetic fields, to superconductors, and has been generalised to various ensembles include the thermal ensemble (Callaway & March, 1984; Gross *et al.*, 1995; Rajagopal, 1998; Heinonen *et al.*, 1998; Gidopoulos, 1998). The theory has not only provided a theoretical framework for discussing the many-electron problem but also has been developed as an effective computational tool widely used in condensed matter systems.

The Kohn-Sham approach leads to a one-body problem, where each electron moves in an effective potential that is calculated self-consistently. The exact form of the

exchange-correlation potential is not known, therefore an approximation is needed. The simplest is the local density approximation that assumes each inhomogeneous point of the electron density as being homogeneous (Parr & Yang, 1989). Surprisingly, this approximation has given accurate results for many real systems (Jones & Gunnarsson, 1989). By taking as a starting point the local density approximation, systematic improvements have been developed for the exchange-correlation functional by incorporating inhomogeneous effects. One of the most important and widely used is the generalised gradient approximation given by Perdew & Wang (1986).

One of the most effective techniques for performing self-consistent electronic-structure and total energy calculations is based on the use of pseudopotentials for describing the electron-ion interaction and the expansion of Kohn-Sham eigenfunctions in terms of a plane wave basis set (Kresse & Furthmüller, 1996a; Fuchs & Scheffler, 1999). The plane wave basis set allows the use of Fourier transforms to increase the efficiency of calculating the action of the Hamiltonian on the wave function. For example, the local potential part of the Hamiltonian is diagonal in real space while the kinetic energy part is diagonal in reciprocal space. It follows that the evaluation of the action of the Hamiltonian is fast if the wave function is transformed from reciprocal space to real space and back using Fourier transformations, an operation which fits very naturally within a plane-wave basis. Normally the evaluation of Fourier transforms is more efficient with the fast Fourier transform than the straightforward calculation. To determine the discrete Fourier transform, a total of N^2 operations are required (N is the number of grid points) while fast Fourier transformation reduces the work to $N \log(N)$ (Press *et al.*, 1992). This is an important difference for large N . Additionally, the plane wave basis set is preferred because in the evaluation of the atomic forces the Pulay contribution (Pulay, 1969) is avoided. It follows that the electronic, structural and dynamic properties of a material can all be evaluated at the same time.

The introduction of *ab-initio* pseudopotentials by Hamman *et al.* (1979) leads to the creation of a new family of optimised pseudopotentials (Troullier & Martins, 1990; Rappe *et al.*, 1990; Lin *et al.*, 1993) that have allowed a major development in electronic structure calculations. However there are still difficulties in performing calculations on materials containing first-row and 3d transition metal elements because a large number of plane waves are required to describe the localised valence states in these systems. An improvement in the evaluation of the Kohn-Sham equations can be obtained if a scheme using a mixed basis (plane waves and atomic orbitals) set is adopted (Louie *et al.*, 1979; Gülseren *et al.*, 1998). Within this model, the Kohn-Sham equations are transformed into a generalised eigenvalue problem but with a dimension much smaller than for its pure plane-wave counterpart. Recently, Vanderbilt (1990) has introduced a new concept of pseudopotentials (ultrasoft), within these novel pseudopotentials no more than 50-100 plane waves per atom are required, even in the difficult cases of 3d transition metal and first-row elements.

For a condensed matter system, the calculation of the total energy presents two distinct minimisation problems that must be addressed. The first is related to the requirement of the variational principle in density functional theory; that for each geometry the charge density must be found that minimises the total energy. The second problem involves the determination of the structure that is energetically most favourable. Therefore, an efficient method will allow us to calculate the ground state electron density distribution and the structural geometry at the same time. Car & Parrinello (1985) showed that molecular dynamics and density functional theory can be combined to give a parameter-free method for evaluating the ground state with no assumption about the ground state geometry. Car and Parrinello's method has opened new perspectives in the physics of complex systems: liquids, clusters, solids and complicated surface reconstructions. Direct methods to calculate the electronic ground states for systems with a large number

of non-equivalent atomic site in the unit cell also have been developed, which provide a more efficient way to determine the ground state than molecular dynamics (Teter *et al.*, 1989; Kresse & Furthmüller, 1996b).

The present chapter presents an introduction to all of the theoretical methods that will be used in later chapters. It is organised as follows. Section 2.2 gives an outline of the density functional theory and the most important approximations used to describe the exchange-correlation effects (the local density approximation and the generalised gradient approximation). Norm-conserving pseudopotentials are discussed in section 2.3. In this section we will concentrate on the principles that underpin *ab-initio* pseudopotentials, the procedure of their generation, and we briefly explain how a Troullier & Martins pseudopotential is defined. Additionally, we discuss the importance of generating fully non-local pseudopotentials within the Kleinman & Bylander form and the improvement in the transferability of the pseudopotential through the inclusion of the core charge density. In section 2.4, various aspects of the total energy calculations for periodic systems are discussed, such as the expansion of the Kohn-Sham equations in terms of a plane wave basis set, integration in reciprocal space, difficulties with metallic systems, the free energy scheme and the supercell approximation. In section 2.5, the mixed basis method is presented as an alternative technique for solving the Kohn-Sham equations. Ultrasoft pseudopotentials are briefly discussed in section 2.6.

2.2 Density functional theory

The problem of N interacting particles in an external potential is very difficult, its solution, necessarily approximated, is commonly expressed by a $3N$ -dimensional Schrödinger equation for the wave function $\psi(\mathbf{r}_1, \mathbf{r}_2, \dots, \mathbf{r}_N)$. Although methods

based on wavefunction construction work well for systems with few electrons, these become practically impossible for large systems. Within the density functional theory (DFT) formalism, calculations are made without the need to construct the many-body wave function, all the required information is provided by the electronic charge density (Parr & Yang, 1989).

Hohenberg & Kohn (1964) showed that for a system of interacting particles in an external potential, $V_{ext}(\mathbf{r})$, (e.g. arising from nuclei) there is a universal functional $F[\rho]$ of the density, ρ , independent of the external potential, such that the ground state energy and the density can be obtained by minimising the energy functional

$$E[\rho] = F[\rho] + \int V_{ext}(\mathbf{r})\rho(\mathbf{r})d^3\mathbf{r}, \quad (2.1)$$

with respect to charge density variation and subject to the constraint that the number of particles is constant. Therefore, in principle, the ground state density is sufficient to determine the many-body energy. The functional F is not known and depends on the type of interaction existing in the system, the dimensionality of space, and on the parameters of the Hamiltonian. F is defined as the kinetic energy plus the electron-electron interaction energy, which consists of a combination of its quantum and classical part

$$F[\rho] = T_s[\rho] + \frac{1}{2} \int \int \frac{\rho(\mathbf{r})\rho(\mathbf{r}')}{|\mathbf{r} - \mathbf{r}'|} d^3\mathbf{r}d^3\mathbf{r}' + E_{xc}[\rho]. \quad (2.2)$$

The first term is the kinetic energy of non-interacting electrons of density ρ , the second term is the classical mean-field inter-electronic Coulomb energy, and the third term is an universal functional of ρ and represents the non-classical many-body effects of exchange and correlation (xc). The many electron ground state

energy for a given external potential is given by

$$E[V_{ext}, \rho] = T_s[\rho] + \frac{1}{2} \int \int \frac{\rho(\mathbf{r})\rho(\mathbf{r}')}{|\mathbf{r} - \mathbf{r}'|} d^3\mathbf{r} d^3\mathbf{r}' + E_{xc}[\rho] + \int V_{ext}(\mathbf{r})\rho(\mathbf{r})d^3\mathbf{r}. \quad (2.3)$$

To evaluate equation (2.3), it is necessary to determine the self-consistent charge density ρ which minimises $E[V_{ext}, \rho]$; in addition the evaluation of $T_s[\rho]$ is not straightforward just with knowledge of the charge density. These difficulties are overcome by minimising equation (2.3) with respect to single-particle wave functions $\psi_i(\mathbf{r})$ which leads to a set of single-particle equation, known as the Kohn-Sham equations (Kohn & Sham, 1965):

$$\left[-\frac{1}{2}\nabla^2 + V_{eff}(\mathbf{r}) \right] \psi_i(\mathbf{r}) = \epsilon_i \psi_i(\mathbf{r}). \quad (2.4)$$

The ϵ_i are Lagrange multipliers that ensure the normalisation of the orbitals ψ_i during the variational procedure. The effective one-electron potential is given by

$$V_{eff}(\mathbf{r}) = V_{ext}(\mathbf{r}) + \int \frac{\rho(\mathbf{r}')}{|\mathbf{r} - \mathbf{r}'|} d^3\mathbf{r}' + V_{xc}[\rho(\mathbf{r})], \quad (2.5)$$

where the exchange-correlation potential V_{xc} is the functional derivative of the exchange-correlation energy

$$V_{xc}[\rho(\mathbf{r})] = \frac{\delta E_{xc}[\rho(\mathbf{r})]}{\delta n(\mathbf{r})}, \quad (2.6)$$

and $\rho(\mathbf{r})$ is defined as

$$\rho(\mathbf{r}) = \sum_i^N f_i |\psi_i(\mathbf{r})|^2, \quad (2.7)$$

which requires that the solution be self-consistent. f_i is the occupancy factor. Once some kind of approximation is assumed for the exchange-correlation energy, solutions of ψ_i , the charge density, equation (2.7), and the effective potential, equation (2.5), are determined and then a new value of ψ_i is calculated by re-solving equa-

tion (2.4). This cycle is repeated until the input and output solutions are identical. We have to emphasise that the energy eigenvalues do not correspond to elementary excitations so the band structure of ϵ_i is of interest for arguments concerning bonding, alloying, phase stabilities, etc., but not for optical spectra (Sutton, 1996).

2.2.1 Exchange-correlation energy

Within the density functional theory formalism, the exchange-correlation functional is unknown and an approximation is required. In the literature, several approximations for the exchange-correlation energy are available (Wigner, 1933; Kohn & Sham, 1965; Hedin & Lundqvist, 1971; Slater, 1974; Ceperly & Alder, 1980; Langreth & Mehl, 1983; Perdew & Wang, 1986; Becke, 1988; Lee *et al.*, 1988; Perdew & Wang, 1992; Perdew *et al.*, 1996b). The exchange-correlation energy consists of physical effects due to the electron-electron potential and the kinetic energy. The exchange energy component reduces the Hartree potential energy, the antisymmetry of the wave function causes electrons with the same spin orientation to avoid each other. The correlation energy has two contributions: a negative part due to the Coulomb potential which arises because electrons of either spin avoid each other, and a positive part associated with an increase in kinetic energy due to the reduction in space because of the mutual avoidance. In applications to atoms, molecules and condensed matter, the local density approximation is the simplest and most widely used approximation for the exchange-correlation energy (Jones & Gunnarsson, 1989)

$$E_{xc}^{LDA}[\rho] = \int \rho(\mathbf{r}) \epsilon_{xc}(\rho(\mathbf{r})) d^3\mathbf{r}, \quad (2.8)$$

where ϵ_{xc} is the exchange-correlation energy per particle in an uniform gas of density ρ . ϵ_{xc} is accurately known from Monte Carlo calculations (Ceperly & Alder, 1980), and it has been fitted to an analytic representation (Perdew & Zunger, 1981) which

allows practical calculations to be made. The LDA is, by definition, exact when the density is uniform, and accurate when it varies slowly. For real electronic systems, where these conditions are violated, the LDA still retains a useful degree of accuracy. The LDA gives the geometry of molecules and solids with an accuracy of about 1% but the dissociation energy of molecules and the cohesive energy of solids are wrong by about 10-20% (Kohn, 1999). The unexpected success of LDA is attributed to the LDA exchange-correlation hole satisfying the exact hole normalisation conditions. Even though the LDA hole is a poor approximation to the exact hole, the exchange-correlation energy depends on the angular averaged hole and with this average much of the error of the LDA is cancelled (Parr & Yang, 1989).

For slowly-varying densities, improvements over the LDA have been made by a gradient expansion approximation (GEA) (Kohn & Sham, 1965). Although gradient expansions provide an accurate correction for densities with a small density gradient, this is not the case for atoms and molecules. In general it has been demonstrated that a GEA does not predict better results than the LDA for real densities (Perdew, 1995). The main reason is that the GEA-hole is poorly damped and oscillatory at large separation and it violates the hole normalisation and negativity conditions (Burke *et al.*, 1998). Perdew *et al.* (1992) constructed a gradient expansion that fulfils the hole normalisation condition. They used a real-space cut-off procedure for removing the unphysical behaviour of the gradient expansion, generating a short-ranged hole that is much closer to the exact hole. This has improved the binding energy of finite systems. Within this generalised gradient approximation, the exchange-correlation energy is written as

$$E_{xc}^{GGA}[\rho] = \int f(\rho(\mathbf{r}), \nabla\rho(\mathbf{r}))d^3\mathbf{r}, \quad (2.9)$$

where f is an analytic function. Several GGAs have been proposed by different

authors (Langreth & Mehl, 1983; Perdew & Wang, 1986; Becke, 1988; Lee *et al.*, 1988), most of them are semi-empirical, depending upon parameters which are fitted to energies of known systems. Perdew & Wang (1992) have developed a more general GGA functional which satisfies limiting properties of a homogeneous gas and which has no fitting parameters. Recently Perdew, Burke and Ernzerhof have introduced a simplification of this GGA (Perdew *et al.*, 1996b) which is almost the numerical equivalent of PW91(see Appendix A). Zhang & Yang (1998) have calculated a new value of the parameter that controls the large gradient limit of the PBE exchange energy; this modification is known as rev-PBE, and leads to an improvement in the atomisation energy of small molecules. Hammer *et al.* (1999) have also claimed that rev-PBE leads to better chemisorption energies of atoms and molecules on transition metal surfaces. Although the atomisation energy is improved with rev-PBE, it provides a worse estimate for the bond length (Perdew *et al.*, 1998).

The improvements of the GGA are significant in many fields of atomic, molecular and condensed matter physics (Perdew *et al.*, 1992; Lee & Martin, 1997). The GGA has improved the cohesive energy of a large number of molecules (Ortiz & Ballone, 1991) and solids (García *et al.*, 1992). Also, there is a considerable improvement for surface binding energies and barrier heights (Hammer *et al.*, 1999; Bird & Gravil, 1997). However for the structural properties of semiconductors (Juan & Kaxiras, 1993) and transition metals belonging to the 4*d* and 5*d* series, GGA provides no improvement over the LDA (Klein *et al.*, 1995). In general, it is found that the GGA tends to underestimate the bulk modulus and over-corrects the lattice constant when compared with the LDA.

2.3 Pseudopotentials

A solid is a collection of ion cores and valence electrons. Ion cores contain a nucleus and tightly bound electrons (core electrons). Core wave functions are well localised about lattice sites while valence electrons can be found with a high probability in the interstitial region. Although these states can be expanded in term of a plane wave basis set, plane waves are unsuitable to describe the oscillatory behaviour of the wave function in the core region, due to the large number of plane waves that are required. However, many physical properties of solids are controlled to a large part by their valence electrons rather than the core electrons. Within the pseudopotential approximation, the properties of solids are calculated by assuming that ion cores are not perturbed by the rearrangement of the valence electrons. Therefore with this approximation, it is possible to remove the participation of the core electrons in an atomic calculation, by considering the nucleus plus the core electrons as an inert or “frozen” core. All electrostatic and “quantum-mechanical” interactions are incorporated as angular dependent pseudopotentials which are identical to the true potential outside of the core region but are weaker inside it. The valence electrons are represented by “smooth” pseudo-orbitals which are identical to the real wave function in the valence region but which have no nodal points near the nucleus.

In earlier times, pseudopotentials were applied to the electronic structure and ground states properties of solids and they were represented by analytic potential models with parameters fitted to experimental data (Abarenkov & Heine, 1965; Schlüter *et al.*, 1975). Phillips & Kleinman (1959) derived the first pseudopotentials from atomic core and valence wave functions without experimental information. In this scheme, the pseudo wave function and the real wave function have the same shape, but they differ in their amplitudes outside the core region, which causes

serious trouble in the calculation of the Coulomb potential during a self-consistent procedure. Hamman *et al.* (1979) avoided this problem by adopting a scheme of norm-conserving *ab-initio* pseudopotentials, which describe accurately the valence electrons in different atomic and solid-state environments.

2.3.1 Norm-conserving pseudopotentials

The concept of norm-conserving pseudopotentials has allowed a major development in the field of electronic state calculations. Pseudopotentials can be constructed from a self-consistent, all-electron calculation for the atom in a reference configuration. The construction is defined by a set of fundamental conditions which must be completely fulfilled by the pseudo wave function, with the purpose of producing a faithful wave function in the valence region (Hamman *et al.*, 1979). These constraints are as follows:

1. The pseudo wave function, Ψ_i^{PP} , and the all-electron wave function, Ψ_i^{AE} , are identical beyond a core radius r_{cl}

$$\Psi_i^{PP} = \Psi_i^{AE} \text{ for } r > r_{cl}. \quad (2.10)$$

The value of r_{cl} is taken greater than the last nodal point of Ψ_i^{AE} .

2. For the same atomic configuration, Ψ_i^{PP} and Ψ_i^{AE} have the same eigenvalue

$$\epsilon_i^{AE} = \epsilon_i^{PP}. \quad (2.11)$$

3. The pseudo charge enclosed within the sphere of radius r_{cl} is the same as for

the all-electron wave function (norm conservation)

$$\int_0^{r_{cl}} |\Psi_l^{PP}|^2 r^2 dr = \int_0^{r_{cl}} |\Psi_l^{AE}|^2 r^2 dr. \quad (2.12)$$

This normalising of the pseudo wave function assures that the electrostatic potential is identical for both charge distributions outside the core radius.

4. At the same reference energies, the pseudo and all-electron logarithmic derivatives agree for $r \geq r_{cl}$. The total charge inside the sphere is related to the first energy derivative of the logarithmic derivative of the wave function at the sphere boundary by the identity

$$\int_0^{r_{cl}} r^2 \Psi_l^2(\epsilon', r) dr = -\frac{r_{cl}^2 \Psi_l^2(\epsilon', r)}{2} \frac{\partial}{\partial \epsilon} \frac{\partial}{\partial r} \left(\ln \left(\Psi_l(\epsilon', r) \right) \right)_{r=r_{cl}}^{\epsilon=\epsilon'} \quad (2.13)$$

where $\Psi_l(\epsilon', r)$ is the solution of the Schrödinger equation at energy ϵ' (not necessarily an eigenfunction) for either the all-electron potential or the pseudopotential. The scattering properties of the pseudopotential and the full potential have the same energy variation to first order. However, there is no guarantee that the logarithmic derivatives match over a useful range. The energy range over which the logarithmic derivatives of pseudopotentials are equal to those of the full potential is a measure of the range over which the pseudopotentials are accurate.

2.3.2 Pseudopotential generation

A standard procedure for generating *ab-initio* pseudopotentials starts by solving self-consistently the all-electron problem, in order to find eigenvalues ϵ_l^{AE} , wave functions Ψ_l^{AE} and the electron screening potential, $V_H + V_{xc}$, for a chosen reference configuration. Inside the core radius, the valence wave functions are then

replaced by parameterised analytical expressions whose parameters are defined by imposing continuity of the wave function and its derivatives at the core radius, and the norm-conserving constraints (see subsection 2.3.1). As a result, the screened pseudopotential will be an analytic function which is obtained by inverting the radial part of the Schödinger equation

$$V_{l,scr}^{PP}(r) = \epsilon_l - \frac{l(l+1)}{2r^2} + \frac{1}{2rR_l^{PP}(r)} \frac{d^2}{dr^2} \left(rR_l^{PP}(r) \right). \quad (2.14)$$

We note that each angular momentum component of the pseudo wave function will feel a different potential. The full ionic pseudopotential is then generated by removing the screening effect of the valence electrons

$$V_{ion,l}^{PP}(r) = V_{scr,l}^{PP}(r) - V_H^{val}(r) - V_{xc}^{val}(r). \quad (2.15)$$

In general, this potential can be used in a self-consistent procedure to determine the electronic structure in another environment. Several pseudopotential models have been developed following the procedure outlined above (Kerker, 1980b; Bachelet *et al.*, 1982; Vanderbilt, 1985; Troullier & Martins, 1990, 1991) by implementing different functions for the wave function inside the core region and adding additional constraints in the pseudopotential construction which have allowed the construction of more rapidly convergent pseudopotentials. In some cases, a separate optimisation procedure has been applied after generating the pseudopotential (Rappe *et al.*, 1990; Lin *et al.*, 1993). In the next section, a brief outline of Troullier and Martins' scheme (Troullier & Martins, 1990, 1991) will be given. These pseudopotentials are widely used and provide accurate and well optimised potentials for plane-wave expansions.

2.3.3 Troullier and Martins pseudopotentials

Kerker (1980b) carried out a parameterisation of the radial pseudo wave function inside the core region using an exponential of a polynomial function

$$R_i^{PP}(r) = \begin{cases} R_i^{AE}(r) & r > r_{cl} \\ r^l \exp(p(r)) & r \leq r_{cl} \end{cases} \quad (2.16)$$

where R_i^{AE} is the radial part of the all-electron wave function and $p(r)$ is a fourth order polynomial whose coefficients are chosen to give a smooth, non-singular pseudopotential which obeys the constraints given in subsection 2.3.1.

Troullier & Martins (1990, 1991) generalised Kerker's method by increasing the order of the polynomial to eight which allows the freedom to explore properties which increase the smoothness of a parametrised family of pseudopotentials. Addition to the restrictions used by Kerker, Troullier & Martins forced the continuity of the wave function and its first four derivatives at the core radius, together with the analyticity and zero curvature of the pseudopotentials at the origin. These properties improve the softness of the potential, whereby a lower cut-off energy is required for well-converged results in total energy calculations using a plane wave basis.

2.3.4 Kleinman-Bylander form

The ionic potential calculated by equation (2.15) is semi-local, in other words, non-local in the angular coordinates and local in the radial coordinate

$$V_{ion}^{PP}(r, r') = V_{ion,local}^{PP}(r)\delta(r - r') + \delta(r - r') \sum_{l,m} \Delta V_l(r) | Y_{lm}(\hat{r}) \rangle \langle Y_{lm}(\hat{r}') |, \quad (2.17)$$

where Y_{lm} are the spherical harmonics, $V_{ion,local}^{PP}(r)$ is the local potential part which, in principle, is chosen arbitrarily and $\Delta V_l(r)$ is defined by

$$\Delta V_l(r) = V_{ion,l}^{PP}(r) - V_{ion,local}^{PP}(r). \quad (2.18)$$

With this semi-local dependence, $V_{ion,l}^{PP}(r)$ is inconvenient for total energy calculations using a plane wave basis because a huge number of integrals need to be calculated during the construction of the matrix elements. Kleinman & Bylander (1982) proposed a fully separable form which allows for a substantial saving in computational demand, by requiring the evaluation of a number of integrals approximately equal to the number of the plane waves needed:

$$\Delta V_{non-local,l}^{KB}(r) = \frac{|\Delta V_l(r) R_l^{PP}(r)\rangle \langle R_l^{PP}(r) \Delta V_l(r)|}{\langle R_l^{PP}(r) | \Delta V_l(r) | R_l^{PP}(r) \rangle}. \quad (2.19)$$

In this form of the non-local potential each component of the pseudo wave function is projected onto a single basis state. When it is applied to pseudo-atoms it gives identical results to the semi-local form, independent of local potential part. However, in another environment, the wave function does not project onto a radially complete set of spherical harmonics. It has been found that with the Kleinman-Bylander approach, the transferability of the pseudopotentials can be altered due to the appearance of accidental spurious states (ghost states) (Gonze *et al.*, 1990, 1991). Therefore it is important to consider the transferability of the pseudopotentials in the Kleinman-Bylander form in order to ensure that fully non-local pseudopotentials do not present ghost states.

2.3.5 Core-valence exchange-correlation

Although the exchange-correlation is a non-linear functional of the electron density, the complete linearisation of its core-valence contribution is the most common approximation and it has proven to be accurate in a great number of applications with both the LDA and GGA approximations. However, an explicit account of the core-valence non-linearity of E_{xc} is sometimes required, for instance in the study of materials with few valence electrons such as alkaline metal atoms, or for spin-density functional theory (Louie *et al.*, 1982; Fuchs *et al.*, 1998). Instead of a full core density, it suffices to add a so-called partial core density $\tilde{\rho}_{partial}^{core}$ as suggested Louie *et al.* (1982). Therefore the effect of core electrons on the exchange-correlation energy is described by a partial core given by

$$\tilde{\rho}_{partial}^{core} = \begin{cases} \rho^{core} & \text{for } r \geq r_0 \\ \frac{a}{r} \sin(br) & \text{for } r < r_0 \end{cases} \quad (2.20)$$

where ρ^{core} is the core density, r_0 is a cut-off radius and a and b are constants which guarantee the continuity of $\tilde{\rho}_{partial}^{core}$ and its first derivative at r_0 . This procedure removes the sharply peaked structure near the nucleus and allows for smooth exchange-correlation potentials to be obtained for both the LDA and GGA approximations. A frequently used choice of the cut-off radius is to take the value where the core density is from one to two times larger than the valence charge density (Louie *et al.*, 1982). We have selected a radius where the densities are equal.

2.4 Total crystal energy for periodic systems

Before starting to apply density functional theory to finding the ground state of electrons moving in a crystalline field, a difficulty must be overcome. There is a

large number of electrons in the crystal whose wave functions are extended throughout the whole crystal. As a consequence, a direct solution of the Kohn-Sham equation is impossible. Fortunately, if the translation symmetry of the solid is exploited, the size of problem is reduced. Bloch's theorem allows us to represent the electronic wave function of the i th state as the product of a plane wave with wave vector \mathbf{k} inside the first Brillouin zone, modulated by a periodic function, u_i , (Ashcroft & Mermin, 1976)

$$\psi_{i\mathbf{k}}(\mathbf{r}) = \exp(i\mathbf{k} \cdot \mathbf{r})u_i(\mathbf{r}). \quad (2.21)$$

As consequence of equation (2.21), knowledge of the wave function within one unit cell determines it throughout space in a periodic material.

Ihm *et al.* (1979) have derived a formalism for performing self-consistent total energy calculations for periodic systems using a plane wave basis set within the pseudopotential method. This can also be extended to a mixed basis set (combination of plane wave and localised orbitals, see section 2.5). The application of the total energy method to solids allows the prediction of a wide variety of properties of materials including the cohesive energy, lattice constant, bulk modulus, crystal structure and its phase transitions, phonons, surface properties, chemisorption, interfaces, and defects which can be compared with experimental results (Ihm, 1988). The total crystal energy of a system whose nuclei are located at $\{\mathbf{R}_I\}$ is defined as the sum of the electronic energy, E , and the lattice (ion-ion) energy, $E_{ion-ion}$,

$$E_{total}[\rho, V_{ext}] = E[\rho, V_{ext}] + E_{ion-ion}(\{\mathbf{R}_I\}). \quad (2.22)$$

Using equation (2.3), we obtain

$$E_{total}[\rho, V_{ext}] = T_s + \int \rho(\mathbf{r})V_{ext}(\mathbf{r})d^3\mathbf{r} + E_H[\rho] + E_{xc}[\rho] + E_{ion-ion}(\{\mathbf{R}_I\}) \quad (2.23)$$

where the kinetic energy term is given by

$$T_s = \sum_i \int f_i \psi_i^*(\mathbf{r}) \left(-\frac{1}{2} \nabla^2 \right) \psi_i(\mathbf{r}) d^3\mathbf{r}, \quad (2.24)$$

where E_H is the Hartree energy and the lattice energy or the Madelung energy of the ions is given by

$$E_{ion-ion} = \frac{1}{2} \sum_{I,J \neq I} \frac{Z_I Z_J}{|\mathbf{R}_I - \mathbf{R}_J|}, \quad (2.25)$$

where Z_I and Z_J are the effective charges of the ion cores.

The integral of ρV_{ext} represents the interaction energy between ions and electrons. As was indicated in section 2.3, an important simplification can be made if it is assumed that only the valence electrons contribute to the physical properties. Then the effect of the cores on the valence electrons can be replaced by pseudopotentials. For crystalline systems, the potential V_{ext} is constructed as lattice sum of the individual pseudopotentials

$$V_{ext}(\mathbf{r}) = \sum_{\mathbf{R}} \sum_n V_{ion,n}^{PP}(\mathbf{r} - \mathbf{R} - \tau_n), \quad (2.26)$$

where \mathbf{R} are the lattice vectors and τ_n is the position of an ion within the unit cell. The pseudopotential is normally divided into a local and a non-local, but separable, part. See subsection 2.3.4.

2.4.1 Plane wave basis sets

A plane wave basis set gives a natural representation for periodic systems and it has been used successfully to calculate the ground state properties of materials. The use of plane waves for expanding the electronic wave function provides a homogeneous basis set, independent of the atomic positions, giving an unbiased description of

the simulation which avoids the Pulay term (Pulay, 1969) in the calculation of ionic forces. Additionally, the accuracy of results can be improved by a single parameter, the cut-off energy, E_{cut} . The expansion of the Bloch function in terms of plane waves leads to the following representation for the electronic wave function

$$\psi_{i\mathbf{k}}(\mathbf{r}) = \frac{1}{\sqrt{\Omega}} \sum_{\mathbf{G}} b_{\mathbf{G}}^i \exp(i(\mathbf{k} + \mathbf{G}) \cdot \mathbf{r}), \quad (2.27)$$

where \mathbf{G} are reciprocal lattice vectors; \mathbf{k} is a wave vector in the first Brillouin zone, Ω is the crystal volume and $b_{\mathbf{G}}^i$ are the expansion coefficients. In principle an infinite number of plane waves are needed to expand the electronic wave function. However, in practical calculations the sum is truncated, including only plane waves with a kinetic energy defined by $1/2 |\mathbf{G} + \mathbf{k}|^2 < E_{cut}(\text{Hartree})$, where the cut-off energy E_{cut} determines the convergence of the calculations.

2.4.2 Brillouin zone integration

Total energy calculations involve integrations of quantities (charge density, total energy, etc.) over the Brillouin zone (BZ). By Bloch's theorem, the average of a quantity Q can be written as (Ashcroft & Mermin, 1976)

$$Q = \frac{\Omega}{(2\pi)^3} \int_{BZ} Q_{\mathbf{k}} d^3\mathbf{k}, \quad (2.28)$$

where Ω is the unit cell volume. This integral requires knowledge of the function $Q_{\mathbf{k}}$ at a set of \mathbf{k} -points in the entire BZ but symmetry arguments can be used to justify sampling only inside the irreducible part of BZ. Several methods have been developed (Chadi & Cohen, 1973; Cunningham, 1974; Monkhorst & Pack, 1976; Moreno & Soler, 1992; Hama & Watanabe, 1992) for determining a special set of \mathbf{k} -points in the BZ, which allow us to calculate the average Q with an arbitrary

degree of accuracy with a given number of sampled \mathbf{k} -points. Each of these schemes provide a homogeneous set of \mathbf{k} -points which depend on the lattice unit cell and its symmetry. The most widely used method is the Monkhorst-Pack scheme. Within this model a uniform mesh of \mathbf{k} -points is defined by a set of 3 integers N_1 , N_2 , and N_3 which determine the density of \mathbf{k} -points in each primitive reciprocal-lattice direction. A general \mathbf{k} -point is given by

$$\mathbf{k}_{rst} = U_{1r}\mathbf{G}_1 + U_{2s}\mathbf{G}_2 + U_{3t}\mathbf{G}_3 \quad (2.29)$$

where \mathbf{G}_i are the reciprocal lattice vectors and U_{ip} are weighting factors defined by

$$U_{ip} = \frac{2p - N_i - 1}{2N_i} \quad (2.30)$$

where p runs from 1 to N_i . The mesh defines $N_1N_2N_3$ \mathbf{k} -points in the entire Brillouin zone and the integration in equation (2.28) is replaced by a sum over a discrete set of \mathbf{k} -points

$$Q = \frac{1}{N_1N_2N_3} \sum_{rst} Q_{\mathbf{k}_{rst}}. \quad (2.31)$$

It often occurs that some members of the \mathbf{k} -point set are symmetry-related by a point group operation of the crystal. If several \mathbf{k} -points are symmetry-related, then the Kohn-Sham equations need to be solved only for a single member of the symmetry-related set.

2.4.3 Kohn-Sham Hamiltonian within a plane wave basis set

By solving the Kohn-Sham equations using equations (2.27), we can show that the expansion coefficients $b_{\mathbf{G}+\mathbf{k}}^\alpha$ satisfy the following eigenvalue problem

$$\sum_{\mathbf{G}'} \mathbf{H}_{\mathbf{G}\mathbf{G}'}^{\mathbf{k}} b_{\mathbf{G}'+\mathbf{k}}^i = E_{i,\mathbf{k}} b_{\mathbf{G}+\mathbf{k}}^i, \quad (2.32)$$

where the momentum-space Hamiltonian matrix elements are defined by

$$\mathbf{H}_{\mathbf{G}\mathbf{G}'}^{\mathbf{k}} = \frac{1}{2}(\mathbf{k} + \mathbf{G})^2 \delta_{\mathbf{G}\mathbf{G}'} + V_H(\mathbf{G} - \mathbf{G}') + V_{xc}(\mathbf{G} - \mathbf{G}') + V_{ion}^{PP}(\mathbf{k} + \mathbf{G}, \mathbf{k} + \mathbf{G}') \quad (2.33)$$

where the Hartree potential, $V_H(\mathbf{G} - \mathbf{G}')$, the exchange-correlation potential, $V_{xc}(\mathbf{G} - \mathbf{G}')$, and the ion-electron potential, $V_{ion}^{PP}(\mathbf{k} + \mathbf{G}, \mathbf{k} + \mathbf{G}')$, are expressed in term of their Fourier components.

The size of the secular equation (2.32) is defined by the number of plane waves. A conventional scheme of diagonalisation it is not the best way to solve the Hamiltonian especially when a large system is treated. The computational demand depends on the third power of number of the plane waves while the storage requirement is approximately the square of the number of plane waves (Press *et al.*, 1992). This restricts the application of exact diagonalisation for a plane wave basis to very small systems. Because of this, new iterative diagonalisation approaches have been developed that allow the minimisation of the total energy in a more efficient manner (Car & Parrinello, 1985; Štich *et al.*, 1989; Teter *et al.*, 1989; Gillan, 1989; Kresse & Furthmüller, 1996b).

2.4.4 Conjugate gradients

It is well-known that direct methods for determining the minimum of the Kohn-Sham energy functional are more efficient than those based on diagonalisation (Teter *et al.*, 1989). The simplest way to perform the minimisation is by changing the approximated wave function along the gradient. However by moving the trial wave function towards the minimum there is no guarantee that the lowest energy point can be reached in a finite number of steps. The search can be improved by using information from previous steps to calculate the best minimisation route, this strategy is known as the conjugate gradient method (Gillan, 1989). In principle, this scheme could update all the electronic wave functions simultaneously, but a large amount of data must be stored between iterations to ensure the conjugacy of the search. Due to this difficulty, the search is normally carried out for a single band at a time (band by band method) and moving in a direction orthogonal to all the other bands. Although a small storage is required, the charge density and the potential must be recalculated after each single band update. The wave function components with large momentum will have a large gradient, and the kinetic energy in the Hamiltonian will be dominated by these states. In order to remove this problem a preconditioned gradient vector is used (Payne *et al.*, 1992).

2.4.5 Symmetrised charge density

Another advantage of a plane wave basis set is that the fast Fourier transform (FFT) can be applied to transfer quantities from real space to reciprocal space and vice versa. For instance, within the self-consistent approach, the charge density is an important quantity to be calculated, and its form in the reciprocal space is very computationally demanding. An efficient way to evaluate it is by performing the calculation of the charge density in real space (on a grid of points \mathbf{r}_i) and then to

calculate its reciprocal space representation by a Fourier transform

$$\rho^{(\mathbf{G})} = \sum_i \exp(-i\mathbf{G} \cdot \mathbf{r}_i) \rho(\mathbf{r}_i). \quad (2.34)$$

The charge density in real space, $\rho(\mathbf{r})$, is calculated by

$$\rho(\mathbf{r}) = \sum_{\mathbf{k}_s} \omega_{\mathbf{k}_s} \left[\frac{1}{N_T} \sum_{\alpha \in T} \rho_{\mathbf{k}_s}(\mathbf{S}_\alpha^{-1} \mathbf{r}) \right], \quad (2.35)$$

where $\omega_{\mathbf{k}_s}$ is the weighting factors of the special \mathbf{k}_s -vectors, the factor in brackets represents the symmetrised charge density in real space with respect to the space group of the crystal, and N_T is the number of operations α in the point group T .

2.4.6 Metallic systems and free energy

For systems with completely filled bands, the substitution of the integral over the Brillouin zone, equation (2.28), by the sum over a mesh of \mathbf{k} -points, equation (2.31), is an efficient approximation. However, for metallic systems the convergence with respect to the number of \mathbf{k} -points becomes slow and instabilities can arise in the self-consistent procedure. This is due to the occupancies changing discontinuously from 1 to 0 at the Fermi level. One way to improve the convergence with respect to the number of \mathbf{k} -points is to allow the occupation number to vary continuously through the Fermi level. When a broadening method is adopted, it is more convenient to work with a scheme of non-zero temperature (Mermin, 1965; Gillan, 1989). Therefore the electron density of the ground state does not minimise the functional of the total energy, equation (2.23), but the functional of the free energy, F , at finite temperature, which can be written

$$F = E_{total} - T \sum_i S(f_i). \quad (2.36)$$

Here S is the entropy of non-interacting electrons associated with the i -orbital with occupation number f_i at temperature T . Normally, it is convenient to use an artificially high temperature (typically $k_b T = 0.25$ eV) since a broadening of the occupation number improves the stability and speeds up the convergence of the calculations. The entropy function can be chosen with some arbitrariness (it depends on the distribution function adopted). We have used a spline of Gaussians (White *et al.*, 1996), which allows the occupancy to fall off more quickly with energy than a Fermi-Dirac distribution. Our final plane wave code is that described in White *et al.* (1996).

2.4.7 Supercell approximation

This approximation allows a system of any dimensionality to be studied. For instance, a molecule in a box can be treated as a periodic system. In principle, there are no limitations on the shape of the unit cell used (Bird & Gravil, 1997). The supercell approximation has been shown to be an useful tool for modelling the adsorption of atoms or molecules on clean surfaces. The semi-infinite crystal is replaced by a slab with two surfaces. To model static adsorption, a two-dimensional array of adsorbate atoms is set on one of the two surfaces. In this way, we have a two-dimensional lattice which is finite in the direction perpendicular to the surface. To recover periodicity in this direction, the slabs are repeated and a vacuum region is added between them. In order to avoid interactions between different slabs, the vacuum region must be wide enough. On the other hand, to obtain the electronic structure representative of the real system, the slab should be sufficiently thick so that all relevant quantities will be independent of thickness. In summary, the supercell approximation allows us to study an aperiodic system using Bloch's theorem.

2.5 Mixed basis approach

Although the pseudopotential-plane-wave method has allowed us to study systems containing 3d transition or first row-elements, it is still inefficient due to the large number of plane waves needed to represent the localised states in these systems. An alternative method to solve this problem is to expand the Kohn-Sham eigenfunctions in terms of a combination of localised functions and plane waves, (Louie *et al.*, 1979; Gülseren *et al.*, 1998). We write

$$\psi_{i\mathbf{k}}(\mathbf{r}) = \sum_{\mu} a_{\mu}^i \chi_{\mu}(\mathbf{r}) + \frac{1}{\sqrt{\Omega}} \sum_{\mathbf{G}} a_{\mathbf{G}}^i \exp(i(\mathbf{k} + \mathbf{G}) \cdot \mathbf{r}) \quad (2.37)$$

where i is the band index; μ is a combined index which represents the orbitals and the atomic sites, a_{μ} and $a_{\mathbf{G}}$ are coefficients of the pseudo-atomic orbitals and plane waves respectively, \mathbf{G} are reciprocal-lattice vectors, and Ω is the crystal volume. The localised part of equation (2.37) is defined by a Bloch sum

$$\chi_{\mu}(\mathbf{r}) \equiv \chi_m^n(\mathbf{r}) = \sum_{\mathbf{R}} \exp(i\mathbf{k} \cdot (\mathbf{R} + \tau_n)) \phi_m(\mathbf{r} - \mathbf{R} - \tau_n), \quad (2.38)$$

where m represents the orbitals; τ_n is the position of an atom within the unit cell, and ϕ_m are the pseudo-atomic orbitals.

Inserting (2.37) into the Kohn-Sham equations leads to the following matrix eigenvalue problem for each \mathbf{k} vector,

$$(\mathbf{H} - \mathbf{E}\mathbf{S})\mathbf{U} = 0, \quad (2.39)$$

where \mathbf{H} and \mathbf{S} represent the Hamiltonian and overlap matrices respectively. \mathbf{E} is a diagonal matrix containing the eigenvalues $E_{i,\mathbf{k}}$ of \mathbf{H} , the eigenvector \mathbf{U} contains the expansion coefficients a_{μ}^i and $a_{\mathbf{G}}^i$. Within the mixed basis scheme, the Hamiltonian

matrix and overlap matrix have the following structure

$$\begin{bmatrix} [\mathbf{A}_{\mu\mu}] & [\mathbf{A}_{\mu\mathbf{G}}] \\ [\mathbf{A}_{\mu\mathbf{G}}^*] & [\mathbf{A}_{\mathbf{G}\mathbf{G}}] \end{bmatrix}$$

where $[\mathbf{A}_{\mu\mu}]$, $[\mathbf{A}_{\mu\mathbf{G}}]$ and $[\mathbf{A}_{\mathbf{G}\mathbf{G}}]$ are the parts based on atomic-orbital-atomic-orbital representation, atomic-orbital-plane-wave representation, and plane-wave-plane-wave representation respectively.

The adoption of the momentum space approach facilitates the evaluation of the matrix elements of \mathbf{H} and \mathbf{S} . Here, the localised part of equation (2.37) is expanded in terms of plane waves, which leads to the electronic wave function to be written as follows

$$\begin{aligned} \psi_{i\mathbf{k}}(\mathbf{r}) &= \frac{1}{\sqrt{\Omega}} \sum_{i,m,\mathbf{G}} a_{\mu}^i(\mathbf{k}) \exp(-i\mathbf{G} \cdot \tau_n) I_{\mathbf{G}}^m(\mathbf{k}) \exp(i(\mathbf{k} + \mathbf{G}) \cdot \mathbf{r}) \\ &\quad + \frac{1}{\sqrt{\Omega}} \sum_{\mathbf{G}} a_{\mathbf{G}}^i \exp(i(\mathbf{k} + \mathbf{G}) \cdot \mathbf{r}) \end{aligned} \quad (2.40)$$

where the Fourier integral of the atomic orbitals is given by

$$I_{\mathbf{G}}^m(\mathbf{k}) = \frac{1}{\sqrt{\Omega}} \int \exp(-i(\mathbf{k} + \mathbf{G}) \cdot \mathbf{r}) \phi_m(\mathbf{r}) d\Omega. \quad (2.41)$$

The first term on the right hand side of the equation (2.40) needs a much bigger number of plane wave than the second one. Although the dimension of the Hamiltonian and overlap matrices is not increased, the construction of the matrix elements consumes a considerable amount of computing time. Note that plane wave cut-off in the first term in equation (2.40) is the same as in the corresponding pure plane wave calculation.

The overlap matrix is not diagonal; its elements are

$$\mathbf{S}_{\mathbf{G},\mathbf{G}'}(\mathbf{k}) = \delta_{\mathbf{G},\mathbf{G}'}, \quad (2.42)$$

$$\mathbf{S}_{\mu,\mathbf{G}}(\mathbf{k}) = \exp(-i\mathbf{G} \cdot \tau_{\mathbf{n}}) I_{\mathbf{G}}^m(\mathbf{k}) \quad (2.43)$$

and

$$\mathbf{S}_{\mu,\mu'}(\mathbf{k}) = \sum_{\mathbf{G}} \exp(i\mathbf{G} \cdot (\tau_{\mathbf{n}'} - \tau_{\mathbf{n}})) I_{\mathbf{G}}^{*m'}(\mathbf{k}) I_{\mathbf{G}}^m(\mathbf{k}). \quad (2.44)$$

The Hamiltonian matrix elements are defined by

$$\mathbf{H}_{\mu,\mu'}(\mathbf{k}) = \sum_{\mathbf{G},\mathbf{G}'} \exp(-i\mathbf{G}' \cdot \tau_{\mathbf{n}'}) \exp(i\mathbf{G} \cdot \tau_{\mathbf{n}}) I_{\mathbf{G}'}^{*m'}(\mathbf{k}) I_{\mathbf{G}}^m(\mathbf{k}) \mathbf{H}_{\mathbf{G},\mathbf{G}'} \quad (2.45)$$

and

$$\mathbf{H}_{\mu,\mathbf{G}}(\mathbf{k}) = \sum_{\mathbf{G}'} \exp(-i\mathbf{G}' \cdot \tau_{\mathbf{n}}) I_{\mathbf{G}'}^m(\mathbf{k}) \mathbf{H}_{\mathbf{G},\mathbf{G}'}, \quad (2.46)$$

where $\mathbf{H}_{\mathbf{G},\mathbf{G}'}$ is given by equation (2.33). Within the mixed basis scheme the size of the secular equation (equation (2.39)) is approximately equal to the number of atoms per unit cell times the number of orbitals, plus the plane wave part, which is roughly twenty plane waves per atom. For the systems studied in the present work, the Kohn-Sham Hamiltonians were less than $10^3 \times 10^3$ in size and they were solved following a standard diagonalisation procedure (Press *et al.*, 1992). This has been combined with a charge density mixing scheme, providing an efficient way to achieve self-consistency. More details about this methodology will be presented in the following subsections.

2.5.1 Self-consistent field

In total energy calculations based on a density functional theory formalism, the charge density and the band energy $E_{i,\mathbf{k}}$ are obtained by solving self-consistently

the Kohn-Sham equations for different \mathbf{k} -points in the first Brillouin zone. By taking into account the symmetry present in the problem, the number of \mathbf{k} -points can be reduced during the evaluation of the valence charge density

$$\rho(\mathbf{r}) = \sum_{i,\mathbf{k}} \omega_{\mathbf{k}} f_{i,\mathbf{k}} |\psi_{i\mathbf{k}}(\mathbf{r})|^2, \quad (2.47)$$

where $\omega_{\mathbf{k}}$ are weighting factors of the \mathbf{k} -points in the irreducible part of the first Brillouin zone. The charge density computed from equation (2.47) depends non-linearly on the effective potential, equation (2.5), and the solution must be found by using iterative techniques. For many cases, the iterative procedure can diverge, indeed it is possible to obtain an oscillating charge density with a growing amplitude. Therefore in order to achieve convergence, such oscillations must be damped. The most common damping procedure combines a portion of the input and output charge density of the last iteration (Bendt & Zunger, 1982). At each iteration step n , a new charge density for the $(n + 1)$ th iteration is obtained by mixing the input and the output charge density as follows:

$$\rho_{input}^{n+1} = \rho_{input}^n + \alpha(\rho_{output}^n - \rho_{input}^n) \quad (2.48)$$

By a suitable choice of the mixing parameter, α , between 0 and 1, convergence usually can be achieved. However there are cases where this is not true or where the iteration process converges slowly and many iterations are needed. Normally each iteration requires a lot of computing time, therefore it is important to find methods to accelerate the convergence. Several efforts have been made to improve the convergence of iteration schemes based on simple mixing (Ferreira, 1980; Akai & Dederichs, 1985). However, the results have not been satisfactory in comparison with methods based on a quasi-Newton Raphson scheme, where a significant reduction in the number of iterations can be obtained (Vanderbilt & Louie, 1984; Johnson, 1988; Eyert, 1996).

2.5.2 Broyden's method

In general, an iterative procedure is defined by a non-linear operator which is applied to n th charge density input vector $|\rho_{input}^n\rangle$ and produces the output vector $|\rho_{output}^n\rangle$. If self-consistency is achieved, the residual vector

$$|R^n\rangle = |\rho_{output}^n\rangle - |\rho_{input}^n\rangle \quad (2.49)$$

vanishes. The length of the residual vector is used as a measure of the convergence reached, so then a norm in the space spanned by the input and output is defined. Within the quasi-Newton Raphson approximation, the residual vector is expanded in term of input vector and the subsequent residual vector is calculated by (Eyert, 1996)

$$|R^{n+1}\rangle = |R^n\rangle + \mathbf{J}^n (|\rho^{n+1}\rangle - |\rho^n\rangle), \quad (2.50)$$

where the Jacobian matrix is defined as $\mathbf{J}_{ij}^n = \frac{\partial R_i^n}{\partial \rho_j}$. If the left-hand side of equation (2.50) vanishes, the new input density is given by

$$|\rho^{n+1}\rangle = |\rho^n\rangle - \mathbf{G}^n |R^n\rangle. \quad (2.51)$$

where $\mathbf{G}^n = (\mathbf{J}^n)^{-1}$. In the Broyden approximation one tries to find an approximation of the inverse Jacobian matrix by updating it at each iteration. The Broyden method has a serious problem for large systems, due to the need to store the \mathbf{G}^n matrix (Vanderbilt & Louie, 1984).

Johnson (1988) proposed an efficient way to calculate the inverse Jacobian matrix that avoids the requirement to store it, and where the updating of the inverse Jacobian matrix, \mathbf{G}^{n+1} is calculated by a least-square minimisation of

$$E = \omega_0^2 \|\mathbf{G}^{n+1} - \mathbf{G}^n\|^2 + \sum_{n=1}^m \omega_n^2 \| |\Delta\rho^n\rangle + \mathbf{G}^{n+1} |\Delta R^n\rangle \|^2. \quad (2.52)$$

The parameters ω are considered free parameters and they are fitted in order to achieve an optimal convergence. $\|A\|^2 = \langle A | A \rangle$. $|\Delta\rho^n\rangle$ and $|\Delta R^n\rangle$ are defined as $|\Delta\rho^{n+1}\rangle - |\Delta\rho^n\rangle$ and $|\Delta R^{n+1}\rangle - |\Delta R^n\rangle$ respectively. Minimisation with respect to the inverse Jacobian matrix leads to the updated inverse Jacobian given by (Johnson, 1988; Kresse & Furthmüller, 1996b)

$$\mathbf{G}^{n+1} = \mathbf{G}^n - \sum_{k,n=1}^m \beta_{kn} \left(\mathbf{G}^n |\Delta R^k\rangle + |\Delta\rho^n\rangle \right) \langle \Delta R^k|. \quad (2.53)$$

Writing \mathbf{G}^{n+1} in term of \mathbf{G}^1 , we obtain

$$\mathbf{G}^{n+1} = \mathbf{G}^1 - \sum_{k=1}^m |Z_k^m\rangle \langle \Delta R^k|, \quad (2.54)$$

where

$$|Z_k^m\rangle = \sum_{n=1}^m \beta_{kn} \omega_k \omega_n |U^n\rangle + \sum_{k=1}^{m-1} \beta_{kn} |Z_k^{m-1}\rangle, \quad (2.55)$$

$$|U^n\rangle = \mathbf{G}^1 |\Delta R^n\rangle + |\Delta\rho^n\rangle, \quad (2.56)$$

$$\beta_{kn} = \left(\omega_0^2 I + a \right)_{kn}^{-1} \quad (2.57)$$

and

$$a_{ij} = \omega_i \omega_j |\Delta R^i\rangle \langle \Delta R^j|. \quad (2.58)$$

The efficiency of the scheme depends on providing a good starting approximation to the charge density. One way to do this involves the use of the Kerker's charge mixing scheme (Kerker, 1980a) for the first few self-consistent steps and then to continue the minimisation with Broyden method. This scheme was used to minimise the total energy with the mixed basis set method.

2.5.3 Kerker's mixing scheme and preconditioning

As pointed out in previous section, for total energy calculations based on the mixed-basis approach, we have adopted a self-consistency process based on the modified Broyden scheme (Johnson, 1988) combined with a scheme of Kerker charge mixing (Kerker, 1980a) for the first few iterations

$$\rho_{in}^{m+1}(G) = \rho_{in}^m(G) + A \frac{G^2}{G^2 + G_0^2} \left[\rho_{out}^m(G) - \rho_{in}^m(G) \right]. \quad (2.59)$$

Within this scheme, the oscillations in low-G components of the charge density are damped. For small wave vectors, a small amount of the output charge density is mixed while at high-G, a simple linear mixing with a mixing parameter, A , is carried out.

A reduction in the number of iterations is important especially for large systems where a great amount of computational time is required for each iterative step. Kresse & Furthmüller (1996b) have introduced a metric, g_{ij} , for the evaluation of the dot products present in Broyden's mixing scheme;

$$\langle a | b \rangle = \sum_{i,j} a_i g_{ij} b_j. \quad (2.60)$$

The idea is to try to find a metric that decreases the number of iterations required. We have tested the metric given by Kresse & Furthmüller (1996b) in the calculations of the total energy of the Xe/Pt system, see section 4.3.

2.5.4 Projected density of states

A way of studying bonding is via the projected density of states. This is defined as the density of states associated with the eigenstate $|\psi_i\rangle$

$$d^i(E) = \sum_{\mathbf{k}} |\langle \psi_i | \psi_{\mathbf{k}} \rangle|^2 \delta(E - E_{\mathbf{k}}). \quad (2.61)$$

The sum runs over all the states of the system, and the δ -function picks out those states with energy E . In the case where $|\psi_i\rangle$ is part of a plane wave basis set, this does not provide an efficient way to quantify the local atomic population. Sánchez-Portal *et al.* (1996) have derived a formalism for projecting plane waves onto atomic orbitals, which has allowed a description of the properties of the system in terms of a chemical language (Sánchez-Portal *et al.*, 1996; Segall *et al.*, 1996; Börnsen *et al.*, 1999).

To analyse the bonding in our molecule-surface systems we need to calculate the population of the atomic orbitals using the mixed basis set (see equation (2.37) and (2.38)). We find that the projected density of states that is equivalent to that reported by Sánchez-Portal *et al.* (1996) becomes

$$d^i(E) = \sum_{\alpha\mathbf{k}} \sum_j a_j^{\alpha*} S_{ji} a_i^\alpha \delta(E - E_{\alpha\mathbf{k}}), \quad (2.62)$$

where a are the coefficients of the pseudo-atomic orbitals and plane waves, i and j label the basis functions in equation (2.37) (i.e. either a pseudo-atomic orbital μ , or a low-energy plane-wave \mathbf{G}), α runs over the electronic energies and S_{ji} is the overlap matrix connecting basis functions. With this definition, the total density of states is exactly the sum of $d^i(E)$ over all basis states, and so the total charge

associated with any basis function can be defined by

$$Q^i = \int d^i(E)dE. \quad (2.63)$$

This is equivalent to the charge of the orbital i within Mulliken's analysis (Mulliken, 1955). In practice, we will be most interested in projections onto the pseudo-atomic orbitals, but within the mixed-basis approach the plane-wave parts are also present. A description of the binding mechanism of an Xe atom on the Pt(111) surface is given in subsection 4.6.1.

2.6 Ultrasoft pseudopotentials

Norm-conserving pseudopotentials are accurate, but for the elements of the first row and 3d transition metals they need high cut-off energies. Vanderbilt (1990) has overcome this difficulty by relaxing the norm-conserving condition, which allows us to define a much softer pseudo wave function within the core region. The electronic charge density is divided into a hard part localised in the core region and a smooth contribution outside. Inside the core region the charge density is augmented in order to recover the full electronic charge density. The augmented part appears in the density only, not in the wave function, so that pseudopotentials are softer than in the norm-conserving case. Similarly to other *ab-initio* pseudopotential schemes, the construction of the ultrasoft potential starts with an all-electron calculation for the free atom in some reference configuration, in order to obtain the eigenvalues ϵ_l^{AE} and eigenfunctions ψ_l^{AE} for a screened potential V^{AE} . For each ψ_l^{AE} , a pseudo wave function ϕ_l is constructed with the only constraint that it joins smoothly to ψ_l^{AE} at a cut-off radius r_{cl} and no norm-conservation constraint is explicitly imposed.

The pseudo wave function ϕ_l satisfies the secular equation

$$\left(-\frac{\nabla^2}{2} + V^{local} + V^{NL}\right) |\phi_l\rangle = \varepsilon_l \mathbf{S} |\phi_l\rangle. \quad (2.64)$$

The overlap operator \mathbf{S} is given by

$$\mathbf{S} = 1 + \sum_{nm} q_{nm} |\beta_n\rangle \langle \beta_m| \quad (2.65)$$

with $q_{nm} = \int Q_{nm} dr$, Q_{nm} being the augmentation charge density defined by

$$Q_{nm}(\mathbf{r}) = \psi_n^{*AE}(\mathbf{r}) \psi_m^{AE}(\mathbf{r}) - \phi_n^*(\mathbf{r}) \phi_m(\mathbf{r}). \quad (2.66)$$

The functions β_n satisfy the orthogonality relation $\langle \phi_j | \beta_n \rangle = \delta_{jn}$, and are defined as

$$|\beta_n\rangle = \sum_j (B^{-1})_{jn} |\chi_j\rangle \quad (2.67)$$

where

$$B_{jn} = \langle \phi_j | \chi_n \rangle. \quad (2.68)$$

For each pseudo wave function ϕ_l one defines a function χ_l by

$$|\chi_l\rangle = \left(\varepsilon_l + \frac{\nabla^2}{2} - V^{local}\right) |\phi_l\rangle, \quad (2.69)$$

where the local potential V^{local} matches smoothly to V^{AE} at a cut-off radius r_c^{local} and consists of a local ion-electron potential, V_{ion}^{local} , the Hartree potential and the exchange-correlation potential

$$V^{local}(\mathbf{r}) = V_{ion}^{local}(\mathbf{r}) + \int \frac{\rho(\mathbf{r}') d\mathbf{r}'}{|\mathbf{r} - \mathbf{r}'|} + \frac{\delta E_{xc}[\rho]}{\delta \rho(\mathbf{r})}. \quad (2.70)$$

The term V^{NL} in equation (2.64) represents a fully non-local potential defined by

$$V^{NL}(\mathbf{r}) = \sum_{nm} D_{nm} |\beta_n\rangle\langle\beta_m|, \quad (2.71)$$

where

$$D_{nm} = B_{nm} + \varepsilon_m q_{nm}. \quad (2.72)$$

The numbers n and m run over the number of β functions. Typically, for each angular momentum channel, two reference energies are included. This implies that the number of projections is twice as large as for a corresponding Kleinman-Bylander norm-conserving pseudopotential. The inclusion of more than one reference energy ε per quantum state allows a good transferability over a wide energy range even for larger cut-off radii (Vanderbilt, 1990).

Within the ultrasoft pseudopotential scheme the total crystal energy is given by (Laasonen *et al.*, 1993; Fujiwara & Hoshi, 1997)

$$\begin{aligned} E_{total}[\rho, \{\mathbf{R}_I\}] &= \sum_i \langle\phi_i| \left[-\frac{\nabla^2}{2} + \sum_{nm} \sum_{\mathbf{R}\tau_j} D_{nm}^{\mathbf{R}\tau_j} |\beta_n^{\mathbf{R}\tau_j}\rangle\langle\beta_m^{\mathbf{R}\tau_j}| \right] |\phi_i\rangle + E_H[\rho] \\ &+ E_{xc}[\rho] + \int V_{ion}^{local}(\mathbf{r})\rho(\mathbf{r})d\mathbf{r} + E_{ion-ion}(\{\mathbf{R}_I\}) \end{aligned} \quad (2.73)$$

where the charge density, ρ , is defined by

$$\rho(\mathbf{r}) = \sum_i \left[|\phi_i(\mathbf{r})|^2 + \sum_{nm} \sum_{\mathbf{R}\tau_j} Q_{nm}^{\mathbf{R}\tau_j}(\mathbf{r}) \langle\phi_i| \beta_n^{\mathbf{R}\tau_j}\rangle\langle\beta_m^{\mathbf{R}\tau_j}| \phi_i\rangle \right], \quad (2.74)$$

where \mathbf{R} are the lattice vectors and τ_j is the position of an ion within the unit cell. The functions $A^{\mathbf{R}\tau_j}(\mathbf{r})$ depend on \mathbf{R} and τ_j through $A^{\mathbf{R}\tau_j}(\mathbf{r}) = A(\mathbf{r} - \mathbf{R} - \tau_j)$. The local part of the potential is constructed as a sum of the individual local atomic potentials

$$V_{ion}^{local}(\mathbf{r}) = \sum_{\mathbf{R}\tau_j} V_{ion}^{local}(\mathbf{r} - \mathbf{R} - \tau_j). \quad (2.75)$$

Chapter 3

Validation of the pseudopotentials

3.1 Introduction

Ab-initio pseudopotentials are useful tools in the simulation of condensed matter, facilitating the evaluation of a wide range of properties of solids and molecules with a high level of accuracy and a relatively low computational effort. In addition to the basic constraints (subsection 2.3.1) that define an *ab-initio* pseudopotential, other criteria are included in the construction process in order to improve the transferability and the efficiency of the pseudopotential (Kerker, 1980b; Rappe *et al.*, 1990; Troullier & Martins, 1991; Lin *et al.*, 1993). In the present chapter, we concentrate the discussion on those aspects present in the construction of pseudopotentials that could affect their transferability and softness.

Pseudopotentials for He, Ne, Cu, Rh, Xe, and Pt atoms were constructed following the model of Troullier & Martins (1990, 1991). We have adopted this scheme because it provides efficient pseudopotentials for a variety of elements and is one of the most widely-used, norm-conserving pseudopotential models at the present time.

For the elements Cu, Rh, Xe, and Pt, semi-relativistic pseudopotentials were constructed. It is important to take these relativistic effects into account especially for atoms with a large atomic mass because they significantly influence the electronic behaviour of the atom (Elsässer *et al.*, 1990). Another important consideration is what type of approximation should be used for describing the exchange-correlation effects. We have used both the local density approximation as parametrised by Perdew & Zunger (1981) and the generalised gradient approximation in its forms PW91 and PBE (Perdew & Wang, 1992; Perdew *et al.*, 1996b), allowing us to compare the quality of the pseudopotentials given by both approximations.

The transferability of the pseudopotentials was studied within the Kleinman-Bylander form, checking for the presence of any “false” states. Calculations of the lattice constant and bulk modulus in crystalline structures, and bond length and binding energy for rare-gas atom dimers were carried out to test the reliability of the atomically constructed pseudopotentials in predicting the equilibrium geometry in new environments.

As we pointed out in subsection 2.3.5, an approximation frequently used in an *ab-initio* pseudopotential procedure is to assume the linearity between the valence and core states. However, the outermost core states can have an important overlapping in the valence region, which affects the transferability of the pseudopotentials in a new environment (Fuchs *et al.*, 1998). Within the present study, it is important to show the effects of core-valence exchange correlation on the selected elements. For Pt, Rh, and Xe atoms, these corrections were included during the construction of the pseudopotential and the calculated structural properties were compared with results without core-valence exchange-correlation corrections.

The present chapter is organised as follow: In section 3.2, aspects of the construction of the pseudopotentials, including electronic configuration, the choosing

of core radii, the semi-relativistic approach used, and tests on the transferability of pseudopotentials with the Kleinman & Bylander form are discussed. The effects of the GGA functionals (GGA-PW91 and GGA-PBE) and the core-valence exchange-correlation energy on the pseudopotentials are presented in section 3.3. In section 3.4, the transferability of the pseudopotentials is studied by calculating the structural properties such as lattice constant and bulk modulus for the crystalline structure of Cu, Rh, and Pt and the bond length and binding energy for the dimers of He, Ne, and Xe. The calculations were carried out using the pseudopotential plane wave method and the pseudopotential mixed basis method. This section also includes further tests of the pseudopotentials, especially those related to the choosing of core radii and the effects of the exchange correlation on the calculated structural properties. Finally the conclusions of the chapter are presented in section 3.5.

3.2 Pseudopotential construction

3.2.1 Electronic configuration

Ab initio pseudopotentials are constructed from all-electron calculations for the atom in a reference configuration. In general, the construction of pseudopotentials for a bound, occupied electronic state is made from the neutral configuration. However when the atom's environment changes, its electronic configuration can also change as unoccupied states in the atom become occupied. Hence, valence states that could promote the creation of new bonding should be introduced into the pseudopotential construction. In the case of non-bound states, we have generated them from a separate atomic calculation using an ionised configuration. Table 3.1 shows ionic and neutral configurations used for each element considered.

	Ground state	Ionic state
He	$1s^2$	$1s^{0.8}p^{0.2a}, 1s^{0.8}d^{0.2b}$
Ne	$2s^22p^6$	$2s^12p^{2.5}3d^{0.25}$
Cu	$3d^{10}4s^14p^0$	$3d^94s^{0.25}4p^{0.75}$
Rh	$4d^85s^15p^0$	$4d^75s^{0.25}5p^{0.75}$
Pt	$5d^96s^16p^0$	$5d^86s^{0.25}6p^{0.75}$
Xe	$5s^25p^65d^0$	$5s^15p^{4.75}5d^{0.25}$

Table 3.1: Electronic configurations used to generate pseudopotentials for He, Ne, Cu, Rh, Pt, and Xe atoms. The ionic configuration was taken from Bachelet *et al.* (1982). a for $l = 1$, b for $l = 2$.

3.2.2 Core radii

In this section, we explain in detail the scheme adopted, which produced reliable, highly transferable pseudopotentials without the need for carrying out a large number of tests. The most important parameter within any *ab-initio* pseudopotential scheme is the core radius. Choosing core radii is in principle arbitrary; one just takes into account values greater than the last nodal point of the all-electron wave function, although care must be taken not to select too small a radius which will produce wiggles leading to poor pseudopotentials. On the other hand, core radii that are too large yield softer pseudopotentials which converge more rapidly with a plane wave basis set, but they will become less transferable. Between both extremes, there is a wide range for the core radius which produces fairly small changes in the transferability of the pseudopotentials, and it is important to have a criterion that allows us to find a balance between these extremes. In subsection 3.4.3, we will return to this point and with a particular example show how the equilibrium geometry of Pt can be altered depending on the core radius used.

When choosing the core radius the method adopted aims to optimise the pseudopotential with respect to the scattering properties of the all-electron potential. The scattering of an atomic field is closely linked with the logarithmic derivative of the wave function (Schiff, 1968), therefore a pseudopotential with a high trans-

ferability should present the same scattering as the all-electron potential around the atomic eigenvalues. With the aim of choosing core radii which provide an optimum transferability of the pseudopotentials, we have determined core radii which provide the best match between the logarithmic derivatives of the pseudo and the all-electron wave functions. The sum of the quadratic difference between pseudo and all-electron logarithmic derivatives was adopted as an error estimator

$$\sigma_l = \sqrt{\sum_{\epsilon} \left[\frac{\partial}{\partial r} \left(\ln \Psi_l^{PP}(\epsilon) \right)_{r_{ws}} - \frac{\partial}{\partial r} \left(\ln \Psi_l^{AE}(\epsilon) \right)_{r_{ws}} \right]^2}. \quad (3.1)$$

ϵ represent a discrete set of energy points (we have chosen steps of 0.01 eV) which were taken around one Rydberg either side of the eigenvalues ϵ_l . Such an energy range is quite wide and includes valence bands and lower conduction bands in solids, and it should provide a useful range to study the quality of the pseudopotential in a new environment (Fuchs & Scheffler, 1999). In principle the evaluation of the logarithmic derivative could be done using an arbitrary radius greater than the core radius, but normally the Wigner-Seitz radius, r_{ws} , is used, which is a scaled length of the interatomic separation in a metal (Sutton, 1996).

In the cases of Cu, Rh, Pt, and Xe atoms, where semi-relativistic pseudopotentials were constructed, logarithmic derivatives were calculated using the following relation (Bachelet & Schlüter, 1982)

$$\frac{\Xi'}{\Xi} = \frac{2c\xi}{\Xi} - \frac{k+1}{r}, \quad (3.2)$$

where $\Xi = F/r$ and $\xi = G/r$. F and G correspond to minor and major pseudo wave function solutions of the Dirac equation respectively. ξ is the fine structure constant, and k is a non-zero integer quantum number, whose values are defined as $k = l$ for $j = l - 1/2$ and $k = -(l + 1)$ for $j = l + 1/2$. Figure 3.1 shows the logarithmic derivative obtained for Rh. For each angular momentum component a

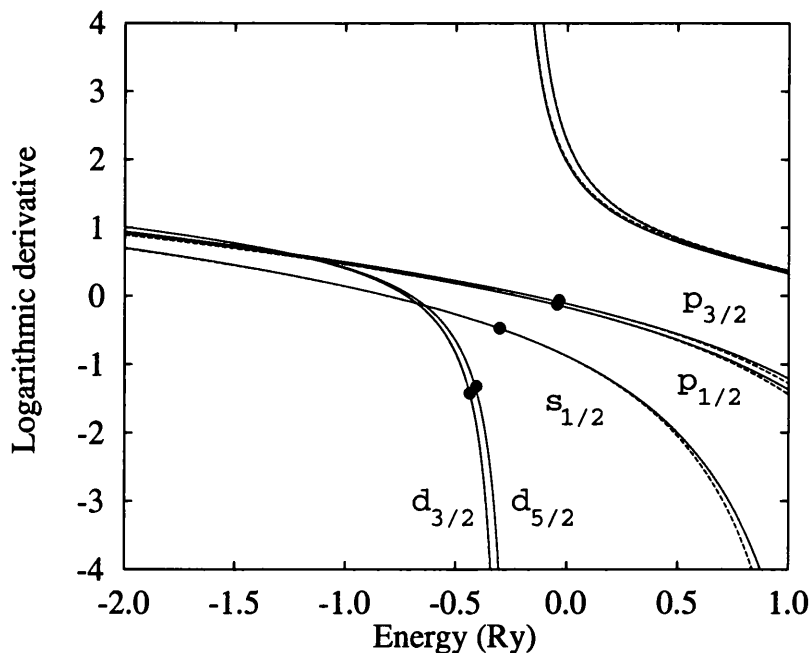


Figure 3.1: Relativistic logarithmic derivatives in $(\text{Bohr radii})^{-1}$ for Rh wave functions around the atomic eigenvalues. Solid lines represent all-electron wave function results; dashed lines represent pseudo-atom results. Bullet symbols indicate the position of the eigenvalues.

different core radius was used. This can improve the optimisation when the wave function presents a noticeable difference of phase in the valence region, as in the case of Pt $6p$ wave function (Figure 3.2). In fact we find a significant difference between the optimised core radius for these p components, see Table 3.2.

Following the variation of σ_l as a function of the core radius in the cases of Rh and Xe, Figure 3.3, it is observed that there is a core radius that minimises the function σ_l , which we have taken to be the optimised core radius. Due to the asymptotic behaviour of the logarithmic derivative curves, Figure 3.1, comparisons were made for a range between -2.0 Ry and $+1.0$ Ry for the energy and -20 $(\text{Bohr radii})^{-1}$ and 20 $(\text{Bohr radii})^{-1}$ for the values of the logarithmic derivative (although the Figure 3.1 only shows the results around the eigenvalues). This range was chosen arbitrarily but other selections do not significantly change the final results for the core radii. The optimised core radii calculated for each element are shown in Table 3.2 as are the Wigner-Seitz radii used in the logarithmic derivative calculations.

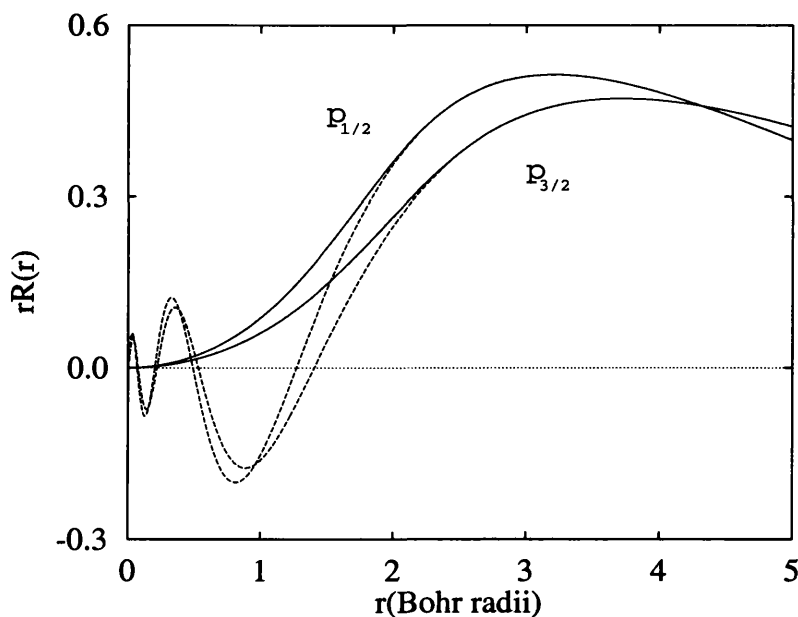


Figure 3.2: Pseudo (solid line) and all-electron (dashed line) for Pt $6p$ valence wave functions.

Atom	$s_{1/2}$	$p_{1/2}$	$p_{3/2}$	$d_{3/2}$	$d_{5/2}$	r_{ws}
Pt	2.30	2.60	2.90	2.45	2.30	2.90
Rh	2.45	2.50	2.70	2.15	1.95	2.81
Cu	1.93	2.35	2.40	2.20*	2.20*	2.60
Xe	1.73	1.90	2.00	3.80	3.90	4.57

Table 3.2: Core radii optimised from relativistic logarithmic derivative calculations for Pt, Rh, Cu, and Xe atoms. Core radii denoted with an asterisk were not optimised with equation (3.1). The Wigner-Seitz radius r_{ws} was taken from Moruzzi & Sommers (1995). Units are in Bohr radii.

We have found that this procedure provides optimum core radii for the transition metal atoms studied (Rh and Pt) and the Xe atom. For these elements, σ_l presents a minimal point, which we take as the optimum value of the core radius. However, such a minimum was not found for the Cu $3d$ pseudopotential component. A similar failure occurred for Ne $2p$ and He $1s$. In these cases, σ_l decreased monotonically as the core radius was decreased and a minimum point was not reached. Figure 3.4 shows the case of Cu. Note that for the s component (left panel), it was possible to obtain an optimised core radius but not for the d parts. The selection of the d core radii for Cu was instead made by first optimising the s and p core radii as described above. The d core radii were then varied and the lattice constant and

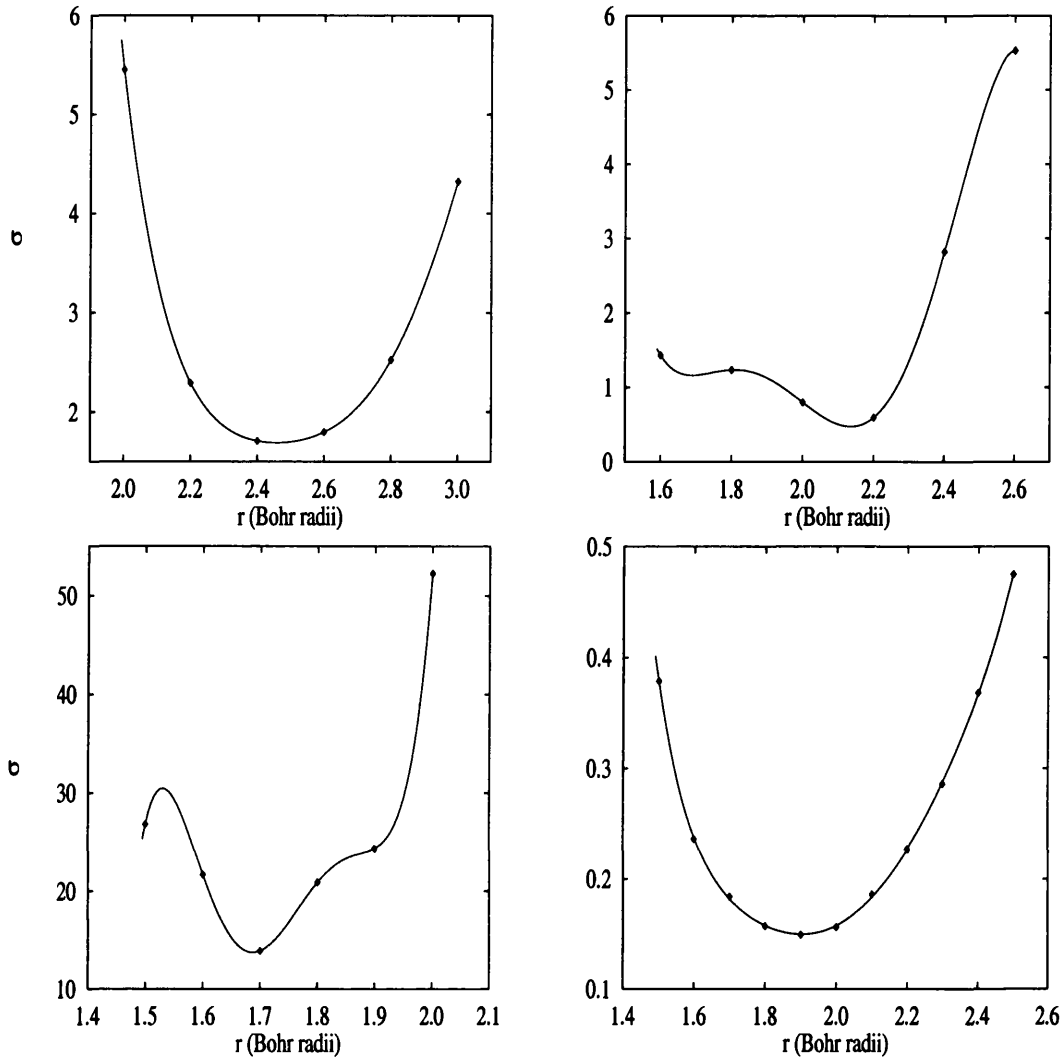


Figure 3.3: σ in $(\text{Bohr radii})^{-1}$ as a function of the core radius for $s_{1/2}$ (upper left) and $d_{3/2}$ (upper right) pseudopotentials for Rh and $s_{1/2}$ (lower left) and $p_{1/2}$ (lower right) pseudopotentials for Xe. The solid line represents a fitted curve using a fourth degree polynomial and the calculated values are denoted by diamond symbols.

the bulk modulus were calculated. In subsection 3.4.1, we will show the results obtained that justify the d core radius given in Table 3.2.

By comparing our core radii in Table 3.2 with those reported by Bachelet *et al.* (1982), we find that our core radii are systematically larger. For s , the differences are between 0.6 Bohr radii and 0.9 Bohr radii. For p the differences are smaller (between 0.1 and 0.2 Bohr radii) while for d the difference are between 1.3 and 2.5

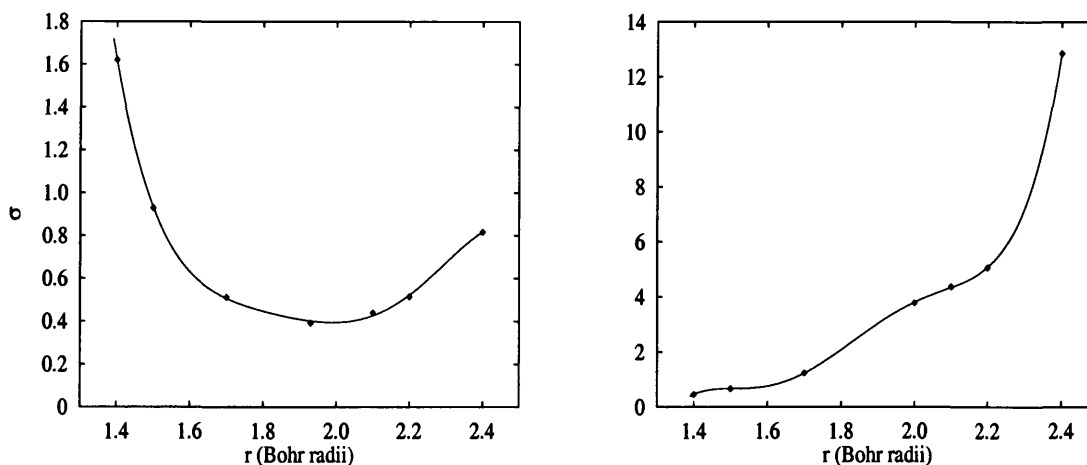


Figure 3.4: σ in $(\text{Bohr radii})^{-1}$ as a function of the core radius for the $s_{1/2}$ (left panel) and $d_{3/2}$ (right panel) pseudopotential of Cu. Solid line represents the fitted curve using a fourth degree polynomial and the calculated values are denoted by diamond symbols.

Bohr radii. In this last case the largest difference corresponds to Xe while for the transition metals the difference with respect to the Bachelet-Hamann-Schlüter core radii is, on average, 1.4 Bohr radii.

In the case of Ne a similar procedure was adopted, the core radius for $2s$ was obtained with the relation (3.1) while the remaining components were fixed in accordance with the bond length and binding energy. In the case of He, it was not possible to fix any pseudopotential components with equation (3.1). Therefore all its components were chosen from those values which provided the best agreement with similar all-electron results, see subsection 3.4.6.

3.2.3 Semi-relativistic pseudopotentials

Relativistic effects on the valence electrons are important for heavier elements. Normally these are incorporated in pseudopotentials by the scalar-relativistic approximation given by Kleinman (1980). Within Kleinman's scheme, the ionic pseu-

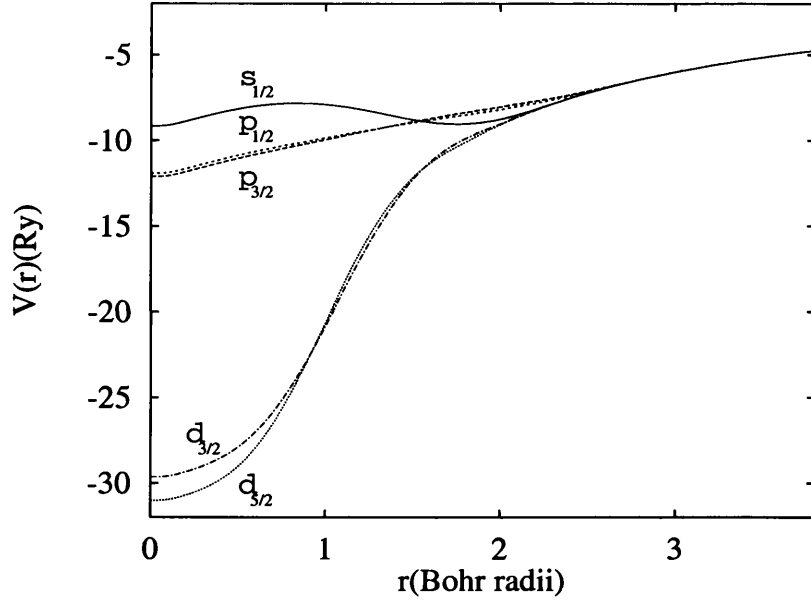


Figure 3.5: Relativistic ionic pseudopotential for Rh.

dopotential is given by (Bachelet & Schlüter, 1982)

$$V^{ion}(r) = \sum_l |l\rangle \left[\bar{V}_l^{ion}(r) + V_l^{so}(r) \mathbf{L} \cdot \mathbf{S} \right] \langle l|, \quad (3.3)$$

where $\bar{V}_l^{ion}(r)$ is defined by the average pseudopotential, weighted by the different degeneracy of $l \pm \frac{1}{2}$

$$\bar{V}_l^{ion}(r) = \frac{1}{2l+1} \left[l V_{l-\frac{1}{2}}^{ion}(r) + (l+1) V_{l+\frac{1}{2}}^{ion}(r) \right], \quad (3.4)$$

and $V_l^{so}(r)$ is given by

$$V_l^{so}(r) = \frac{1}{2l+1} \left[V_{l+\frac{1}{2}}^{ion}(r) - V_{l-\frac{1}{2}}^{ion}(r) \right]. \quad (3.5)$$

The pseudopotential calculated using equation (3.4) contains the whole scalar part of a relativistic potential and can be used for self-consistently solving the Schrödinger equation within a semi-relativistic framework. For Cu, Rh, Pt, and Xe semi-relativistic pseudopotentials were constructed from relativistic results. Figure 3.5 shows the relativistic pseudopotentials in the case of Rh, where the difference be-

tween the spin-split p and d states can be clearly seen. Having obtained the relativistic pseudopotentials with the Dirac equation, the averaged pseudopotential was calculated with equation (3.4) and the spin dependent part was not used. Finally, the non-relativistic Kohn-Sham equation was solved self-consistently in order to calculate the new wave function and from this the averaged pseudopotential was obtained.

3.2.4 Testing the Kleinman-Bylander form

As indicated in subsection 2.3.4, Kleinman & Bylander (1982) have pointed out that the computational load can be significantly reduced if the non-locality of the pseudopotential is expressed with equation (2.17) or equation (2.19) when using a plane wave basis set. Sometimes, however, the transformation of the pseudopotential into such a form creates problems, especially the appearance of wrong states, which are known as “ghost states”. In principle, there is no standard procedure to predict the presence of such states, although Gonze *et al.* (1990, 1991) have suggested that the problem can be overcome by adopting certain rules, such as the correct choice of the local pseudopotential or by increasing the core radius of the local component.

We have tested the transferability of pseudopotentials within the Kleinman-Bylander form for the semi-relativistic and non-relativistic pseudopotentials studied. Fuchs & Scheffler (1999) have pointed out that a ghost-free Kleinman-Bylander pseudopotential can be obtained with d as the local component except for “two shell” situations of transition metal elements where the s component is used commonly as the local potential. We have adopted Fuchs & Scheffler’s rule for the transition elements studied. Figure 3.6 shows a comparison between the average pseudopotential and the transformed one for the case of Rh using s as the local

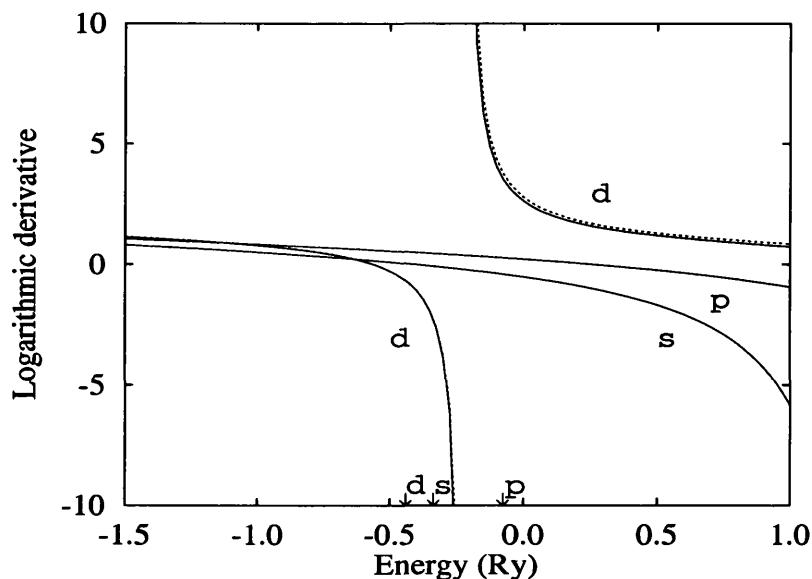


Figure 3.6: Comparison of the logarithmic derivatives in (Bohr radii) $^{-1}$ of Rh between the average pseudopotential (solid line) and the Kleinman-Bylander form (dashed line). Arrows indicate the position of the eigenvalues.

component. The comparison between the curves shows an excellent agreement, which is an indication of the high transferability of the pseudopotentials in the Kleinman-Bylander form and of the absence of “ghost states”.

In the case of rare-gas atoms the s component was also used as the local part. Tests were carried out with d as the local component but no significant differences were found. In summary, for all the pseudopotentials transformed into the Kleinman-Bylander form used in the present work, the s component was used as the local component.

3.3 Exchange-correlation energy

Ortiz & Ballone (1991) have reported that the inclusion of gradient corrections introduces oscillations in the exchange-correlation potential making the pseudopotentials present wiggles. We have found such oscillations and strong irregularities

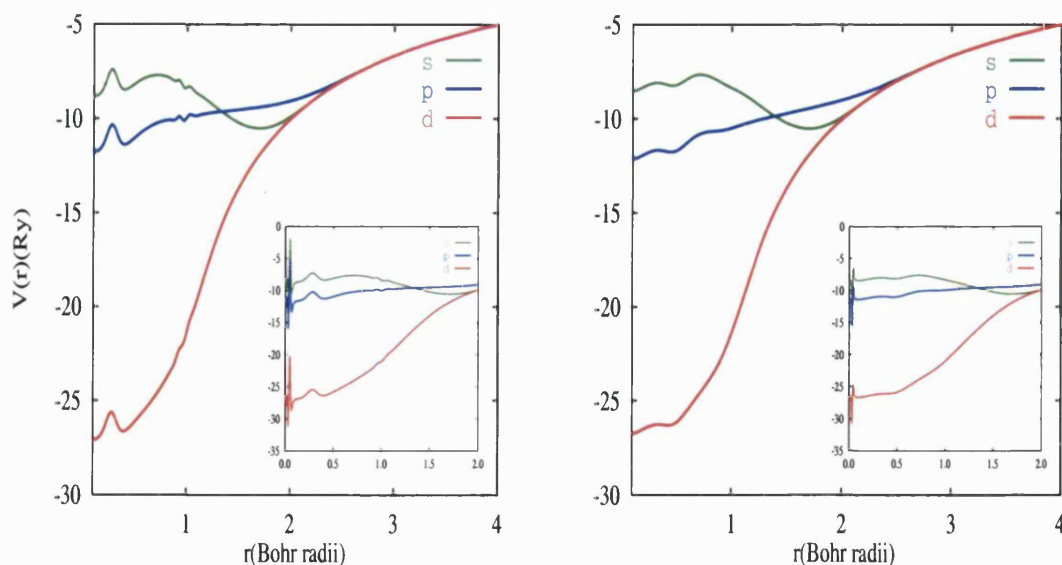


Figure 3.7: The average ionic pseudopotentials in real space for Pt using the GGA approximation. Left corresponds to GGA-PW91 results and right to GGA-PBE. In both cases, the strongest oscillations close to the nucleus (small panel) were removed.

inside the core radius in all pseudopotentials constructed with the non-local approximations (GGA-PW91 and GGA-PBE). These oscillations were less strong in the case of GGA-PBE than GGA-PW91, Figure 3.7. The mathematical representation of GGA-PBE (see Appendix A) not only makes the evaluation of the exchange-correlation energy simple but also improves the quality of the pseudopotentials by reducing wiggles and strong oscillations at the origin. However, we have found that these peaks do not lead to a significant change in the total energy or structural properties such as the lattice constant and bulk modulus, at least in the case of Pt, see subsection 3.4.4. For this reason we have removed only the strongest oscillations close to the nucleus. In the case of Pt, these oscillations were located for values less than 0.1 Bohr radii (see Figure 3.8). The peaks were removed by flattening the pseudopotential curves around each oscillation with a linear interpolation.

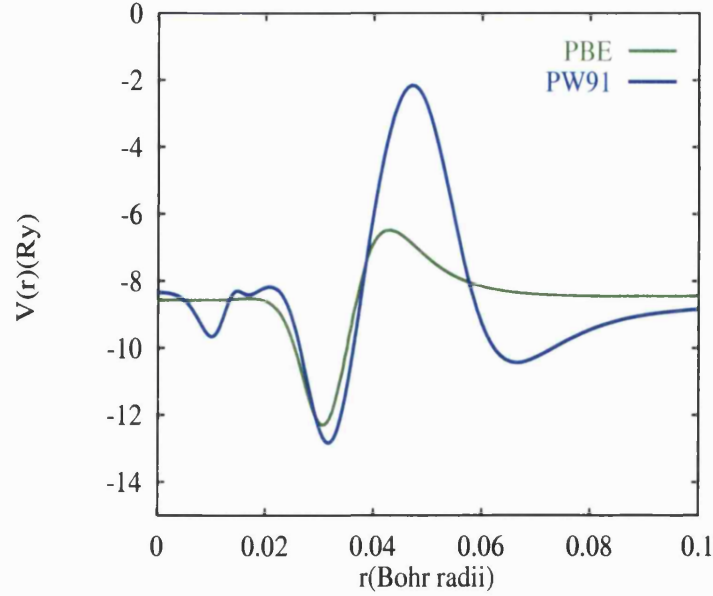


Figure 3.8: s pseudopotential in real space for Pt close to the nucleus using GGA-PBE and GGA-PW91.

3.3.1 Core-valence exchange-correlation correction

The short-ranged oscillations present in the ionic pseudopotentials constructed with GGA-PW91 and GGA-PBE were removed when the core-valence exchange-correlation correction was included in the pseudopotential construction procedure (see Figure 3.9).

The oscillations caused by the gradient expansion are connected with the large contribution of the gradient at low density in the valence region. The inclusion of core states increases the density in this region which stabilises the exchange-correlation potential (Ortiz & Ballone, 1991). We have included just a partial pseudo core charge density (see subsection 2.3.5). The inclusion of the partial core charge introduces an additional term in the atomic total energy, which becomes

$$E \rightarrow T_s[\rho^{val}] + \int_0^\infty (\rho^{val} + \tilde{\rho}_{partial}^{core}) V_{ext} dr^3 + E_H[\rho^{val}] + E_{xc}[(\rho^{val} + \tilde{\rho}_{partial}^{core})]. \quad (3.6)$$

For a total energy calculation in a crystal a representation of the partial core charge

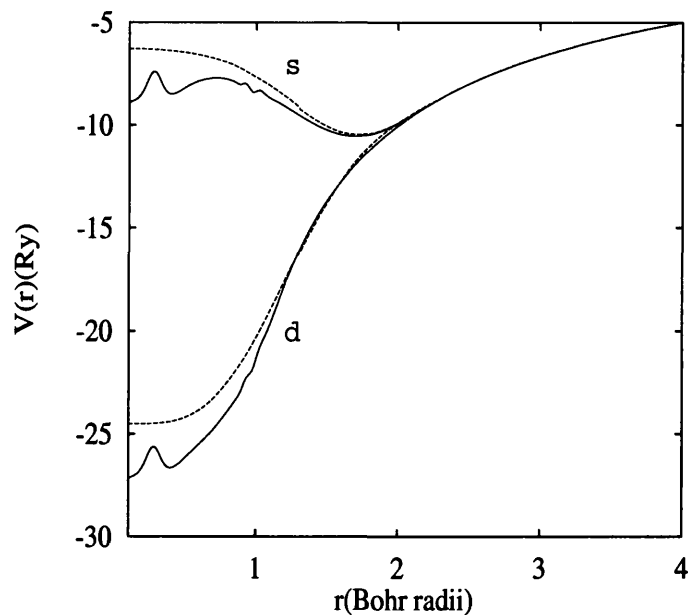


Figure 3.9: s and d components of the ionic pseudopotential for Pt without (solid line) and with (dashed line) the non-linear core-valence exchange-correlation correction. The exchange-correlation energy was calculated with the GGA-PW91 approximation.

density in the \mathbf{G} space is needed. This was determined by

$$\rho^{core}(\mathbf{G}) = \frac{4\pi}{\Omega} \int_0^{\infty} r^2 j_0(|\mathbf{G}|r) \tilde{\rho}^{core}(r) dr, \quad (3.7)$$

where Ω is the cell volume and j_0 is the spherical Bessel function of order zero (Arfken & Weber, 1995).

3.4 Testing pseudopotentials

Pseudopotentials for He, Ne, Cu, Rh, Pt, and Xe were tested by calculating equilibrium structural properties. Tests on Cu, Rh, and Pt pseudopotentials were made with the plane-wave method while the mixed-basis method was used for He, Ne, Rh, Pt, and Xe. The application of both schemes for Pt and Rh allows us to compare the calculated structural properties. All the calculations were carried out

consistently, in other words, the same approximation for the exchange-correlation energy was used for both the pseudopotential construction and in the total energy calculations. The Brillouin zone for the bulk metallic systems was sampled with a $8 \times 8 \times 8$ Monkhorst & Pack mesh (leading to 28 \mathbf{k} -points in the irreducible wedge) while one \mathbf{k} -point was used for dimer calculations. For the metallic systems, the Fermi surface was broadened with a smearing of 0.25 eV and the total energy was extrapolated to zero temperature (Gillan, 1989; de Vita & Gillan, 1991). Self consistent iterations were carried out until the total energy was stable to 10^{-5} eV.

For fcc Cu, Rh, and Pt the total energy was calculated at eight different lattice constants around their equilibrium value and these results were fitted to Murnaghan's equation of state (Murnaghan, 1944; Anderson, 1966; Fu & Ho, 1983):

$$E(V) = E(V_0) + \frac{B_0 V}{B'_0} \left\{ \left(\frac{V_0}{V} \right)^{B'_0} + 1 \right\} - \frac{B_0 V_0}{B'_0 - 1}, \quad (3.8)$$

where V is the cell volume, and B_0 and B'_0 are the bulk modulus and its pressure derivative at the equilibrium volume V_0 .

The interaction potential energies for He_2 , Ne_2 , and Xe_2 dimers were obtained by calculating the total energy difference between the dimer at different bond lengths (approximately 16 points) and its isolated atom, keeping in both cases the size of the box, number of \mathbf{k} -points and cut-off energies constant. For He and Ne the molecule was put into a rectangular box of size $8 \text{ \AA} \times 8 \text{ \AA} \times 13 \text{ \AA}$ and for Xe, a box of $9 \text{ \AA} \times 9 \text{ \AA} \times 15 \text{ \AA}$ was used. We have found that boxes of this size are large enough to avoid any interaction with neighbouring molecules.

3.4.1 Core radius for Cu

In subsection 3.2.2, it was shown that it is not possible to obtain a minimal point in equation (3.1) for Cu d components. In order to find d core radii for Cu which allow us to reproduce structural properties which agree with the all-electron or experimental results, we have varied the d core radius, while the s and p components were kept at the optimised values calculated with equation (3.1). The values of the d core radius were chosen taking into account the position of the maximum of the $3d$ orbital. Table 3.3 shows the calculated lattice constant and bulk modulus for Cu as a function of the d core radius and the plane wave cut-off energy.

From the results shown in Table 3.3, we can see that there is no significant change in the lattice constant for all the chosen core radii; most converge to a value of 3.55 Å, a result which agrees well with the value of 3.52 Å obtained by Khein *et al.* (1995) using all-electron calculations and the local density approximation. In the case of the bulk modulus, the variation was less than 5 GPa, although with a value of 1.6 Bohr radii it is not clear if convergence is reached by 1300 eV or if a higher cut-off energy is required. However, with a core radius between 2.0 Bohr

E_{cut} (eV)	Lattice constant (Å)					Bulk modulus (GPa)				
	Core radius (Bohr radii)					Core radius (Bohr radii)				
	1.6	1.8	2.0	2.2	2.4	1.6	1.8	2.0	2.2	2.4
500	3.423	3.463	3.490	3.516	3.541	139	730	422	277	213
600	3.501	3.447	3.500	3.530	3.548	205	281	250	209	189
700	3.527	3.552	3.554	3.553	3.556	210	176	175	178	180
800	3.489	3.523	3.542	3.549	3.554	314	221	187	181	180
900	3.517	3.543	3.547	3.550	3.554	179	173	177	179	180
1000	3.517	3.539	3.546	3.550	3.554	209	181	178	179	180
1100	3.542	3.544	3.547	3.550	3.554	179	178	178	179	180
1200	3.546	3.546	3.547	3.550	3.554	176	177	178	179	180
1300	3.547	3.546	3.547	3.550	3.554	171	176	178	179	180

Table 3.3: Calculated lattice constant and bulk modulus for Cu using the local density approximation as a function of the plane wave cut-off energy and the d core radius.

radii and 2.4 Bohr radii the pseudopotentials require a much lower cut-off energy and provide a calculated lattice constant and bulk modulus in good agreement with previously reported results. In principle, we could use any value of the core radius inside the given interval. Our final selection for the Cu d core radius was 2.2 Bohr radii.

3.4.2 Pseudopotential-plane-wave results

When performing a total energy calculation based on a plane wave basis set, the physical properties depend on the cut-off energy used. In order to test the convergence of the lattice constant and the bulk modulus with respect to the plane wave basis set, the cut-off energy was varied over a wide range taking into account what kind of transition metal was under consideration. For instance, $3d$ transition metals present deeper d pseudopotentials because they contain no d electrons in their cores, therefore a calculation with a plane wave basis requires of a larger cut-off energy to reach convergence than the $4d$ and $5d$ series, Similarly, the pseudopotentials for $5d$ transition metals are softer than for the $4d$.

Table 3.4 shows the results calculated for the lattice constant and bulk modulus for Cu, Rh, and Pt as a function of the plane wave cut-off energy with both the local and non-local approximations used for the exchange-correlation energy. In general the convergence of the lattice constant and bulk modulus was satisfactory for all the elements considered. With the GGA approximation, the plane wave cut-off energy required for convergence was similar to that for the LDA. For all elements, we notice that the simplified GGA-PBE provides similar results to PW91, which confirms the equivalence of the approximations.

Table 3.5 summarises the results of Table 3.4, using plane wave cut-off energies of

	E_{cut} (eV)	Lattice constant (\AA)			Bulk modulus (GPa)		
		LDA	PW91	PBE	LDA	PW91	PBE
Cu	700	3.553	3.719	3.713	178	167	166
	800	3.549	3.659	3.650	181	131	141
	900	3.550	3.657	3.665	179	135	139
	1000	3.550	3.659	3.666	179	135	139
	1100	3.550	3.660	3.666	179	136	140
	1200	3.550	3.660	3.666	179	136	140
Rh	400	3.860	3.931	3.926	390	391	391
	450	3.764	3.862	3.856	379	271	278
	500	3.781	3.901	3.894	285	208	214
	550	3.802	3.912	3.901	287	234	236
	600	3.802	3.908	3.902	296	243	244
	650	3.798	3.906	3.901	297	241	243
	700	3.798	3.906	3.901	297	241	243
Pt	400	3.934	4.022	4.018	299	272	268
	450	3.917	4.015	4.012	290	240	236
	500	3.924	4.021	4.018	287	237	235
	550	3.925	4.022	4.019	287	241	236
	600	3.925	4.022	4.019	287	241	236

Table 3.4: Calculated lattice constant and bulk modulus for Cu, Rh, and Pt using the local density approximation, and the gradient generalised approximations (GGA-PW91 and GGA-PBE) as a function of the plane wave cut-off energy.

900 eV (Cu), 600 eV (Rh), and 500 eV (Pt). Also a comparison with experiment and the results of previous calculations for Cu, Rh, and Pt are shown. The agreement with previous all-electron calculations and full potential calculations is very good. In the case of Cu, comparison with experiment shows that the equilibrium lattice constant is underestimated by 1.7 % with LDA whereas PW91 and PBE overestimate it by 1.4 % and 1.6 % respectively. The bulk modulus is underestimated by PW91 while PBE gives results only slightly above experimental values. GGA results are closer to the experimental value than LDA. The error in the bulk modulus is reduced from 28.3 % to 2.2 % by PW91 and 0.7 % by PBE. Comparing our Cu results with those obtained by Troullier & Martins (1991), we found that our lattice constant differed by only 0.02 \AA , which could be due to the slightly different core radii used in the pseudopotential construction by Troullier & Martins, ($s = 2.08$ Bohr radii, $p = 2.30$ Bohr radii and $d = 2.08$ Bohr radii).

	Lattice constant (Å)				Bulk modulus (GPa)			
	LDA	PW91	PBE	Expt.	LDA	PW91	PBE	Expt.
Cu	3.55	3.66	3.67	3.61 ^f	177	135	139	142 ^g
	(-1.7)	(+1.3)	(+1.5)	-	(+28.3)	(-2.2)	(+0.7)	
PP-PW ^a	3.57	-	-		174	-	-	
PP-MB ^b	3.62	-	-		150	-	-	
AE ^c	3.52	3.62	-		192	151	-	
Rh	3.80	3.91	3.90	3.81 ^e	296	243	244	267 ^e
	(-0.3)	(+2.5)	(+2.4)		(+10.9)	(-9.7)	(-9.0)	
AE ^d	3.74	-	-		346	-	-	
US ^d	3.75	-	-		344	-	-	
FP ^e	3.76	3.84	-		313	257	-	
Pt	3.92	4.02	4.02	3.92 ^e	287	237	235	283 ^e
	(+0.1)	(+2.6)	(+2.5)		(+1.4)	(-16.2)	(-15.2)	
AE ^c	3.90	3.97	-		307	246	-	
FP ^e	3.89	3.97	-		306	263	-	

^a Pseudopotential-plane wave, PP-PW, from Troullier & Martins (1991).

^b Pseudopotential-mixed basis, PP-MB, from Morrison *et al.* (1989).

^c From Khein *et al.* (1995).

^d Ultra soft pseudopotential, US, from Stokbro (1996).

^e Full potential linear muffin tin orbitals, FP LMTO, from Ozoliņš & Körling (1993).

^f From Lide & Frederikse (1997).

^g From van't Klooster *et al.* (1979).

Table 3.5: Calculated lattice constant and bulk modulus for Cu, Rh, and Pt the with local density approximation and the gradient generalised approximations (GGA-PW91 and GGA-PBE). Numbers in parentheses indicate the percentage error relative to experiment.

The reverse was found in the cases of Rh and Pt, where the lattice constant calculated by LDA was in closer agreement with experiment than for GGA schemes. In the case of Rh, the lattice constant calculated with LDA differs from experiment by only -0.3% whereas PW91 and PBE over-corrected it to $+2.4\%$ and $+2.5\%$ respectively. Although our LDA calculated lattice constant was slightly larger than those reported in other theoretical calculations (Ozoliņš & Körling, 1993; Stokbro, 1996) ours is closer to the experimental result. With respect to the bulk modulus, we found a slight improvement with GGA, but a worse estimation of the lattice constant. For Pt, the LDA results are in good agreement with the experiment. Similar results have been reported by Ozoliņš & Körling (1993) using the

full potential linear muffin tin orbital method, these authors have concluded that the GGA does not improve the structural properties of the $5d$ transition metals. Although the structural properties (lattices constant or bond length) can be worse with the GGA than the LDA, in general the binding energy is significant improved with the GGA (Perdew *et al.*, 1992; Fuchs *et al.*, 1998).

3.4.3 Testing core-radii

For transition metals, the convergence of total energy calculations is determined by the d pseudopotential component. In order to test how the transferability and the plane wave cut-off energy are affected by the depth of the d pseudopotential, the bulk modulus and the lattice constant for Pt were calculated at different d core radii. The core radii for s and p potentials were kept constant and were taken from the values given in Table 3.2. Figure 3.10 shows the d pseudopotential for Pt at different core radii, which were chosen to ensure an appreciable difference of depth between two consecutive curves. The presence of wiggles in a curve (green line) is due to too small a radius being chosen. Table 3.6 shows the results obtained for the lattice constant and bulk modulus of Pt as a function of the core radius. All calculations were performed using the LDA to approximate the exchange-correlation energy.

Despite the wide range used for the d core radius, the lattice constant showed only a slight variation with respect to the results of the optimised core radius (see section 3.2.2). It is clear that the plane wave cut-off energy required to reach a convergent solution decreases as the core radius is increased but with a evident loss of transferability. The changes in the calculated bulk modulus were more sensitive as a consequence of its dependence on the second derivative of the energy. A better agreement was obtained for the bulk modulus as the core decreased, when compa-

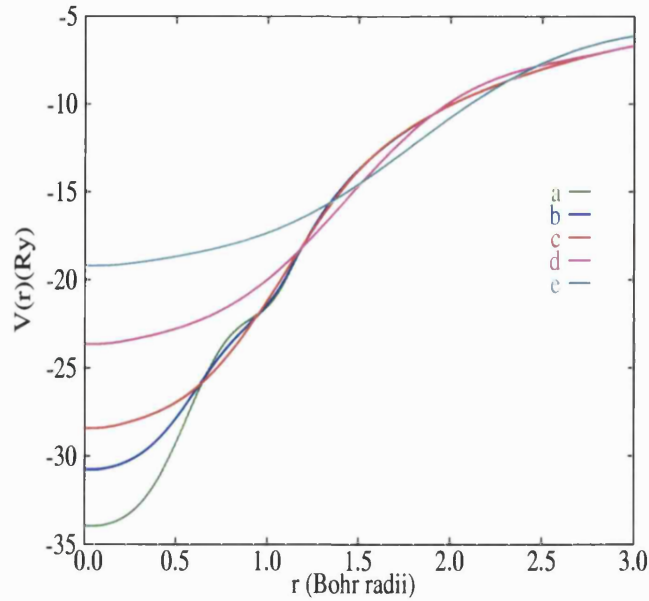


Figure 3.10: d pseudopotential for Pt at a selected set of core radii. (a) $r_c = 1.17$, (b) $r_c = 1.20$, (c) $r_c = 2.00$, (d) $r_c = 3.00$ and (e) $r_c = 4.00$. Units are Bohr radii.

	r_c (Bohr radii)	400 eV	450 eV	500 eV	550 eV	600 eV
a (Å)	1.17	3.944 (1.1)	3.928 (0.7)	3.935 (0.9)	3.936 (0.6)	3.936 (0.3)
	1.20	3.934 (0.8)	3.912 (0.3)	3.923 (0.6)	3.924 (0.6)	3.923 (0.6)
	2.00	3.934 (0.8)	3.912 (0.3)	3.923 (0.6)	3.924 (0.6)	3.924 (0.6)
	3.00	3.934 (0.8)	3.933 (0.8)	3.933 (0.8)	3.933 (0.8)	3.933 (0.8)
	4.00	4.017 (3.0)	4.017 (3.0)	4.017 (3.0)	4.017 (3.0)	4.017 (2.3)
B (GPa)	1.17	318 (3.9)	297 (2.3)	287 (6.2)	290 (5.2)	291 (4.9)
	1.20	311 (1.6)	294 (3.4)	285 (6.8)	287 (6.2)	287 (6.2)
	2.00	311 (1.6)	284 (7.2)	286 (6.5)	287 (6.2)	287 (6.2)
	3.00	286 (6.5)	286 (6.5)	286 (6.5)	286 (6.5)	286 (6.5)
	4.00	281 (8.2)	282 (7.8)	282 (7.8)	282 (7.8)	282 (7.8)

Table 3.6: Calculated lattice constant, a , and bulk modulus, B , for Pt as a function of the core radius, r_c , and the cut-off energy. Numbers in parentheses indicate percentage relative error with respect to all-electron results (Klein *et al.*, 1995).

red with all-electron results, but at the expense of a worse estimation of the lattice constant. In summary, it seems that the core radius optimised with equation (3.1) provides the best estimate for both structural properties for Pt.

3.4.4 GGA pseudopotentials

As was pointed out in section 3.3, it is not expected that the strong oscillations produced by the generalised gradient approximation close to the nucleus cause a substantial change in the calculated bulk properties. We have calculated the lattice constant and the bulk modulus for fcc Pt for a fully GGA-PW91 pseudopotential. In the first case, the oscillations near to the nucleus were kept and in the second case they were removed (see section 3.3). Table 3.7 shows the total energy as a function of the lattice constant. The change of the total energy was about 0.01 eV, so the change the lattice constant and bulk modulus will be small. Indeed, the differences in the lattice constant and the bulk modulus were only 0.003 Å and 0.2 GPa respectively.

Lattice constant (Å)	E_{total} (eV)	E_{total} (eV)
3.6	-709.2073	-709.2043
3.7	-710.1694	-710.1720
3.8	-710.7648	-710.7651
3.9	-711.0835	-711.0786
4.0	-711.1896	-711.1872
4.1	-711.1603	-711.1488
4.2	-711.0163	-711.0058
4.3	-710.8009	-710.7897

Table 3.7: Total energy, E_{total} , as a function of the lattice constant for Pt using the GGA-PW91 approximation and a plane wave cut-off energy of 550 eV. The first column corresponds to a pseudopotential with oscillations at the origin while the second one corresponds to a pseudopotential with oscillations removed (see section 3.3). In the first case, the calculated lattice constant and the bulk modulus were 4.026 Å and 237.0 GPa respectively whereas in the second, they were 4.023 Å and 237.2 GPa.

3.4.5 Pseudopotential-mixed-basis results

In contrast to the plane wave method, the accuracy of calculations based on the mixed basis method on two cut-off energies, (see equation (2.37)). The first term

$E_{cut_{pw}}$ (eV)	Lattice constant (Å)	Bulk modulus (GPa)
40	3.814	301
50	3.801	299
60	3.801	298
70	3.804	298
80	3.804	298

Table 3.8: Calculated lattice constant and bulk modulus for Rh as a function of the plane wave cut-off energy.

corresponds to the expansion of the atomic orbitals in terms of plane waves and the second one corresponds to the delocalised part of the wave function. It is important to establish how the low-energy plane wave component could affect the structural properties in a transition metal. We have tested the structural properties of Rh as a function of the cut-off energy for the delocalised part. The localised part of the wave function, equation (2.37), was expanded using the same cut-off energy as in its equivalent full plane wave calculation and the additional plane wave cut-off was varied between 40 eV and 80 eV. The remaining parameters (k -points, smearing, etc.) were kept equal to those used in section 3.4. Table 3.8 shows the lattice constant and the bulk modulus for fcc Rh as a function of the cut-off energy. We find that the structural parameters converge rapidly for a cut-off above 50 eV. Similar results were found in the case of Pt and the rare-gas elements studied. We have repeated calculations of the structural properties for Rh and Pt using the same cut-off energy for the orbital expansion as in the equivalent full plane wave calculations and with the additional plane wave cut-off fixed at 60 eV. Table 3.9 shows the calculated lattice constant and bulk modulus obtained with the pseudopotential-mixed-basis method. For both elements the lattice constant was very similar to those obtained with the plane wave method, with a maximum difference of only 0.01 Å (see Table 3.5). A very slight difference was observed in the bulk modulus, but this was always less than 0.1 %. From these results, we conclude the mixed-basis set allows the calculation of physical properties with the same accuracy as the plane wave basis set but with a significantly lower computational load. For these tests,

		LDA	LDA-CC	PBE	PBE-CC	Expt
Pt	Lattice constant (Å)	3.93	3.92	4.02	4.02	3.92 ^a
	Bulk modulus (GPa)	285	283	243	235	283 ^a
Rh	Lattice constant (Å)	3.80	3.81	3.90	3.90	3.81 ^a
	Bulk modulus (GPa)	298	294	241	236	267 ^a
Xe ₂	Bond length (Å)	4.05	3.99	4.65	4.74	4.3 ^b
	Binding energy (meV)	43.6	43.7	7.8	8.9	23.4 ^b

^a From Ozoliņš & Körling (1993).

^b From Barker *et al.* (1974).

Table 3.9: Calculated lattice constant and bulk modulus for Pt and Rh and calculated bond length and binding energy for the Xe dimer using a pseudopotential-mixed basis approach. CC denotes results for which non-linear core corrections are included.

the mixed basis method provides results about four times faster than the plane wave method. The effect of the non-linear exchange-correlation core correction on some elements was studied using the mixed basis method. Results are given in Table 3.9. With both the LDA and GGA-PBE approximations we find that core corrections produce only a small effect on the lattice constant. The effect on the bulk modulus is larger, with the GGA producing an increased underestimation with respect to the experimental value.

Table 3.9 also shows the bond length and binding energy for the Xe₂ dimer, calculated by placing Xe₂ in a rectangular box of size $9 \text{ \AA} \times 9 \text{ \AA} \times 15 \text{ \AA}$ and varying the distance between Xe atoms from 3 \AA to 6 \AA . The cut-off energies were fixed at 500 eV and 60 eV for the expansion of the localised and delocalised wave function parts respectively, and the Brillouin zone was sampled with $1 \times 1 \times 1$ Monkhorst & Pack mesh.

It can be seen in Figure 3.11 that the LDA and GGA functionals predict interaction potentials that are remarkably different. The LDA predicts a significantly more attractive interaction between the Xe atoms than the GGA. Table 3.9 shows that the binding energy is overestimated with the LDA while the GGA predicts too low a value. Similar behaviour with the GGA have been reported by Pérez *et al.*

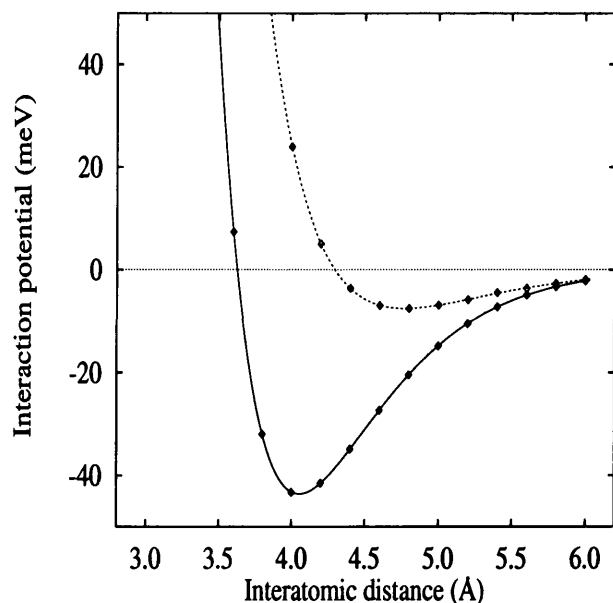


Figure 3.11: Interaction potential energy for Xe_2 calculated with the LDA (solid line) and GGA-PBE (dashed line) approximations. Diamond symbols represent the calculated points.

(1994), who found the interaction potential to be quite flat around the equilibrium position of the Xe_2 dimer. In general, neither the LDA nor GGA-PBE provides a good description of the interaction.

3.4.6 He and Ne core radii

The optimisation scheme used for obtaining core radii in Pt, Rh, and the Xe atom was not completely successful for Ne and He. For Ne, the procedure used for Cu was followed, the core radius for the $2s$ pseudopotential was calculated using equation (3.1) and the core radius for $2p$ was determined by exploring the variation of the structural parameters (bond length and binding energy) of the Ne_2 dimer for different core radii.

Table 3.10 shows the binding energy for the Ne_2 dimer as a function of the $2p$ core radius, which was varied from 2.2 Bohr radii to 1.7 Bohr radii. We find that the

E_{cut} (eV)	Core radius (Bohr radii)					
	2.2	2.1	2.0	1.9	1.8	1.7
600	-7.5	-8.2	-8.2	-4.6	-5.3	-7.2
700	-8.0	-8.5	-5.2	-4.0	-3.8	-6.4
800	-8.6	-7.8	-5.5	-3.5	-3.9	-5.4
900	-8.5	-7.4	-5.6	-3.7	-4.2	-5.3
1000	-8.6	-7.7	-5.6	-3.6	-4.0	-5.3
1100	-8.6	-7.8	-5.7	-3.7	-4.1	-5.4
1200	-8.6	-7.8	-5.7	-3.6	-4.2	-5.4

Table 3.10: Calculated binding energy (meV) for Ne_2 as a function of the p core radius using the mixed basis method. Exchange-correlation effects were approximated with the GGA-PBE.

E_{cut} (eV)	Core radius (Bohr radii)				
	1.00	1.25	1.50	1.75	2.00
600	-3.7	-3.4	-3.2	-3.2	-3.4
700	-4.0	-4.2	-3.4	-3.4	-3.2
800	-3.7	-3.3	-3.3	-3.5	-3.2
900	-3.6	-3.2	-3.2	-3.2	-3.2
1000	-3.1	-3.2	-3.2	-3.2	-3.1
1100	-3.2	-3.2	-3.2	-3.2	-3.1
1200	-3.2	-3.2	-3.2	-3.2	-3.1

Table 3.11: Calculated binding energy (meV) for He_2 as a function of the s core radius using the mixed basis method. Exchange-correlation effects were approximated with the GGA-PBE.

binding energy is quite sensitive to the p core radius while the equilibrium bond length is much more stable around 3.1 Å (this value was practically constant for each p core radius used, with the greatest deviation being only 0.02 Å). We find that the binding energy calculated with a core radius of 2.0 Bohr radii agrees well with the value of 5.6 meV obtained by Patton & Pederson (1997) using all-electron calculations.

In the case of He_2 , it was more difficult to obtain optimised core radii as no component could be calculated using equation (3.1). In this case, the p and d components were chosen by taking a value close to the maximum of the $2p$ and $3d$ wave functions. The $1s$ core radius was then varied from 1.0 Bohr radii to 2.0 Bohr radii. In contrast to Ne, the calculated binding energy of He_2 was not sensitive to the value

		LDA	PBE	Expt ^a	MP2/AE ^b	AE/LDA ^c	AE/PBE ^c
He ₂	Bond length (Å)	2.40	2.80	2.96	3.08	2.40	2.76
	Binding energy (meV)	9.3	3.1	1.0	1.4	9.4	3.2
Ne ₂	Bond length (Å)	2.66	3.11	3.03	3.23	2.64	3.09
	Binding energy (meV)	18.9	5.2	3.9	5.4	19.9	5.6

^a From Gordon & Kim (1972).

^b From Burda *et al.* (1996). (MP2/AE) Møller-Plesset perturbation theory/all-electron.

^c From Patton & Pederson (1997).

Table 3.12: Calculated bond length and binding energy for He and Ne dimers using the LDA and GGA-PBE approximations.

the core radius (see Table 3.11). Only a very small variation of the binding energy was obtained over the selected range. By comparing our result with all-electron results, we find an excellent agreement with the value of 3.2 meV obtained by Patton & Pederson (1997). The *s* core radius for He was taken as 2.0 Bohr radii because this provides a softer pseudopotential.

For both atoms (He and Ne), we find that the equilibrium geometry of the dimer is better described with the GGA-PBE than the LDA, Table 3.12. An important difference in the binding energy was found between the exchange-correlation functionals. The LDA gives a large overestimation of the binding energy for both dimers. Although GGA-PBE also overestimates the binding energy, it is closer to experimental results. Our results are in excellent agreement with those of Patton & Pederson (1997) who used an all-electron DFT approach. Models based on the Hartree-Fock approximation (Burda *et al.*, 1996) show that MP2 is very accurate in describing the binding of the He dimer but provides a similar result for the Ne dimer to models based on a density functional formalism.

3.5 Conclusions

Using first principles total energy calculations and *ab initio* pseudopotentials, we have studied the equilibrium structure of the transition metals Cu, Rh, and Pt. The results showed that the lattice constant and bulk modulus are in good agreement with all-electron calculations and with other theoretical models.

In the case of light rare-gas atoms (He and Ne) the properties of their dimers were better described by the GGA, while for Xe neither LDA nor GGA gives a good description of the bonding, with both showing a large deviation from experimental results.

The results obtained with the GGA show clearly the equivalence between the PW91 and PBE functionals. Additionally, we have found that the GGA-PBE reduces substantially the oscillations produced by the GGA during the pseudopotential construction.

The optimisation of the core radius through the logarithmic derivative allows us to find a balance between the high transferability of a small cut-off radius and the lower plane wave cut-off energy of a large one. However for He, Ne, and the *d* Cu component the optimisation process was not possible for every component.

For the elements Xe, Pt, and Rh the core-valence exchange-correlation correction has a small effect on the structural properties, tending to improve the results using the LDA. Additionally, an improvement in the quality of the pseudopotential was obtained with the GGA, especially the removal of the oscillations close to the nucleus.

The results obtained with the mixed basis method are found to be equivalent to

those obtained with the plane wave method, but with a substantial reduction in the computing time required. This suggests that the mixed basis method is a useful tool in the study of more complicated systems.

Chapter 4

Interaction of Xe atoms with the Pt(111) surface

4.1 Introduction

The adsorption of rare-gas atoms is frequently discussed in terms of the Van der Waals force. Within this description the bonding is due to charge density fluctuations in the adsorbate interacting with their induced image charge inside the metal. But doubts about the general validity of the Van der Waals approximation appear when large changes in the work function upon rare-gas adsorption are observed (Flynn & Chen, 1981). This has encouraged consideration of the possibility of charge transfer mechanisms for these kind of systems. In fact, Ishi & Viswanathan (1991) reviewing experimental data from work function measurements and electron spectroscopies for Xe on metals have found that the chemical bonding contribution plays a significant role in Xe adsorption.

Many phases of adsorbed layers arise due to the competing lateral interaction

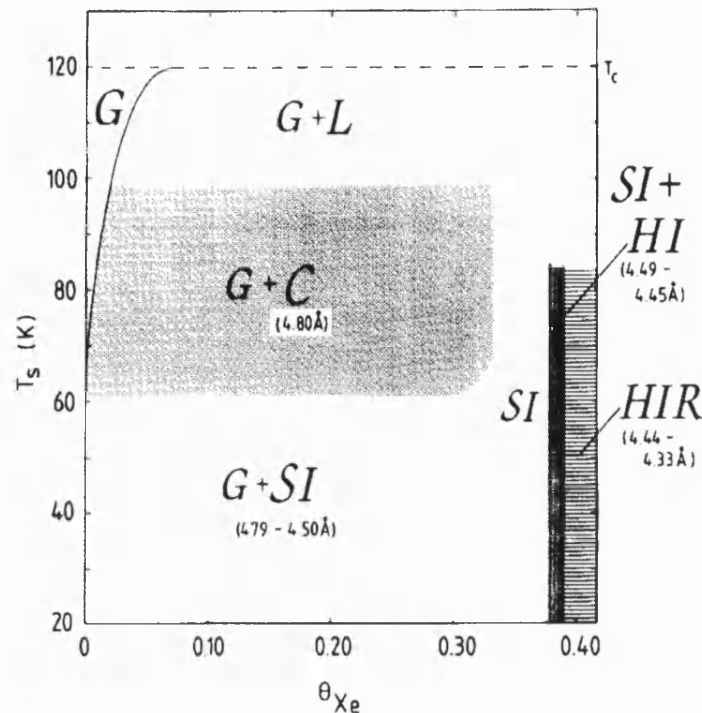


Figure 4.1: Phase diagram of Xe/Pt(111) from Kern *et al.* (1988). C, SI, HI, and HIR denote the commensurate ($\sqrt{3} \times \sqrt{3}$)R30°, the striped incommensurate, the hexagonal incommensurate and the hexagonal incommensurate rotated phase. G and L denote the two-dimensional gas and liquid phases respectively. T_c is the critical temperature, T_s is the substrate temperature and θ_{Xe} is the coverage of Xe.

between adatoms and the adsorbate-substrate interaction (Bruch *et al.*, 1997). Experimentally, it has been found that the two-dimensional adsorbed layers can exist in several phases, some of which have a counterpart in three-dimensional systems but some of which do not. In the particular case of Xe adsorption on Pt(111) at least six phases have been observed (Figure 4.1). At low coverage, a transition from gas to solid occurs. At temperatures between 62 K and 99 K and a coverage less than 0.33 monolayers (ML), a commensurate ($\sqrt{3} \times \sqrt{3}$)R30° phase exists. At $\theta_{Xe} = 0.33$ ML, or by cooling below 62 K, the commensurate phase suffers a transition into a striped incommensurate phase, where the Xe adlayer is uniaxially compressed along the ΓM_{Xe} direction. For $\theta_{Xe} > 0.38$ ML, the striped incommensurate phase is transformed into a hexagonal incommensurate phase. The hexagonal incommensurate phase shows a continuous transition from R30° to

a rotated $R30^\circ \pm 3.3^\circ$ orientation when the coverage is increased to 0.39 ML. It is surprising that the smooth Pt(111) surface seems to be one where a diversity of monolayer phases of Xe has been observed. In fact, the Xe/Pt system has the outstanding property of providing a demonstration of commensurate-incommensurate phase transitions in two dimensions (Kern *et al.*, 1988).

The preferential adsorption site for Xe has been subject of more controversy. On the basis of diffraction from the uniaxial incommensurate phase, Gottlieb (1990) found the top site to be the most stable. This was supported by Müller's LDA cluster calculation (Müller, 1990). However, Müller's result can be questioned due to the fact that he used two Xe atoms adsorbed on a 25 atom Pt cluster, which raise the question of whether such a configuration is sufficient to describe the full surface interaction. Barker & Rettner (1992) found in construction of their empirical potential that a consistent fit with a wide range of dynamical and equilibrium data could be obtained only by placing the Xe atom at the top site. However, this assignment was challenged by Zeppenfeld *et al.* (1992), and a later spin polarised LEED experiment indicated a hollow-site adsorption (Potthoff *et al.*, 1995) (although the determined adsorption height of 4.2 Å appears to be unphysically large). More recently the pendulum has swung back towards the top site, with Bruch *et al.* (1998) showing that this is consistent with their high-resolution He-atom scattering data, and a new LEED study favouring top-site adsorption with an adsorption height of 3.4 Å (Seyller *et al.*, 1999). Although top-site adsorption might at first sight seem unlikely, there is experimental evidence that this is indeed the case for several Xe-metal system (Seyller *et al.*, 1999; Narloch & Menzel, 1998, and reference therein).

There is also a considerable discrepancy between different estimations of the diffusion barrier. Barker & Rettner (1992) reported a value of 24 meV, which is closed to the experimental estimates of 30 meV given by Kern *et al.* (1988) and 31 meV

given by Horch *et al.* (1995). However, a more recent experimental determination using quasielastic helium-atom scattering at low Xe coverage puts an upper limit on the diffusion barrier of 9.6 meV (Ellis *et al.*, 1999), indicating that there remains some uncertainty regarding this quantity.

In this chapter, the interaction energy between Xe and Pt(111) is analysed with total-energy calculations based on a mixed-basis approach within density functional theory and using a pseudopotential formalism (Chapter 2). The slab approximation is used to represent the static adsorption between the Xe atom and the Pt surface. The substrate is modelled by a repeated slab with the metal layers separated by a vacuum region. Xe is absorbed only on one side of the slab, and a dipole correction is included to compensate for the polarisation of the slab. Brillouin zone integration is performed using the special \mathbf{k} -points given by Cunningham (1974). Exchange-correlation effects are treated within the LDA (Ceperly & Alder, 1980; Perdew & Zunger, 1981) and GGA-PBE approximations (Perdew *et al.*, 1996b). The binding mechanism is studied in terms of the charge density and the local density of states.

The chapter is organised as follow. In the next section, the commensurate $(\sqrt{3} \times \sqrt{3})R30^\circ$ structure is shown. Tests of convergence of the total energy as a function of the mixing parameters are discussed in section 4.3. In section 4.4, the convergence of the interaction potential is studied as a function of the cut-off energies, the number of special \mathbf{k} -points, the super cell parameters (number of substrate layers and size of the vacuum gap), and the fitting procedure for the interaction potential is discussed. In section 4.5, we present the interaction potential of Xe/Pt(111) obtained using the LDA and GGA-PBE approximations. Additionally, some aspects of the calculation that could affect the results are presented, namely the effect of non-linear core corrections, the lattice constant of the substrate and the self-consistency of the calculations. Adsorption mechanism on the top and hollow sites is considered in section 4.6. Adsorption at the hollow site is included

in order to show the low polarisation charge found there, which could explain the preference for Xe atoms to bind at the on-top site. Work function changes of the Pt substrate due to the adsorption of Xe are discussed in section 4.7 and finally, in section 4.8, the conclusions of the chapter are presented.

4.2 The commensurate $(\sqrt{3} \times \sqrt{3})R30^\circ$ structure

As was pointed out in the previous section, the adsorption of Xe atoms on the Pt(111) surface displays at least six phases depending on the substrate temperature and coverage (Kern *et al.*, 1988). At temperatures between 62 K and 99 K and at coverage of $\theta_{Xe} = 1/3$, a commensurate $(\sqrt{3} \times \sqrt{3})R30^\circ$ structure exists (Figure 4.2). The nearest neighbour spacing in the adlayer lattice is $\sqrt{3}$ times greater than the surface lattice constant and the adlayer lattice vectors (\mathbf{a}_{1a} and \mathbf{a}_{2a}) are rotated by 30° with respect to substrate lattice vectors (\mathbf{a}_{1s} and \mathbf{a}_{2s}).

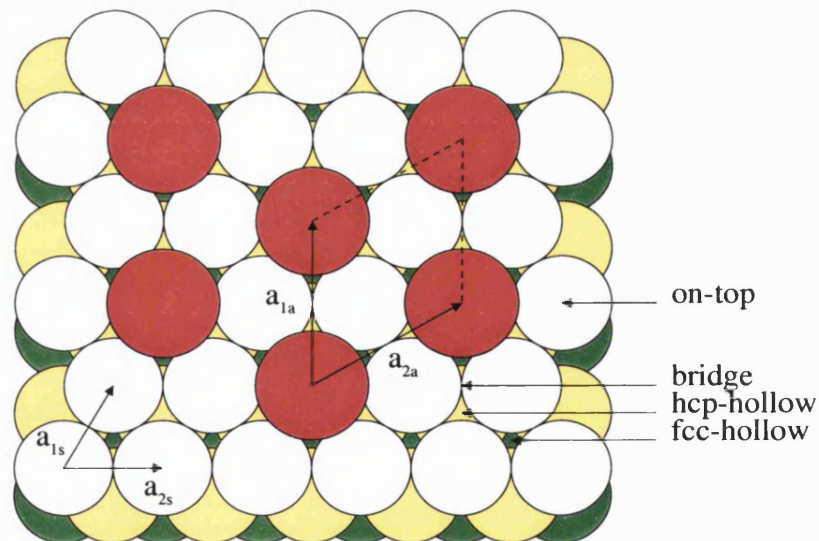


Figure 4.2: Real space commensurate $(\sqrt{3} \times \sqrt{3})R30^\circ$ structure of Xe on the Pt(111) surface and the sites available for adsorption. The subscript *s* denotes the substrate lattice vectors and *a* denotes the adlayer lattice vectors. Red circles represent the Xe atoms. White, yellow and green circles represent top, second, and third layers of the Pt substrate respectively.

4.3 Convergence of total energy

Before calculating the interaction potential energy for Xe on Pt(111), the convergence of the total energy was tested as a function of Kerker's mixing parameters A and G_0 (equation (2.59)). The aim of these tests is to find the parameters which optimise convergence of the total energy. Basically, the self-consistency procedure consisted of two steps. First, a Kerker mixing was used until a variation in the total energy less than a given tolerance was reached and then successive approximations for the charge density were determined with the Broyden mixing scheme (subsection 2.5.2). For each mixing scheme (Broyden and Kerker), it was necessary to calculate the best mixing parameters. In order to do this, the convergence of the total energy for a $(\sqrt{3} \times \sqrt{3})R30^\circ$ Xe/Pt(111) structure with 5 Pt layers and 9 vacuum layers (approximately 20 Å) was tested. Cut-off energies of 400 eV and 50 eV were used for the localised part and plane wave part of the electronic wave function (equation (2.37)) respectively. The irreducible Brillouin zone was sampled with one special \mathbf{k} -point (Cunningham, 1974). Note that these calculations are not well converged because of the low cut-off energies and the coarse \mathbf{k} -point sampling but this should not matter for testing the mixing scheme.

For a fixed value of G_0 , A was varied between 0.05 and 0.8 and the changes in the total energy, ΔE , and the charge density, $\Delta \rho$, were followed through the self-consistent calculation. These changes were defined as the difference between two successive iterations, $\Delta E = E^{n+1} - E^n$, $\Delta \rho = \|\rho^{n+1}(G) - \rho^n(G)\|$. Kerker mixing (equation (2.59)) was used until $\Delta E < 0.1$ eV. Subsequent approximations for the electronic charge density were obtained by using Broyden's method.

Figure 4.3 shows the convergence of total energy and charge density for a self-consistent calculation for selected values of A . Note that large values of A (0.8

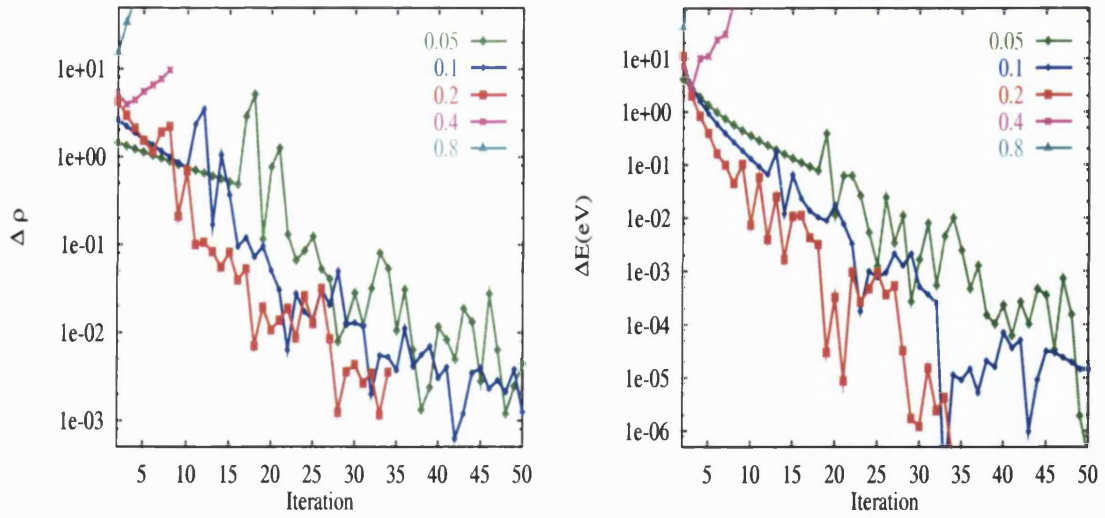


Figure 4.3: Convergence of the charge density (left) and the total energy (right) for $(\sqrt{3} \times \sqrt{3})R30^\circ$ Xe/Pt(111) for a selected set of values of the A parameter within a self-consistent calculation. $G_0 = 1.5 \text{ \AA}^{-1}$.

and 0.4) did not damp the electronic charge density and so the iterative procedure failed. For small values, a damping in the charge density was achieved for the first few iterations, but the value of 0.05 led to a slow convergence for the total energy. Although the value of 0.05 in Kerker's scheme damped the electronic charge density, this charge density was not a good approximation for starting the Broyden scheme because many iterations were required. The damping obtained with 0.2 and 0.1 was similar for the first few iterations, but with $A = 0.2$ less than 30 iterations were needed to reach a convergence of $\Delta E = 10^{-5}$ eV. In this case the value of 0.2 worked nicely for Kerker mixing and provided a good approximation of the charge density which gave a rapid convergence in the Broyden scheme.

The second series of tests consisted of fixing the value of A at 0.2 while G_0 was varied between 0.5 \AA^{-1} and 4.0 \AA^{-1} . Figure 4.4 shows the results obtained for this case. For $G_0 = 0.5 \text{ \AA}^{-1}$ the iterative procedure failed after the third iteration. With $G_0 = 1.0$ the charge density was damped for the first six iterations, but then $\Delta\rho$ started to grow and stayed nearly constant, so that a value for ΔE of less than 0.1 eV was not reached during the first fifty iterations, and as a consequence

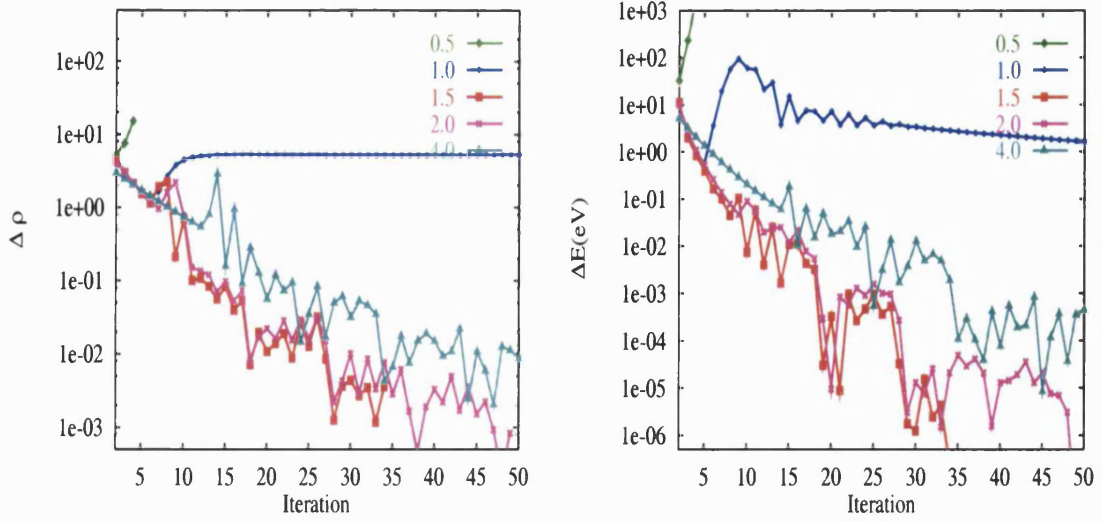


Figure 4.4: Convergence of the charge density (left) and the total energy (right) for $(\sqrt{3} \times \sqrt{3})R30^\circ$ Xe/Pt(111) structure for a selected set of values of the G_0 parameter within a self-consistent calculation. $A = 0.2$.

the Broyden mixing did not start. The values of 1.5 \AA^{-1} , 2.0 \AA^{-1} , and 4.0 \AA^{-1} damped the charge density with Kerker mixing, but faster convergence to $\Delta E = 0.1 \text{ eV}$ was reached with the values of 1.5 \AA^{-1} and 2.0 \AA^{-1} . Using the value of 1.5 \AA^{-1} provided a converged solution in less than 35 iterations with an accuracy better than 10^{-6} eV within Broyden mixing.

As was discussed in subsection 2.5.1, the convergence of the self-consistent procedure could be improved with the inclusion of an appropriate metric to evaluate the scalar product. We have used the scalar product defined by equation (2.60) and the metric given by Kresse & Furthmüller (1996b)

$$g_{ij} = \delta_{ij} \frac{G^2 + G_1^2}{G^2}. \quad (4.1)$$

Figure 4.5 shows the convergence of the total energy as a function of G_1 , which was varied between 0.05 \AA^{-1} and 4.0 \AA^{-1} . Note that with small values such as 0.05 \AA^{-1} or 0.5 \AA^{-1} , the number of iterations needed to reach convergence in the total energy of better than 10^{-6} eV was reduced when a comparison is made with no

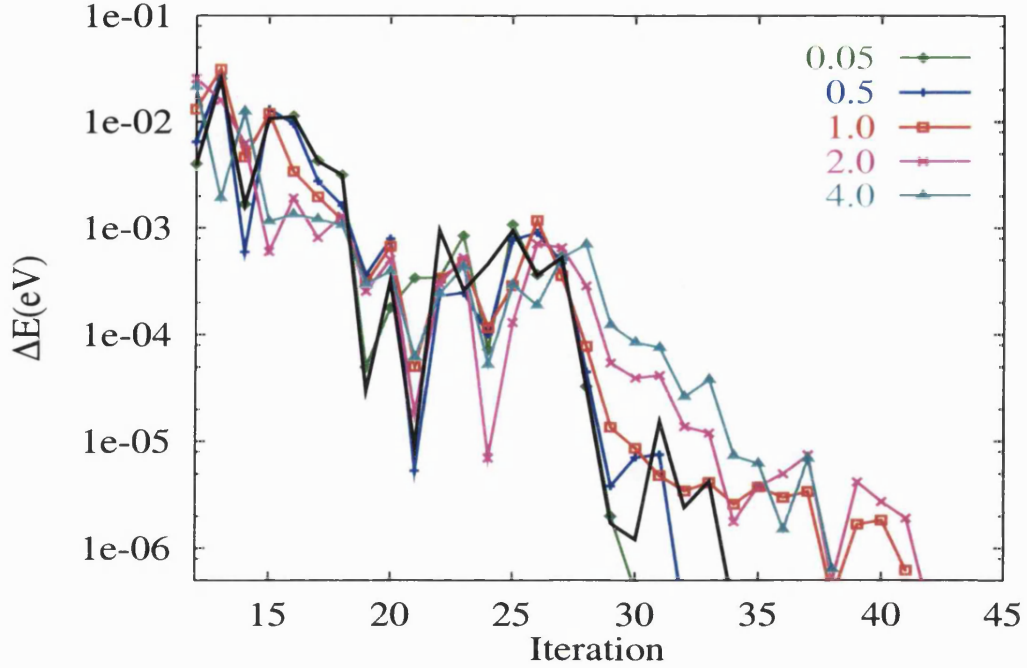


Figure 4.5: Convergence of the total energy for the $(\sqrt{3} \times \sqrt{3})R30^\circ$ Xe/Pt(111) structure with the inclusion of a metric in the evaluation of the scalar products for self-consistent calculations. Black line represents the results without preconditioning.

metric being used (black line). In general, it was observed that the correct choice of mixing parameters provides an important reduction in the number of iterations needed for reaching a required precision. The final choice of the mixing parameters was as follows: $A = 0.2$, $G_0 = 1.5 \text{ \AA}^{-1}$ and $G_1 = 0.05 \text{ \AA}^{-1}$.

4.4 Convergence of the interaction potential

The interaction potential energy was defined as

$$V(z) = E_{Xe/Pt(111)}(z) - E_{Pt(111)} - E_{Xe} \quad (4.2)$$

where $E_{Xe/Pt(111)}(z)$ is the ground state total energy of the Pt(111) slab with an adsorbed Xe atom at height z , and $E_{Pt(111)}$ and E_{Xe} are the ground state total

energies of the Pt(111) slab and the Xe atom respectively. The energies of the clean Pt surface and Xe/Pt were calculated within identical super-cells and keeping all parameters of the calculation (cut-off energies, number of \mathbf{k} -points, dimension of the supercell, etc.) constant. In order to guarantee a good level of accuracy, the convergence of the interaction potential energy was carefully checked as a function of the cut-off energies, the number of special \mathbf{k} -points, the number of Pt layers and the size of the vacuum gap.

4.4.1 Testing the cut-off energies

Within the formalism of the mixed basis scheme, there are two cut-off energies which need to be determined: the cut-off energy corresponding to the expansion of the pseudo-atomic orbitals, $E_{cut_{ao}}$ (first term of equation (2.37)), and the energy corresponding to the additional plane waves, $E_{cut_{pw}}$ (second term of equation (2.37)). In this subsection, we will show how these cut-off energies affect the interaction potential energy for an Xe atom located at a height of 3 Å above the top site of the Pt(111) surface. The cut-off energy of the expansion of the pseudo orbitals was varied between 400 eV and 600 eV while the additional plane wave cut-off was varied between 40 eV and 80 eV. Around these values we found that the structural properties of bulk Pt are well converged (see subsection 3.4.5). Table 4.1

$E_{cut_{pw}}$ (eV)	$E_{cut_{ao}}$ (eV)	V (meV)
40	500	264
60	400	268
60	500	270
60	600	270
80	500	271

Table 4.1: Interaction potential energy, V , for a Xe atom located at a height of 3 Å above the top site of the Pt(111) as a function of cut-off energies $E_{cut_{pw}}$ and $E_{cut_{ao}}$. The super cell consisted of five Pt layers and a vacuum gap equivalent to nine layers. Exchange-correlation effects were treating using the LDA.

summarises the results for a selection of cut-off energies. Note that $E_{cut_{ao}}$ of 500 eV provides a well converged solution and by using a bigger cut-off energy (for instance 600 eV), the interaction potential energy did not change significantly. In the case of the plane wave part, $E_{cut_{pw}}$, well converged results were obtained with 60 eV. We note that an increment from 60 eV to 80 eV caused a change in the potential energy of just 1 meV, but the required computing time was approximately twice as long per iteration. In accordance with the results obtained for the structural properties of Pt (see Table 4.1), we have fixed the cut-off energies at 500 eV and 60 eV for the expansion of the atomic orbital and the plane wave part of the electronic wave function respectively.

4.4.2 Testing k-point sampling

Within a electronic structure calculation, the most demanding computational part involves a series of separate calculations for each \mathbf{k} -vector. However when several \mathbf{k} -vectors are equivalent by symmetry, it is necessary to perform calculations only for one of them, which drastically reduces the computational load. In the case of the adsorption of Xe on a Pt(111) surface, depending on the adsorption site, an important reduction in computational time can be achieved if the point group symmetry is taken into account. The largest reduction was obtained for adsorption on the top, fcc hollow and hcp hollow sites. Here, due to the C_{3v} symmetry, one just needs to consider $\frac{1}{12}$ th of the full Brillouin zone (the irreducible wedge is shown in Fig. 4.6). For adsorption at the bridge site, the symmetry is reduced and a great portion of Brillouin zone must be considered. For this case, the symmetry corresponds to C_{2v} and $1/4$ of the Brillouin zone was used (see Figure 4.6, Γ KK'M'T area). In order to test the accuracy of the interaction potential as a function of the number of \mathbf{k} -points, we have calculated the potential for an Xe atom at the on top site and at a height of 3.0 Å above the Pt(111) surface, by sampling the

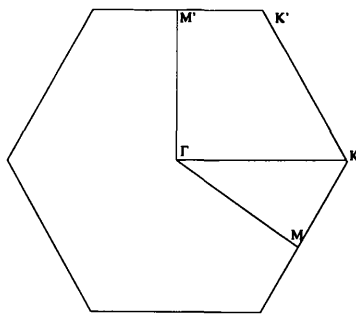


Figure 4.6: Two-dimensional Brillouin zone for a hexagonal lattice. The irreducible wedge ($\Gamma\text{KM}\Gamma$ area) was used in the total energy calculation at the top, fcc-hollow, and hcp-hollow sites while a $1/4$ of the Brillouin zone ($\Gamma\text{KK}'\text{M}'\Gamma$ area) was used for the bridge site.

irreducible Brillouin zone using 3, 6, and 18 \mathbf{k} -points within Cunningham's scheme (Cunningham, 1974). According to the results shown in Table 4.2, it appears that the interaction potential energy oscillates with respect to the number of \mathbf{k} -points, but with 6 \mathbf{k} -points well converged results were reached.

4.4.3 Testing the super cell parameters

A slab geometry was used to represent the adsorption of Xe atoms on the Pt(111) surface. We have studied the interaction potential as a function of the parameters that define the super cell. Table 4.3 shows the potential as a function of the number of Pt layers and the vacuum gap. The number of Pt layers was varied between 3,

k-points in IBZ	k-points in WBZ	V (meV)
3	18	256
6	54	270
18	162	268

Table 4.2: Interaction potential energy for a Xe atom located at a height of 3 Å above the top site of the Pt(111) surface as a function of the number of special \mathbf{k} -points in the irreducible Brillouin zone (IBZ). The calculations were performed using $E_{cut_{ao}} = 500$ eV and $E_{cut_{pw}} = 60$ eV. WBZ represents the number of \mathbf{k} -points in whole Brillouin zone. The super cell consisted of five Pt layers and a vacuum gap equivalent to nine layers. Exchange-correlation effects were treated using the LDA.

5 and 7 layers and we observed that the potential energy changed by 3 meV for an increment from 5 and 7 layers. A similar change was obtained when the vacuum gap was varied from 7 to 11 equivalent layers. The results show that five layers of Pt and a vacuum gap of nine layers are big enough to obtain a well converged potential with respect to the super cell parameters.

Pt layer	vacuum layer	V (meV)
3	9	242
5	7	267
5	9	270
7	11	271

Table 4.3: Interaction potential energy, V , for an Xe atom located at a height of 3 Å above the top site of Pt(111) surface as a function of the number of Pt layers and equivalent vacuum layers. The irreducible Brillouin zone was sampled with 6 k -points. The LDA was used for describing exchange correlation effects. The calculations were performed using $E_{cut_{ao}} = 500$ eV and $E_{cut_{pw}} = 60$ eV.

4.4.4 Fitting the potential data

Previously, we have presented results for the interaction potential as a function of the main parameters that affect the accuracy of a self-consistent calculation using a mixed basis set and a super cell geometry. In this subsection, we discuss the fitting procedure used to plot the interaction potential. First, the potential was calculated for a set of points uniformly distributed between 2.0 Å and 5.0 Å (nine points in total). This data was then least-squares fitted to an interpolating polynomial given by

$$P(x) = a_0 + a_1x + a_2x^2 + a_3x^3 + a_4x^4 + a_5x^5 + \dots \quad (4.3)$$

where $x = 1/z$. In order to test the selection made of the independent variable in equation (4.3), we have compared curves generated with $x = 1/z$ and $x = z$, see Figure 4.7. We find that using the inverse of z as the independent variable in a fifth degree polynomial (blue line) gives a better fit than $z = x$ for a polynomial of

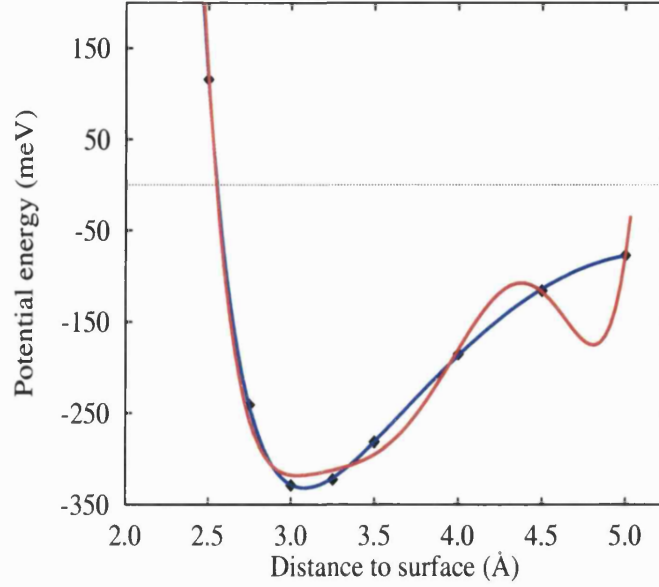


Figure 4.7: Interaction potential energy for the $(\sqrt{3} \times \sqrt{3})R30^\circ$ Xe/Pt(111) structure at the top site fitted to fifth degree polynomial. Blue line corresponds to the case with $x = 1/z$ used as the independent variable in equation(4.3) while the red line corresponds to a fifth degree polynomial with $x = z$. The LDA was used to describe exchange-correlation effects. Diamond symbols represent the calculated points.

the same degree (red line).

Before calculating the interaction potential at different adsorption sites, we tested the efficiency of the fitting using $x = 1/z$ for the potential curves obtained with the LDA and GGA-PBE. Figure 4.8 shows the potential obtained with both exchange-correlation approximations as a function of the order of the interpolating polynomial. We found that a polynomial of fifth degree provided a good fit for the potentials for both cases, see Table 4.4.

The perpendicular vibrational energy

$$E_v = \hbar\omega, \quad (4.4)$$

was obtained using the harmonic approximation with the angular frequency calcu-

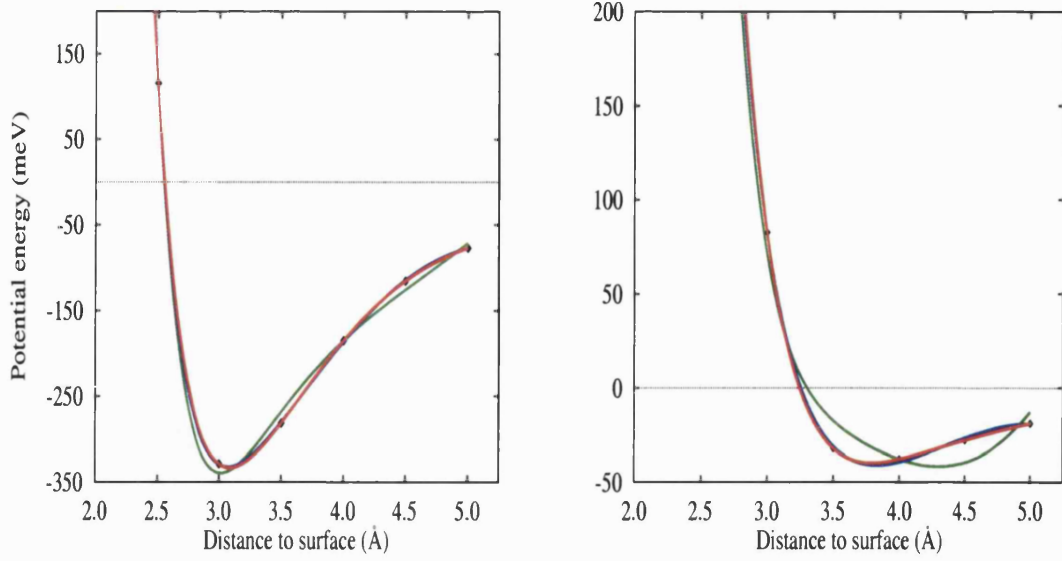


Figure 4.8: Interaction potential energy for the $(\sqrt{3} \times \sqrt{3})R30^\circ$ Xe/Pt(111) structure as a function of the height above the first surface layer, fitted to different orders of polynomial equation (4.3). Left panel corresponds to calculations made with the LDA and right with the GGA-PBE. Diamonds correspond to the calculated points; the solid lines represent curves obtained with polynomials of order 4 (green line), 5 (blue line), and 6 (red line) respectively. For both cases the inverse of z was used as the independent variable.

lated by

$$\omega = \sqrt{\frac{k}{M_{Xe}}}, \quad (4.5)$$

where M_{Xe} is the mass of the Xe atom and the constant k was obtained by calculating the second derivative of the potential energy evaluated at the equilibrium position.

Finally, an additional test was made on the estimation of the well depth and equi-

Degree	LDA			GGA-PBE		
	V_0 (meV)	Z_0 (Å)	E_v (meV)	V_0 (meV)	Z_0 (Å)	E_v (meV)
4	335	3.06	6.5	42	4.20	1.8
5	332	3.11	5.6	41	3.82	2.1
6	333	3.12	5.7	40	3.80	2.0

Table 4.4: Calculated well depth, V_0 , equilibrium height, Z_0 , and vibrational energy, E_v , for Xe atoms adsorbed on the Pt(111) surface as a function of the interpolating polynomial.

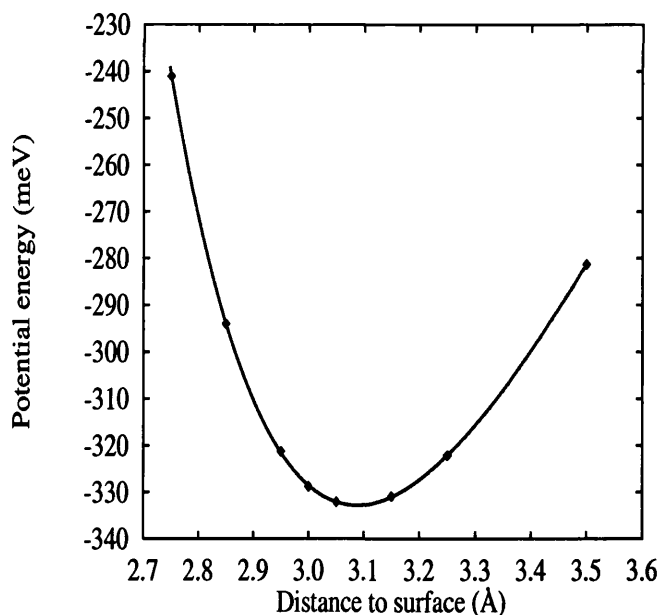


Figure 4.9: Fitted interaction potential energy around the equilibrium point.

librium height. The use of fairly widely spaced points could have an effect on the calculated value of the equilibrium well depth, and its height above the surface. We have therefore re-calculated the equilibrium height by using a set of eight points in the range between 2.75 Å and 3.50 Å (Figure 4.9). It is found that the well depth differed from the results shown in Table 4.4 by just 1 meV.

4.5 Interaction potential

In section 4.4 the main parameters involved in a total energy calculation using a mixed basis set and a super cell approximation were determined. In summary, the final choice of parameters was as follows: 500 eV for the expansion of the pseudo orbitals, 60 eV for the extra, low-energy plane waves, the surface Brillouin zone was sampled by 6 k-points for C_{3v} or 15 k for C_{2v} in the irreducible wedge, and the supercell contained five Pt layers and nine equivalent layers of vacuum (which is approximately 20 Å). In general, we have found that such parameters provide a precision of order 5 meV in the interaction potential for the $(\sqrt{3} \times \sqrt{3})R30^\circ$

Xe/Pt(111) system, taking as a reference calculations based on the LDA.

The energy of an isolated Xe atom was calculated in a $(15 \text{ \AA})^3$ box with the same cut-off energies as for the slab calculations. Because the reference is taken to be an isolated Xe atom, our calculated potentials include the lateral interaction energy of a layer of Xe atoms in the $(\sqrt{3} \times \sqrt{3})$ structure. This energy is found to be -59 meV and -17 meV for the LDA and GGA-PBE respectively, where the minus sign indicates that the interaction is attractive. The equivalent value for the Barker-Rettner potential is -56 meV, and, on the basis of fits to thermal desorption data, Widdra *et al.* (1998) estimate a value of -33 meV.

The interaction potential curves were calculated for Xe at the on-top, fcc-hollow, hcp-hollow and bridge sites on the Pt(111) surface (see Figure 4.2), and using both the LDA and GGA-PBE approximations. In each case, the lattice constant used for the Pt slab is given in Table 3.9. The most striking feature of the calculated potentials is the weakness of the interaction obtained with the GGA-PBE form (Figure 4.10). Our results show that the GGA-PBE predicts a potential with a binding energy of 41 meV (Table 4.5) that is much lower than values reported in the literature (Kern *et al.*, 1988; Müller, 1990; Barker & Rettner, 1992; Widdra *et al.*, 1998). In contrast, the LDA gives a value of 332 meV which is in reasonably good agreement with the most recent experimental estimate of 286 meV (Widdra *et al.*, 1998). The equilibrium LDA adsorption height of 3.11 Å is also in fairly good agreement with Barker and Rettner's (Barker & Rettner, 1992) value of 3.35 Å and the recent LEED measurement of 3.4 Å (Seyller *et al.*, 1999). However, there is a considerable discrepancy in the vibrational energy for both the LDA and GGA-PBE. By comparing our estimates of the vibrational energy with the value of 3.7 meV reported by Hall *et al.* (1989), we find that both results differ by a factor of about 2. Both the LDA and GGA-PBE predict that the Xe-surface binding is strongest at the on-top site.

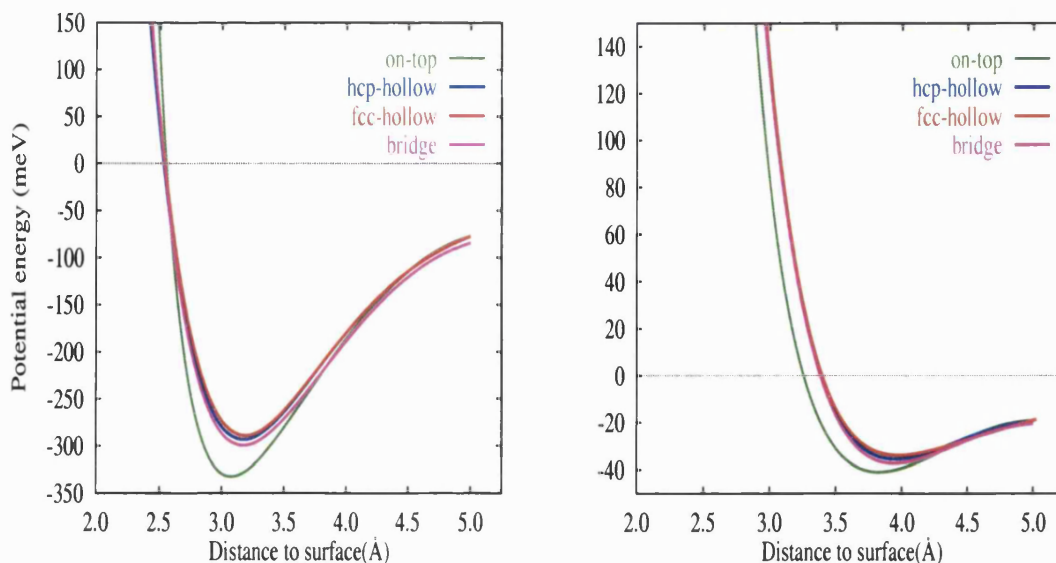


Figure 4.10: Interaction potential energy for the $(\sqrt{3} \times \sqrt{3})R30^\circ$ Xe/Pt(111) structure at selected adsorption points over the surface (see Figure 4.2). Left corresponds to results with LDA approximation and right with GGA-PBE approximation.

Our DFT-based potentials were compared with the experimentally derived potentials of Barker & Rettner (1992). The parameterisation of Barker and Rettner’s potential is the same as that used by Kulginov *et al.* (1996). Although the Barker-Rettner potential curves cannot be regarded strictly as experimental results, the fact that they reproduce a wide range of experimental data means that they should be at least qualitatively correct. Results for the on-top, fcc-hollow and bridge sites are shown in Figure 4.11. The interaction potential energy at the hcp-hollow site (not shown) is very similar to the fcc-hollow site, see Figure 4.10. It is clear that in the case of the GGA results are in qualitative as well as quantitative disagreement

	LDA			GGA-PBE		
	V_0 (meV)	Z_0 (Å)	E_v (meV)	V_0 (meV)	Z_0 (Å)	E_v (meV)
on-top	332	3.11	5.6	41	3.80	2.0
hcp-hollow	292	3.17	4.8	35	3.94	1.9
fcc-hollow	287	3.18	4.8	34	3.97	1.7
bridge	299	3.17	4.8	36	3.94	1.8

Table 4.5: Calculated well depth, V_0 , equilibrium height, Z_0 , and vibrational energy, E_v , for Xe atoms adsorbed on the Pt(111) surface in different adsorption sites.

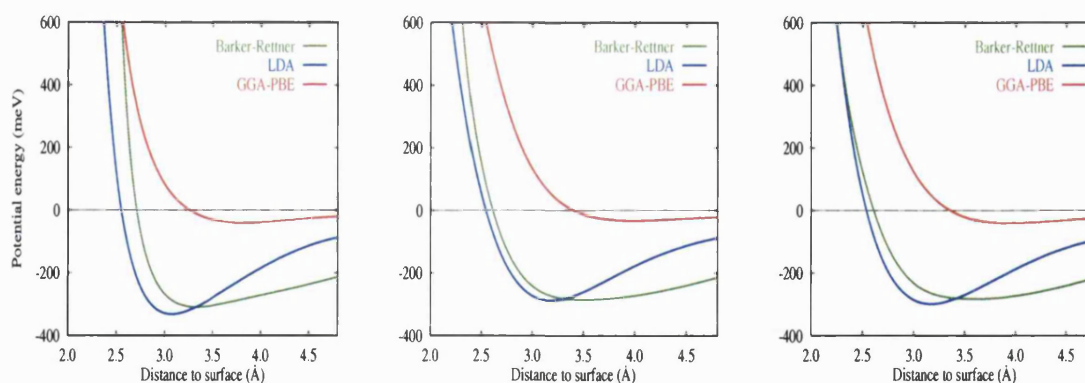


Figure 4.11: Interaction potential energy as a function of height from the first surface layer. Left at the on-top, centre fcc-hollow and right bridge site.

with experiment. However, the LDA potentials agree reasonably well with the Barker-Rettner curves in the near-surface region, particularly for the hollow and bridge sites. The discrepancy observed in the longer-ranged, attractive part of the well in Figure 4.11 is expected as it is well known that the LDA fails to describe the asymptotic Van der Waals interaction (Lang & Nørskov, 1983).

4.5.1 Dependence of the interaction potential with parameters of the calculation

Figure 4.12 shows a comparison between the interaction potentials calculated with and without the core-valence correction for Xe atoms adsorbed at on-top site. There is no significant variation in the results when non-linear core corrections were taken into account. In the case of the LDA there is a small shift up of the potential curve when non-linear core corrections are included while for GGA-PBE the changes are more noticeable around the equilibrium point. The well depth is slightly changed (8 meV for LDA and 2 meV for GGA-PBE, see Table 4.6) while the equilibrium adsorption height and the vibrational energy are almost constant.

On the other hand, we found that the potential well depth, equilibrium adsorption

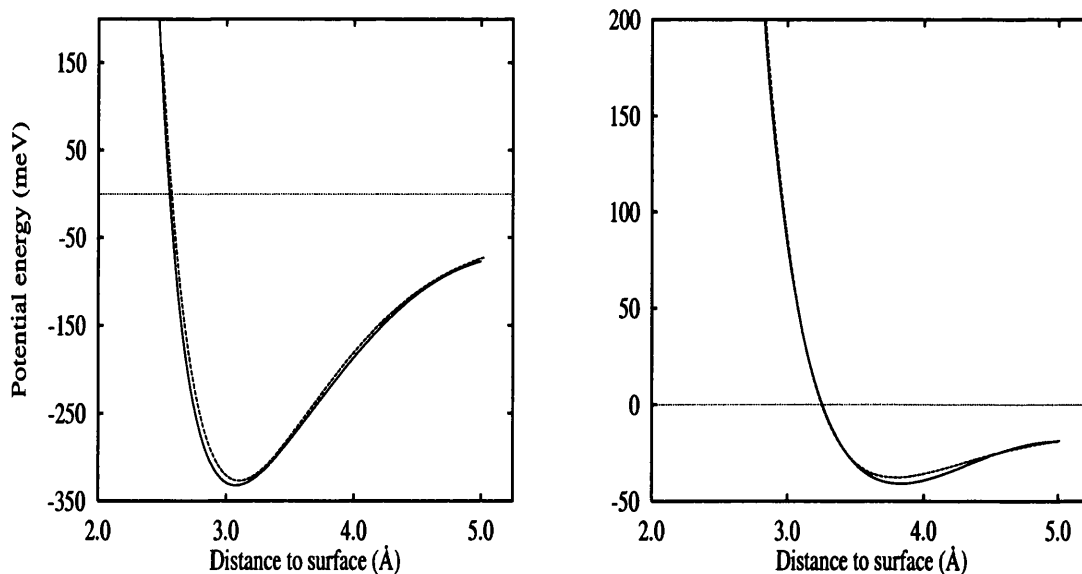


Figure 4.12: Effect of non-linear core-valence exchange-correlation corrections on the interaction potential energy. Left corresponds to results obtained with the LDA and right with the GGA-PBE. Solid line represents results without non-linear core-valence corrections and dashed line including non-linear core corrections.

height and vibrational energy are quite sensitive to changes in the lattice constant. For example, the potential well depth can be altered by more than 10 % if the Pt atoms are placed at the GGA lattice constant for a LDA calculation (see the third row of Table 4.6).

Another situation that could affect the estimation of the interaction potential is related to the self-consistency of the calculations. We observed that the potential energy curves are sensitive when non-consistent calculations are made, in other

	V_0 (meV)	Z_0 (Å)	E_v (meV)
LDA–NLCC	324 (8)	3.11 (0.00)	5.8 (0.0)
PBE–NLCC	39 (2)	3.79 (0.01)	2.0 (0.0)
LDA with GGA-PBE lattice constant	374 (42)	3.01 (0.10)	6.7 (0.5)

Table 4.6: Calculated potential well depth, V_0 , equilibrium height, Z_0 , and vibrational energy, E_v , for Xe atoms adsorbed on the Pt(111) surface at the on-top site. Lattice constant used for LDA calculations was 3.93 Å and for GGA-PBE, 4.02 Å. Numbers in parentheses indicate the absolute error with respect to result without non-linear core corrections (NLCC).

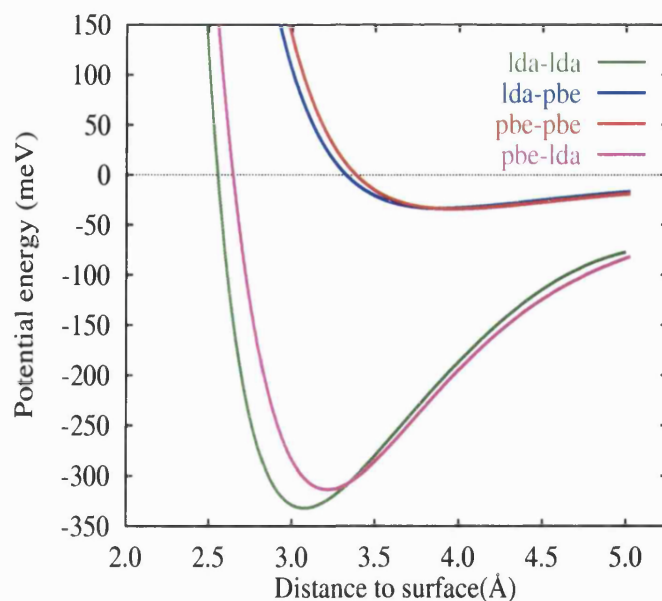


Figure 4.13: Interaction potential energy for the $(\sqrt{3} \times \sqrt{3})R30^\circ$ Xe/Pt(111) structure for consistent and non-consistent calculations. The first acronym before the dash indicates the approximation used for the exchange-correlation energy in the pseudopotential construction and the second one corresponds to that used in the total energy calculation. The lattice constant used for all case was the value obtained with LDA approximation, 3.93 Å.

words, when the approximation used for the exchange-correlation energy in the pseudopotential construction is different from that in the mixed basis set calculation. Figure 4.13 shows that there is a significant change in the potential well depth and the equilibrium height with both the LDA and GGA-PBE approximations. In addition, it is noticeable that there is a change in the repulsive part of potential. In the case of the combination PBE-LDA, the potential is more attractive while the opposite occurs for LDA-PBE.

4.6 Binding mechanism

4.6.1 Adsorption at the top site

We now turn to an analysis of the binding mechanism for Xe on Pt(111). All the results in this subsection refer to LDA calculations at the on-top site and at the calculated equilibrium adsorption height. Figure 4.14 displays a slice of the charge density difference

$$\Delta\rho = \rho(\text{slab} + \text{Xe}) - \rho(\text{slab}) - \rho(\text{Xe}) \quad (4.6)$$

induced by the adsorption of Xe atoms. The slice is along the $[\bar{1}\bar{1}2]$ direction (see Figure 4.15). According to Figure 4.14, it can be seen that the adsorption causes a re-organisation of the electronic charge around both the Xe and the Pt surface atoms, which produces an important change in the work function (see section 4.7).

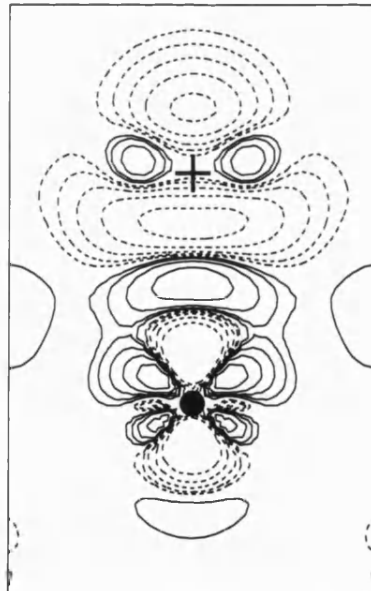


Figure 4.14: Electronic charge density difference induced by the adsorption of Xe atoms at the on-top site. Positive values are shown by solid lines and negative values with dashed lines. The contour lines represent densities given by $\pm 2^n \times 10^{-3} e \text{ \AA}^{-3}$ with $n = 1, \dots, 5$. The position of the Xe and Pt atoms are shown by the cross and bullet symbols respectively.

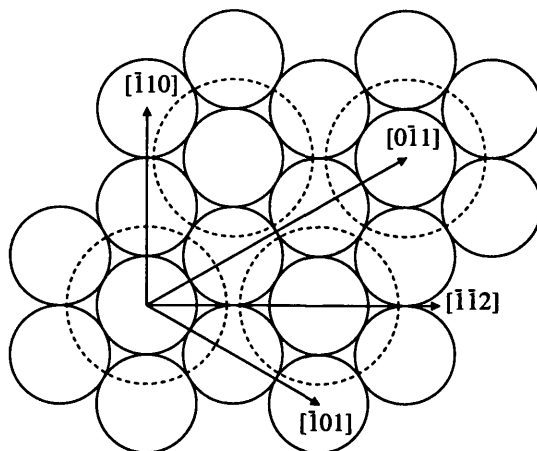


Figure 4.15: Adsorption of Xe on Pt(111) and some key directions in the (111) surface. Xe atoms are represented by dashed circles and the Pt atoms in the first layer by full circles.

The information that one can obtain from Figure 4.14 is just a qualitative description of the adsorption. In order to obtain further information, we have calculated the induced charge in each orbital by using the projected density of states (see subsection 2.5.4). We find that the integrated charges defined by equation (2.63) for the pseudo-atomic orbitals sum to a value somewhat greater than the total number of electrons in the system, and the plane-wave components compensate for this overcounting. Overcounting is more significant for the metallic system; in the case of bulk Pt, the magnitude of the plane-wave charge component is about $1.5e$ per atom, while for the Xe atom, as a result of the well-localised orbitals, it is only $0.02e$ per atom.

To investigate the charge redistribution further we have calculated the total charge

	s	p_x	p_y	p_z	d_{xy}	d_{yz}	d_{zx}	$d_{x^2-y^2}$	d_{z^2}	Total
Xe	+0.01	+0.03	+0.02	-0.91	+0.02	+0.12	+0.11	+0.01	+0.18	-0.41
Pt	-0.26	+0.13	+0.10	+0.64	+0.08	+0.14	+0.11	+0.09	-0.54	+0.49

Table 4.7: Difference of the charge Q^i (in $10^{-1}e$) upon Xe adsorption at the on-top site for Xe and Pt orbitals. For Xe and Pt we refer to the $5s$, $5p$, $5d$ and $6s$, $6p$, $5d$ orbitals respectively. The Pt atom was directly below the adsorbed Xe.

associated with particular orbitals. Table 4.7 shows the charge upon Xe adsorption in the integrated charge Q^i in the Xe orbitals and for the orbitals of the Pt atom directly below the adsorbed Xe. These orbitals are singled out because they show by far the largest changes. The Xe atom transfers approximately $0.05e$ to the Pt surface. However, there is also an internal reorganisation within the Xe atom, consistent with the bonding charge density shown in Figure 4.14, with a small occupation of $5d$ orbitals at the expense of the $5p_z$ state. It is interesting to note that the equivalent change in the charge associated with the low-energy plane-wave component in equation (2.37) is $-0.021e$. This is significant, because the adsorption of Xe on metal surfaces has frequently been discussed in terms of an interaction with the Xe $6s$ resonance (Eigler *et al.*, 1991; Buldum & Ciraci, 1996; Narloch & Menzel, 1998). Because the $6s$ orbital is not included explicitly in our basis, we would expect its effects to be observed in the low-energy plane-wave component. The fact that the change in the plane-wave occupancy is negative implies that the plane waves contribute less in the combined adsorption system than in the component systems. Although one has to be careful not to over-interpret these small occupancy changes, our results indicate that it is the $5d$ resonance, rather than the $6s$ resonance, which has the most significant effect in the binding.

This picture is supported by the projected density of states, as defined by equation (2.62). Figure 4.16 shows the density of states projected onto the orbitals of three Pt atoms. A comparison is made between the two inequivalent Pt atoms in the top layer of the slab and an atom in the bottom layer, which is essentially unaffected by Xe adsorption. The adsorption of a Xe atom is seen to make little difference to the Pt atom in the top layer further away from the adsorbate. However, for the Pt atom directly below the Xe atom, there is a distinct feature around 4.5 eV below the Fermi energy for the $5d_z^2$ orbital (this orbital has the largest effect), which is associated with the interaction with the Xe $5p$ orbitals (mainly $5p_z$). This interaction also causes a broadening of the $5p$ states of the Xe atom, as shown in

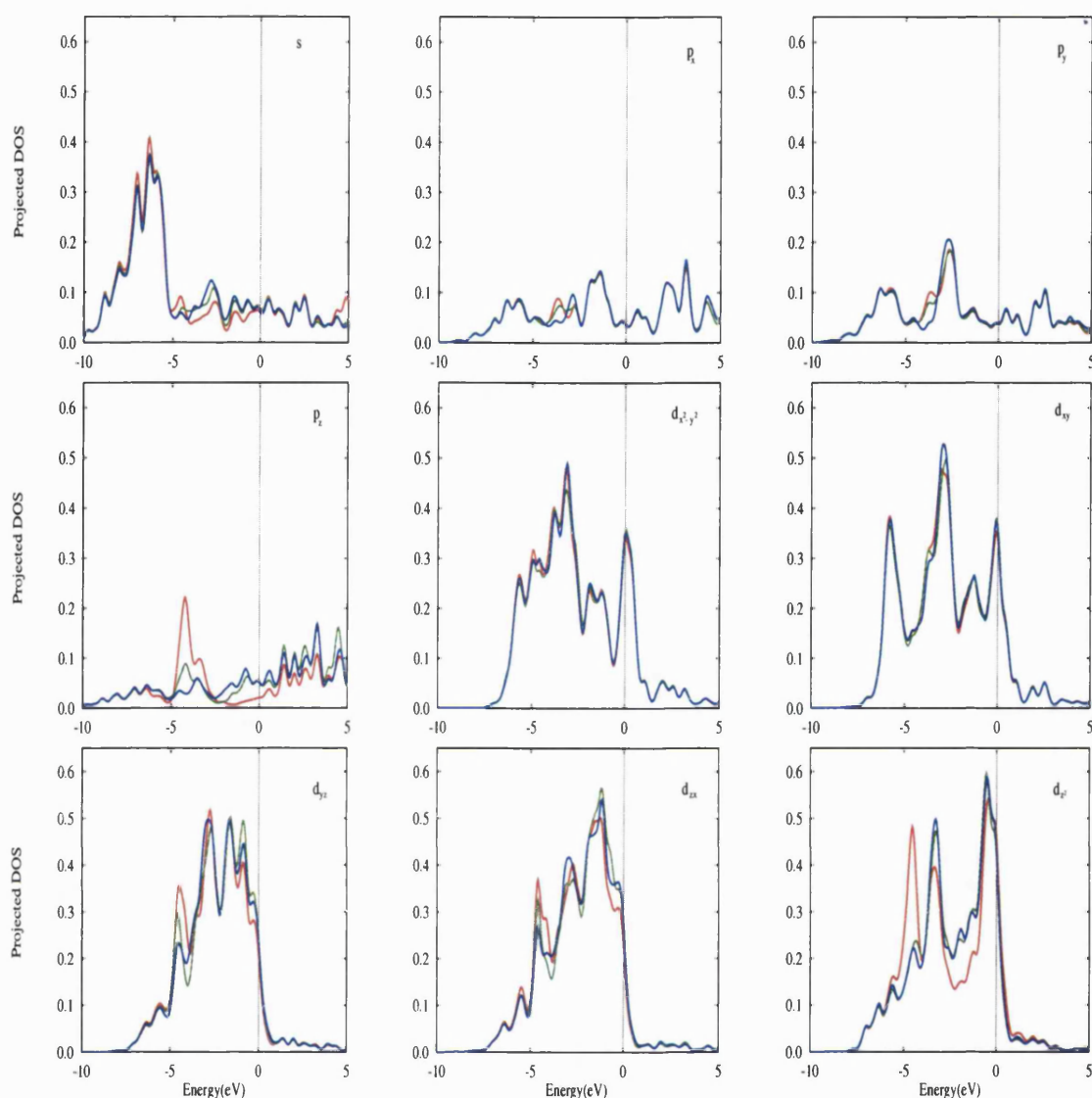


Figure 4.16: Local density of states projected onto the orbitals of selected Pt atoms; the Pt atom directly below the Xe atom is represented by a red line, the inequivalent Pt atom in the top layer is represented by green line and a Pt atom in the bottom layer is represented by a blue line.

the left panel of Figure 4.17. A weak mixing of the $5p$ and $5d$ states of Xe is observed around the Fermi level (Figure 4.17, right panel) which is consistent with the occupancy changes shown in Table 4.7 and the bonding charge density shown in Figure 4.14. The equivalent plot for the low-energy-plane wave component shows no obvious feature around the Fermi level, again indicating that the $6s$ resonance plays little part in the binding.

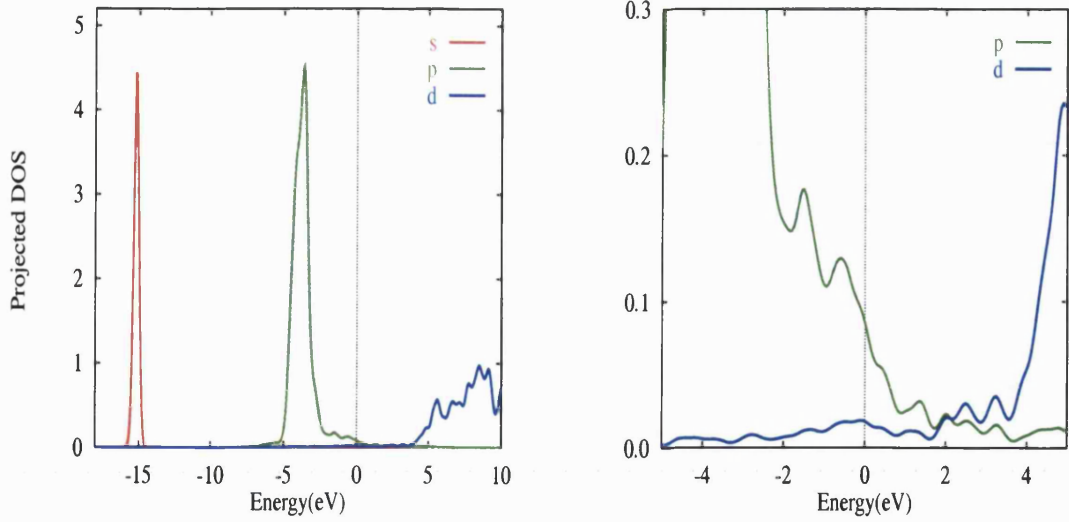


Figure 4.17: The local density of states projected onto Xe orbitals (left panel). $5s$, $5p$ and $5d$ are represented by green, blue and red lines respectively. Close-up around the Fermi level (right panel).

4.6.2 Adsorption at the hollow site

We have also analysed the adsorption at the hcp-hollow site, in order to find any reason for the preference for binding at the on-top site. Figure 4.18 shows the electronic charge density difference induced by Xe atoms at the hcp-hollow. In contrast with adsorption at the top site, adsorption at the hcp-hollow produces a smaller polarisation of the Xe atom. Table 4.8 shows that the charge transfer from the Xe atoms is $-0.031e$. The variation of charge observed on the Pt atoms belonging to the top and second layers was $+0.009e$ and $+0.001e$ respectively. While the change in the charge associated with the low-energy plane-wave component is

	s	p_x	p_y	p_z	d_{xy}	d_{yz}	d_{zx}	$d_{x^2-y^2}$	d_{z^2}	Total
Xe	+0.03	-0.06	-0.07	-0.52	+0.02	+0.09	+0.08	+0.02	+0.10	-0.31
Pt _{tl}	-0.08	+0.03	+0.03	+0.20	-0.05	+0.05	+0.05	-0.06	-0.08	+0.09
Pt _{sl}	-0.01	+0.01	+0.01	+0.05	-0.02	+0.01	-0.01	+0.01	-0.04	+0.01

Table 4.8: Difference of the charge Q^i (in $10^{-1}e$) upon Xe adsorption at the hcp-hollow site for Xe and Pt orbitals. For Xe and Pt we refer to the $5s$, $5p$, $5d$ and $6s$, $6p$, $5d$ orbitals respectively. Pt_{tl} and Pt_{sl} represent Pt atomic in the top layer and second layer respectively.

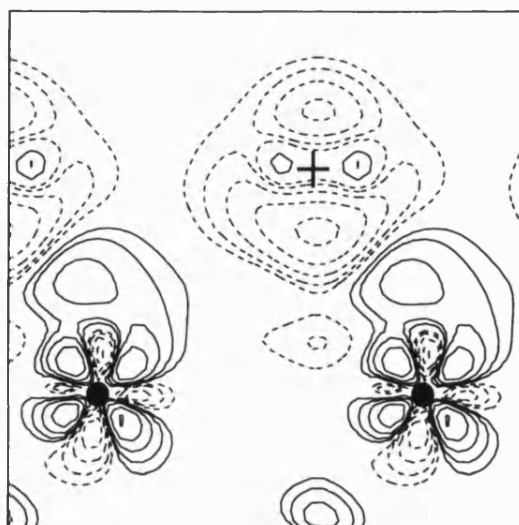


Figure 4.18: Electronic charge density difference induced by the adsorption of Xe atoms at the hcp-hollow site. Positive values are shown by solid lines and negative value with dashed lines. The contour lines represent densities given by $\pm 2^n \times 10^{-3} e \text{ \AA}^{-3}$ $n = 0, \dots, 5$. The position of the Xe and Pt atoms are shown by the cross and bullet symbols respectively.

$-0.012e$. These results show a smaller charge transfer in comparison with adsorption at the top site. We might therefore speculate that this smaller polarisation at the hollow site could explain why adsorption at the on-top site is favoured.

4.7 Work function change

As was discussed in subsection 4.6.1 the adsorption of Xe causes a redistribution of the charge density which in turn leads to a change in the work function of the Pt surface. In general, the work function of a surface is very sensitive to the redistribution of charge caused by the adsorption of atoms or molecules. Changes in the work function have been reported both in chemisorption and physisorption (Somorjai, 1994; Bruch *et al.*, 1997). For chemisorption, it is attributed to charge transfer between adsorbate and substrate, and for physisorption to the process of polarisation.

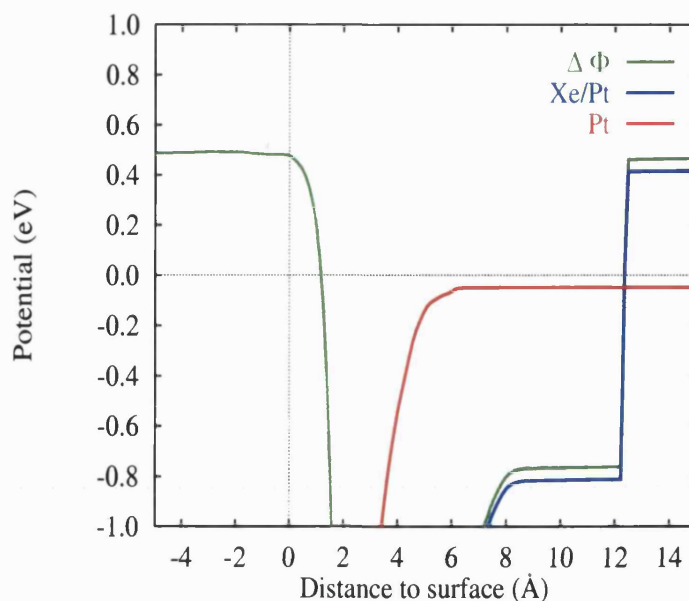


Figure 4.19: Planar-averaged potentials as a function of the distance perpendicular to the surface. Red curve corresponds to the potential produced by five Pt layers, blue curve is the potential of the Pt slab with an adsorbed Xe and the green curve is the difference between the curves.

We have calculated the work function change using two different procedures. In the first, we analyse the change of the potential in the vacuum region. Without an adsorbate on the surface, the potential in the vacuum gap is flat if the vacuum region is wide enough, see Figure 4.19 (red line). When Xe is adsorbed a small electric field appears in the vacuum region due to the polarisation of the surface. This is compensated in the standard way by adding an effective dipole layer in the vacuum gap. From this we calculate a change in the work function of -1.25 eV. The inclusion of a dipole correction leads to an additional energy given by

$$E_{dip} = \sum_i q_i V_{dip}(\mathbf{r}_i) \quad (4.7)$$

where q_i is the charge of the i th atom at the position \mathbf{r}_i and V_{dip} is the induced dipolar potential. Although the results of the well depth, equilibrium adsorption height and vibrational energy presented in previous sections were obtained without this contribution, the incorporation of a dipole correction does not significantly change those results. For example, we have re-calculated the well depth and equilibrium

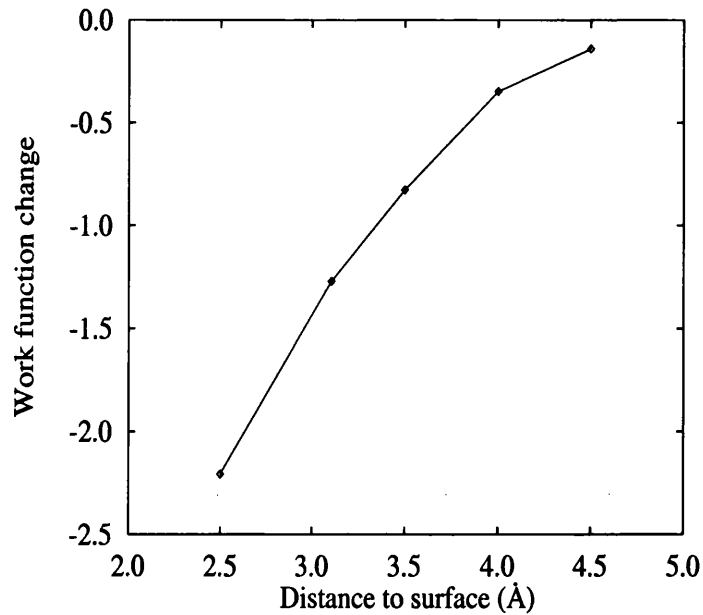


Figure 4.20: Work function change as a function of the adsorption height.

height for adsorption at the top site and have found the same values as those given in Table 4.5.

The second procedure used to determine the work function change involves calculating the dipole moment produced by the charge induced by Xe adsorption on the metal surface,

$$\Delta\Phi = -4\pi e \int z\delta\rho(\mathbf{r})d\mathbf{r}. \quad (4.8)$$

Here $\delta\rho$ is the change in the planar-averaged charge density and z represents the coordinate perpendicular to the surface. This procedure allows a direct evaluation of the work function change from the charge density. The value of work function change obtained at the equilibrium position was $\Delta\Phi = -1.27$ eV, which is in good agreement with Figure 4.19. However, our estimate of the work function change is inconsistent with the value of -0.6 eV obtained by Cassuto & Erhardt (1988) using angle-resolved photoemission. The cause of this discrepancy is not clear, but it is partly due to the fact that our LDA equilibrium adsorption height is lower than that reported in the literature. In order to find a better agreement with the work function change observed by Cassuto & Erhardt (1988), we have calculated

the work function as a function of the adsorption height (see Figure 4.20). The work function change is found to depend very sensitively on the height, and if it is calculated at the experimental adsorption height of 3.4 Å rather 3.11 Å, we obtain $\Delta\Phi = -0.9$ eV, which is closer to the experimental value.

4.8 Conclusions

First principles calculations of the interaction potential for Xe atoms on the Pt(111) surface have been presented. Neither LDA nor GGA-PBE potentials are in excellent agreement with the experimentally derived potentials of Barker & Rettner (1992) but the LDA potential is considerably closer. This is in contrast with the observation that the GGA usually gives substantially better adsorbate binding energies than the LDA. It is probably accidental that the LDA gives better agreement with experiment in this case, and our results should not be taken to imply that the general improvement in chemical binding energies provided by the GGA is invalid. However, they do show that a thoughtless application of DFT methods in less common situations, like rare-gas interactions, can lead to incorrect conclusions and that a careful benchmarking with respect to experiment is vital.

Although the LDA potential is closer to experiment, there are still significant errors in the well depth and adsorption height, and this overbinding is reflected in a substantial overestimation of the work-function change. The long-ranged part of the LDA potential, as expected, also shows a considerable deviation from experiment.

The binding mechanism of the Xe/Pt(111) system has been analysed via the density of states projected onto the atomic orbital and plane-wave basis functions of our mixed-basis method. A significant element of chemisorption is found, with the interaction with the Xe 5*d* resonance appearing to have the greatest effect in the

binding. The larger polarisation of the Xe atom at the on-top site could explain why Xe is adsorbed preferentially at this site.

Chapter 5

Interaction of light rare-gas atoms with the Rh(110) surface

5.1 Introduction

The main advantages of using low energy rare-gas atoms as the probe in diffraction are their non-destructive nature and their lack of reaction with the substrate. This allows the study of any kind of material: metals, semiconductors and insulators (Fariás & Rieder, 1998). When probe atoms with a constant kinetic energy impact on an surface, each incoming particle will experience a different turning point (for example, closer at the bridge site than at the top site). Therefore a periodic modulation of the repulsive part of the potential is produced. The resulting scattering surface is known as the corrugation surface which can be deduced from an analysis of atom diffraction data. In principle, knowledge of the surface corrugation allows the arrangement of the surface atoms to be determined provided that a simple relationship exists between the structure and the corrugation. In general the theoretical construction of the surface corrugation is difficult, but the use of simple

models has allowed useful information to be obtained from diffraction patterns.

For example, helium atom scattering (HAS) has been demonstrated to be a useful tool in the study of physisorbed layers of polar molecules. This is because it does not alter the surface structure and charging effects do not occur, allowing the determination of the orientation of the molecules with respect to the substrate in non-destructive way; as demonstrated by studies of CH₃F, CH₃Br, CH₃Cl, HCl and NH₃ on surfaces of graphite (Ruiz-Suárez *et al.*, 1988; Rowntree *et al.*, 1990). The high sensitivity of He to adsorbed hydrogen structures has allowed the determination of structures not previously observed with LEED studies (Witte *et al.*, 1995; Graham *et al.*, 1995, 1998).

The first Ne diffraction from a low-index metal surface was observed by Rieder & Stocker (1984) and Salanon (1984). Ne diffraction from (110) surface of Ni, Cu, Rh and Pd show a large corrugation amplitude (Rieder & Stocker, 1984, 1985; Parschau *et al.*, 1989) which indicates that Ne could provide better details of the surface atomic structure than He. In fact, it has been reported that Ne diffraction shows clearly the structure of NiAl(110) while He diffraction does not (Fariás & Rieder, 1998).

Using an effective medium approach, Esbjerg & Nørskov (1980) found that the repulsive part of the potential energy for an He atom is proportional to the unperturbed electron density of the substrate at the position of the He atom. However, comparisons made with He scattering measurements on the Ni(110) surface (Rieder & García, 1982) showed that the relationship between the repulsive part of the potential and the substrate electronic charge density is more complex than pointed out by Esbjerg & Nørskov (1980). In order to resolve the difference between these results, Annett & Haydock (1983, 1984) introduced a gradient correction term which reduces the corrugation of the potential. By carrying out local density cal-

culations, Harris & Zaremba (1985) found that the anticorrugating contribution should be at least one order of magnitude smaller than the value given by Annett & Haydock (1984). In response, Annett & Haydock (1986) used first principles calculations to support their initial conclusions. From He and Ne scattering from Ni(110) and Rh(110), Rieder *et al.* (1993) found that He atoms approach metal surfaces more closely at the on-top site than the bridge site (anticorrugating effect). In the case of Ne, the opposite effect was found. These results provide strong support for the Annett-Haydock model. Again using *ab initio* density functional theory calculations and solving the Kohn-Sham equations using the full-potential linear augmented plane wave method, Petersen *et al.* (1996) have calculated the interaction potential energy for He and Ne at the on-top site and at the short bridge site for the Rh(110) surface. They found the anticorrugation effect for He and Ne reported by Rieder *et al.* (1993). They claimed that the difference between these probe atoms is determined by the surface wavefunction at the Fermi level, where d_z^2 and d_{xz} orbitals play an important role in the scattering process. Recently, Trioni *et al.* (1998a) have shown that anticorrugating effects may also arise because of the different polarisations of He and Ne.

In order to continue our tests of the pseudopotential-mixed basis scheme applied to rare-gas atoms, we have used this scheme to calculate the interaction energy for He and Ne in the same way as was done for Xe/Pt. Our interest is focused on the question of whether such a procedure can provide an acceptable interpretation of the interaction between light rare-gas atoms and a metal surface. The exchange correlation effect will be approximated using both the LDA and GGA-PBE (see Chapter 2). It is not well established which approximation provides a better description of the interaction of light rare-gas atoms with a metallic surface. For instance, Trioni *et al.* (1998b) have claimed out that the LDA reproduces the interaction of He and Ne over the surface of Ag. However, Petersen *et al.* (1996) claimed that LDA results are in worse agreement with experiment in the case of

He and Ne over a Rh surface. Additionally, as was shown in Chapter 4, our study of Xe/Pt(111) demonstrated that the LDA gives a more realistic potential than the GGA. The Rh(110) surface has been chosen in order to compare our results with previous calculations based on an all-electron scheme (Petersen *et al.*, 1996). Although pseudopotentials for Rh are quite soft, those for He and Ne are very hard which may make it troublesome to use pseudopotentials in this kind of system. However we found (subsection 3.4.5) that pseudopotentials constructed for both rare-gas atoms provide results for their dimers which are in good agreement with previous all-electron calculations (Burda *et al.*, 1996; Patton & Pederson, 1997).

The chapter is organised as follow. In the section 5.2 full computational details are presented. Calculations of the relaxation of Rh(110) and tests of convergence for the interaction potential as a function of the cut-off energies, the number of special k -points, super cell parameters (number of substrate layers and vacuum gap) and the fitting polynomial are discussed. The interaction potential of He/Rh(110) and Ne/Rh(110) obtained with the LDA and GGA-PBE and the corrugation of the potential are studied in section 5.3. The polarisation charges are presented in section 5.4 and finally, in section 5.5, the conclusions of the chapter are presented.

5.2 Computational details

Any fundamental understanding of the microscopic properties of a solid surface requires a reasonable model of the atomic geometry. In the simplest model, it is assumed that the periodicity of the outermost layers is identical to that of an equivalent parallel layer in the bulk, and the spacing between neighbouring layers in the surface region is the same as in the inside of the crystal. However, this model in general does not represent the most stable structure. The coordination

of the surface atoms and the electronic structure in the selvedge region are not equal to the bulk, and some changes in the atomic geometry may take place for a real surface. If the rearrangement leads to a change in the interlayer spacing perpendicular to the surface, it is called relaxation. If the rearrangement results in a different two-dimensional geometry of one or more surface layers, it is called reconstruction. For the Rh(110) surface, reconstruction has not been reported but relaxation has. We have therefore calculated the interaction potential energy for He and Ne atoms on a Rh(110) surface by taking into account a surface with its first and second layers fully relaxed. The relaxation of the third layer was considered negligible (it is generally less than 1 % (Eichler *et al.*, 1996; Attard & Barnes, 1998)).

Another point emphasised in this section, as in the case of Xe/Pt, is a discussion on aspects of the calculations that could affect the accuracy of the interaction potential energy of light rare-gas atoms with a metallic surface. For this kind of system, the interaction potential energy is very weak and it is important to ensure that the main parameters that could affect our final results have been carefully controlled. Therefore, the convergence of the interaction potential energy was tested as a function of the number of special \mathbf{k} -points, the cut-off energies, the substrate thickness and size of the vacuum gap, etc., in order to determine the minimal computational requirements that guarantee precise results for the systems He/Rh and Ne/Rh.

5.2.1 Relaxation of the Rh(110) surface

The (110) surface atoms of fcc Rh have seven nearest neighbours while bulk atoms have twelve. To balance this loss of bonding, the surface undergoes an oscillatory change in the interplanar spacing. The surface relaxes such that the first atomic

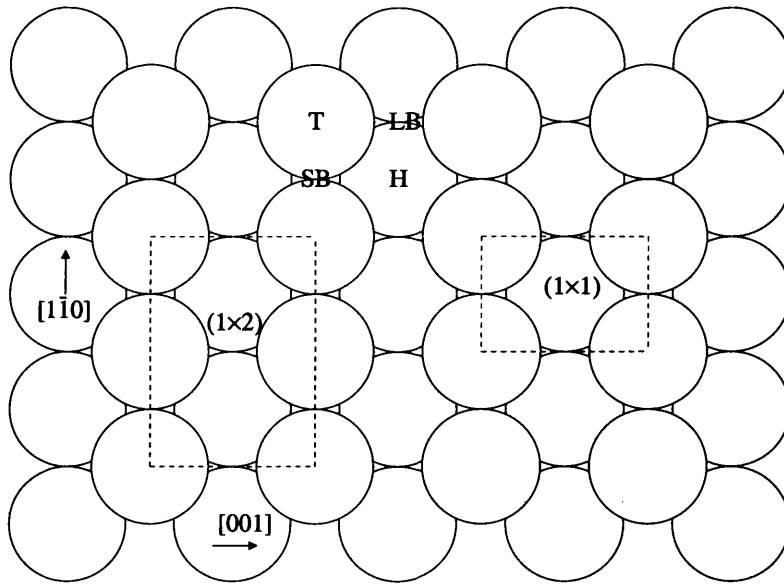


Figure 5.1: Schematic diagram of the (110) surface showing the unit cell used for (1×2) and (1×1) structures and the high symmetry sites available for adsorption. T : on-top, SB : short bridge, LB : long bridge, and H : hollow.

layer moves toward the second one to increase its coordination, the third atomic layer responds by expanding away from the second layer, hence compensating for the over-coordination of the second one. We have calculated the relaxation of Rh(110) using the procedure described below.

The relaxation of the Rh (110) clean surface (Figure 5.1) was simulated using a (1×1) surface cell, and the slab approximation. The super cell consisted of 5 Rh atomic layers separated by 10 Å of vacuum gap. The \mathbf{k} -space integration was done using a 12×8 special point mesh (Monkhorst & Pack, 1976) with 24 points inside the irreducible Brillouin zone. The number of special \mathbf{k} -points was chosen by taking into account the following criterion: the area of unit cell (Å²) times the number of \mathbf{k} -points in whole surface Brillouin zone should be approximately equal to 1000 (Bird, 1997). We have observed that a \mathbf{k} -point set chosen with this criterion is large enough to provide well-converged results.

The total energy was calculated as a function of the distance between two successive layers. The separation between the first and second atomic layers was varied

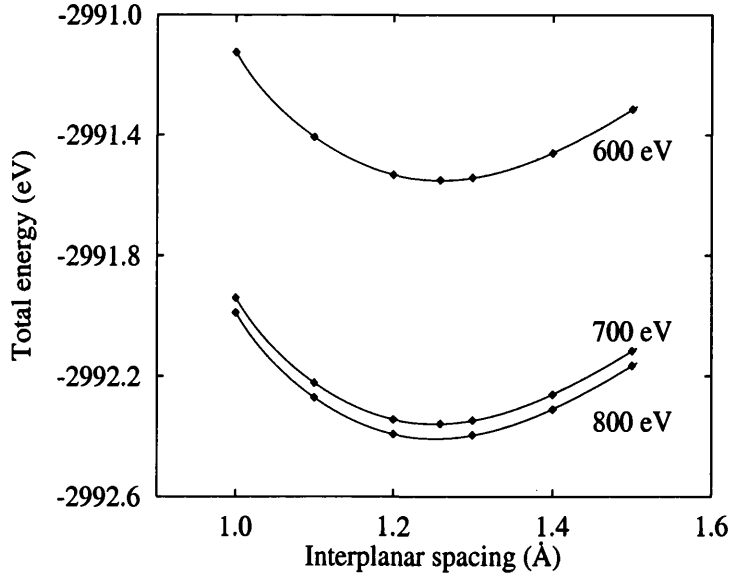


Figure 5.2: Variation of the total energy for the (1×1) Rh(110) structure as a function of the first interplanar spacing using the GGA-PBE approximation. The lattice constant used was 4.02 \AA , Table 3.9.

around its bulk equilibrium value (see Table 3.9), keeping other layers at their bulk equilibrium positions. Figure 5.2 shows the total energy as function of the interplanar spacing for selected cut-off energies corresponding to the localised orbital expansion, equation (2.37). The results show that a cut-off energy of 700 eV is large enough to provide a well-converged total energy, so this cut-off energy was used to calculate the surface relaxation. Once the equilibrium position of the first atomic layer was determined it was fixed at the calculated value, and the second atomic layer was varied by around 10% of the bulk equilibrium value, with the remaining atomic layers kept fixed. This procedure was iterated until the forces on the top two layers were negligible (less than 0.05 eV/\AA).

The calculated surface relaxation could be sensitive to the underlying lattice constant of the Rh slab, and we know that the theoretical lattice constant depends on the exchange-correlation approximation used (subsection 3.4.5). Therefore, we have calculated the relaxation of the Rh(110) surface using both the LDA and the GGA-PBE in a consistent way; the results are summarised in Table 5.1. Both approximations give the expected behaviour, with the first atomic layer relaxing

	$\Delta d_{12}/d_0(\%)$	$\Delta d_{23}/d_0(\%)$
LDA	-10.7	+3.3
GGA-PBE	-11.7	+3.6
US-LDA ^a	-9.8	+2.6
Exp ^b	-6.9	+1.9

^a From Eichler *et al.* (1996).

^b From Nichtl *et al.* (1987).

Table 5.1: Contraction/expansion of the separation of two subsequent atomic layers for the Rh (110) surface using the LDA and GGA-PBE. Δd is the change in the distance between two consecutive atomic layers, d_0 is the interlayer distance in the bulk. US-LDA represents an LDA calculation based on the ultrasoft pseudopotential method.

inwards while the second one relaxes outwards. When a comparison is made with results obtained by a LEED analysis (Nichtl *et al.*, 1987), we find that both approximations appear to overestimate the experimental relaxation. However our results are in good agreement with similar *ab-initio* calculations (Eichler *et al.*, 1996).

5.2.2 Testing convergence

Before calculating the interaction potential energy of He and Ne atoms on the Rh(110) surface at selected adsorption sites, Figure 5.1, convergence tests were carried out. Calculations were made for a (1×2) structure using five layer slabs, separated by 16 Å of vacuum (approximately twelve equivalent vacuum layers). The Brillouin zone was sampled with a 6×8 Monkhorst-Pack mesh, with 12 \mathbf{k} -points in its irreducible wedge. The exchange-correlation energy was described with the GGA-PBE. Changes of the interaction potential were tested as a function of the cut-off energies corresponding to the pseudo-atomic orbital expansion and the additional plane wave part, equation (2.37). Figure 5.3 shows the potential energy around the equilibrium height position for an He atom approaching the Rh (110) surface. It is again observed that a cut-off energy of 700 eV in the pseudo-atomic orbital expansion is large enough to obtain well-converged results. A difference of

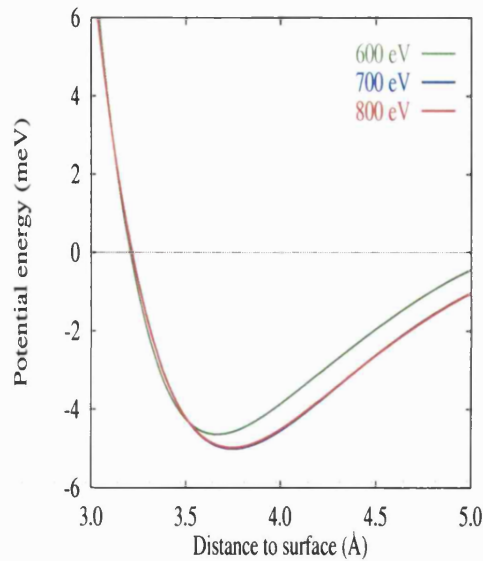


Figure 5.3: Interaction potential energy for the He/Rh(110) structure at the top site as a function of the cut-off energy for the pseudo-atomic orbital expansion (equation 2.37). The additional plane-wave cut-off energy was fixed at 60 eV. The exchange-correlation energy was approximated with the GGA-PBE.

only 0.1 meV was found for the potential well depth calculated with cut-offs of 700 eV and 800 eV. The same difference of 0.1 meV was also obtained when the cut-off energy corresponding to the additional plane waves was varied from 60 eV to 80 eV.

Additionally we have observed that if the Rh slab thickness is increased to seven layers, the interaction potential energy around the minimum of the well changes by only 0.1 meV. In this test, the vacuum region between Rh slabs was fixed at 16 Å; we have also found that an increment in the vacuum gap leads to a very small change in the interaction potential energy. For instance in the case of Ne/Rh(110), we found when the vacuum gap is increased from 16 Å to 20 Å the interaction potential energy changes by just 0.2 meV.

In summary, the final choice of parameters was as follows: 700 eV for the expansion of pseudo-atomic orbitals, and 60 eV for the extra low-energy plane waves. The irreducible surface Brillouin zone was sampled using 12 \mathbf{k} -points (Monkhorst &

Degree	Z_0 (Å)	V_0 (meV)
3	3.844	4.96
4	3.786	4.92
5	3.782	5.01
6	3.784	5.00
7	3.784	5.00

Table 5.2: Equilibrium height and potential well depth for He atoms interacting with the Rh(110) surface as a function of the degree of the interpolating polynomial.

Pack, 1976), and the super cell consisted of five Rh layers, separated by 16 Å of vacuum gap.

Because the interaction potential is quite weak for He and Ne, the accuracy of the fitting was checked by monitoring changes in the potential well depth and the equilibrium adsorption height. The potential was calculated from 1.5 Å to 5.5 Å (nine points) and least-squares fitting was used in the same way as described for Xe/Pt (see subsection 4.4.4). The calculated equilibrium height and potential well depth for He/Rh(110) as a function of the degree of the interpolating polynomial are shown in Table 5.2. Note that the changes in the potential well depth are quite small but the equilibrium height is a little more sensitive. A polynomial of low degree (four of five) is sufficient to obtain well-converged results. Similarly to the Xe/Pt case, we have re-calculated the interaction potential around the equilibrium point in order to check if the separation of the selected points has an important effect on the results presented in Table 5.2. By using seven points in the range from 3.4 Å and 4.0 Å and fitting with a fifth degree polynomial, we found that the equilibrium well depth changed by only 0.1 meV. The results shown in the next section were all calculated using a fifth degree polynomial fit.

5.3 He and Ne interacting with the Rh(110) surface

The energy of an isolated He and Ne atom was calculated in a $(12 \text{ \AA})^3$ box with the same cut-off energies as for the slab calculations. Because the reference is taken to be an isolated atom, our calculated potentials include the lateral interaction energy of a layer of He (or Ne). These energies are found to be -4.8 meV and -0.5 meV for the LDA and GGA-PBE respectively for He. The equivalent figures for Ne are -7.8 meV and -2.6 meV respectively.

Figure 5.4 shows the calculated interaction potentials for He and Ne. For both atoms, the LDA predicts an interaction potential considerable more attractive than the GGA-PBE. In the case of He/Rh(110), we find that the LDA gives a well depth at both the long and short bridge sites which are quite similar at around 20 meV (see Table 5.3) while at the top site the well is deeper by about 20 meV . On the other hand, with the GGA-PBE we also find the lowest energy at the top site but with a difference of less than 1 meV in comparison with the bridge

		He		Ne	
		Z_0 (\AA)	V_0 (meV)	Z_0 (\AA)	V_0 (meV)
LDA	T	2.43	42.2	2.86	65.4
	LB	2.88	20.5	2.93	55.1
	SB	3.01	21.6	2.64	62.4
PBE	T	3.75	5.0	3.61	13.0
	LB	3.67	3.7	3.64	12.4
	SB	3.82	4.5	3.42	14.2
Exp.		8.2 ^a			
Rh(110)(1×2)H ^b		2-3		8	

^a From Parschau *et al.* (1989).

^b From Rieder *et al.* (1993).

Table 5.3: Potential well depth, V_0 , and equilibrium height, Z_0 , for He and Ne interacting over the Rh(110) surface. Rh(110)(1×2)H corresponds to a hydrogen covered (110) surface of Rh.

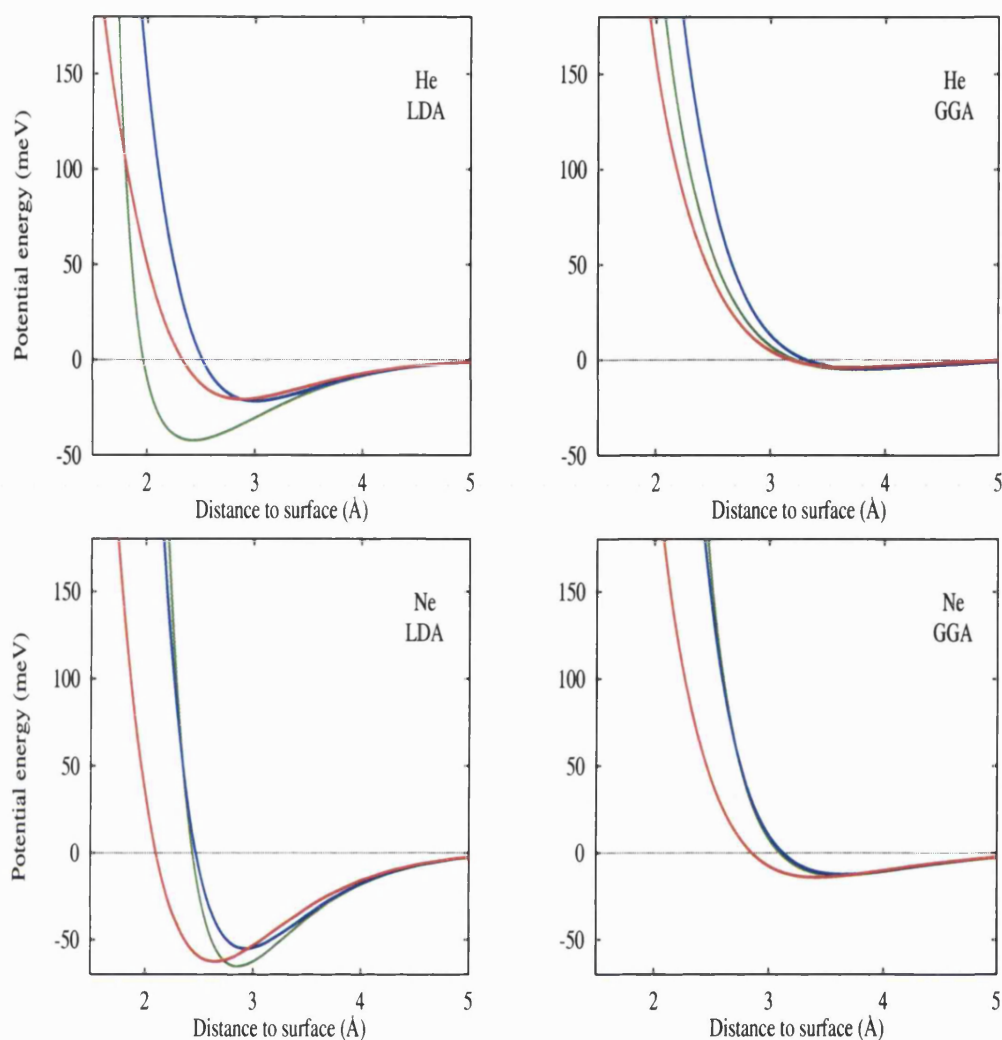


Figure 5.4: Interaction potential energy of He/Rh(110) (top right and top left) and Ne/Rh(110) (bottom right and bottom left) at on-top (green line), short bridge (blue line) and long bridge (red line) sites. Left LDA and right GGA-PBE.

sites. Selective adsorption experiments of He on the clean Rh(110) surface have provided an estimated potential well depth of about 8 meV (Parschau *et al.*, 1989). Consequently, the GGA seems to be in better agreement with experiments than the LDA. The large over-estimation of the well depth given by the LDA is a typical feature of the local approximation, although this is quite different from the results obtained for the heavier rare gas atom, Xe, in Chapter 4. By comparing our GGA-PBE calculated well depth with the value of 13 meV reported by Petersen *et al.* (1996), we find our result is closer to the experimental result (Parschau *et al.*, 1989).

In the case of Ne, there is no experimental information on the well depth for a clean Rh(110) surface, but we can obtain a rough estimate from results of a Rh surface covered with hydrogen, Rh(110)(1×2)H, with a coverage equal to 0.5 ML. (Table 5.3). By supposing that H atoms have a similar effect on Ne atoms as on He atoms, we can deduce that the potential well depth of Ne is around the value given by the GGA-PBE. Our result obtained with the GGA-PBE approximation is lower than the well depth value of 18 meV reported by Petersen *et al.* (1996).

5.3.1 Corrugation of the potential

We now turn to an analysis of the repulsive part of the potential curves in Figure 5.4. For high kinetic energies, it is expected that probe atoms penetrate deeper into the electron density therefore the corrugation amplitude of the potential should increase with an increment of the probe's kinetic energy. However in some cases it has been found that the corrugation amplitude remains constant or even decreases with an increase in the kinetic energy, (Rieder & García, 1982). Figure 5.5 shows the calculated corrugation amplitude of the interaction potential of He and Ne on Rh(110) as a function of the kinetic energy of the impinging particles. These curves were obtained from the fitting polynomial. This was done by calculating the potential difference between the bridge and on-top sites, using the on-top site as a reference point. Calculations were concentrated in the energy range between 20 meV and 200 meV, as this corresponds to the kinetic energy normally used in HAS techniques (Fariás & Rieder, 1998). All calculations were made using the results obtained with the GGA-PBE approximation.

In the case of He, the corrugation amplitude increases with kinetic energy at the long bridge site (i.e. perpendicular to the closed-packed row) reaching a maximum at around 100 meV and decreases for higher energy. This behaviour is similar to

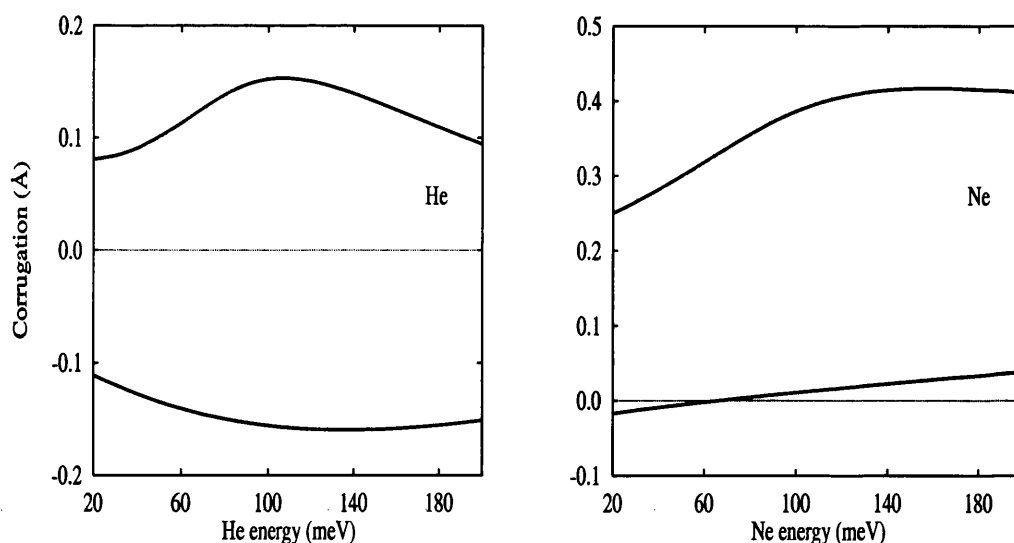


Figure 5.5: Corrugation amplitude of the potential for He (left) and Ne (right) atoms over the Rh(110) surface, using the GGA-PBE approximation. The blue line corresponds to the corrugation along the closed-packed rows while the red line corresponds to the perpendicular direction, see Figure 5.1.

that found by Rieder & García (1982) for He on Ni(110). At the short bridge site, we note that the potential is anticorrugated; the anticorrugation of the potential increases slowly with kinetic energy and becomes nearly constant at higher energies. In the case of Ne at the long bridge site, the corrugation grows linearly with energy until reaching a plateau around 140 meV. Along the closed-packed rows, the potential shows a very small anticorrugating effect which reverses as the kinetic energy is increased beyond 60 meV.

Making a comparison between He and Ne, we observe that the corrugation amplitude is larger in magnitude for Ne than for He, which is in agreement with experimental findings. Analyses of diffraction intensities from metal surfaces have shown that the interaction potential of Ne over a metal surface has a larger corrugation than for He (Lapujoulade & Perreau, 1983; Rieder & Stocker, 1984; Salanon, 1984; Parschau *et al.*, 1989). Table 5.4 shows that the measured Ne corrugation is up to twice that of He, which is in agreement with our results.

In the literature there is little information about the energy dependence of the

	He		Ne	
	ξ_{10} (Å)	ξ_{01} (Å)	ξ_{10} (Å)	ξ_{01} (Å)
Parschau <i>et al.</i> (1989)	+0.06	+0.15	-	+0.29
Rieder <i>et al.</i> (1993)	-0.06	+0.12	+0.04*	+0.15*
Petersen <i>et al.</i> (1996)	-0.04	-	+0.09*	-
present work	-	-	+0.01*	+0.27*
present work	-0.14	+0.18	-0.01	+0.32

Table 5.4: Comparison of amplitudes of corrugation from the interaction potential of He and Ne with Rh(110). ξ_{10} corresponds to the amplitude of corrugation parallel to the closed-packed rows and ξ_{01} to the perpendicular direction. Kinetic energy of the incoming atom is 64 meV except the values marked with an asterisk that correspond to 34 meV.

corrugation amplitude for He and/or Ne over Rh as a function of the kinetic energy of the probe atoms. However, a comparison can be made with specific kinetic energy values, see Table 5.4. We find that the amplitude of the corrugation perpendicular to the closed-packed rows is in better agreement than along the parallel direction when a comparison is made with the results given by Parschau *et al.* (1989). For He atoms with a kinetic energy of 64 meV, we find a value of +0.18 Å while for Ne with the same kinetic energy the corrugation amplitude is calculated to be +0.32 Å. For these cases, Parschau *et al.* (1989) have reported corrugation amplitudes of +0.15 Å and +0.29 Å respectively while Rieder *et al.* (1993) reported values of +0.12 Å and +0.15 Å respectively, but the result for Ne was obtained with a kinetic energy of 32 meV. For this energy, we have calculated a corrugation amplitude of +0.27 Å. Probably, the disagreement with the results of Rieder *et al.* (1993) is due to the fact that their measurement was performed for an H-covered surface.

Along the closed-packed rows, in the case of He, we find a corrugation amplitude of -0.14 Å which contrasts with the value of +0.06 Å given by Parschau *et al.* (1989) and overestimates the values of -0.06 Å and -0.04 Å given by Rieder *et al.* (1993) and Petersen *et al.* (1996) respectively. In the case of Ne, we obtain a value of -0.01 Å while Rieder *et al.* (1993) and Petersen *et al.* (1996) report +0.04 Å and +0.01 Å respectively.

5.4 Induced charge density

We have calculated the electronic charge density induced by He and Ne atoms over the on-top site of Rh(110) at three selected heights: at 5.0 Å, where the interaction is negligible, at the equilibrium height, and at the repulsive part of the potential for a turning point corresponding to a kinetic energy of 150 meV. The main reason to consider the latter with a strong interaction point is because for He and Ne the changes induced in the charge density at the equilibrium height are very small. Additionally, the kinetic energy of 150 meV was chosen in order to compare with the results given by Petersen *et al.* (1996).

In Figures 5.6 and 5.7 we present the electronic charge density induced by He

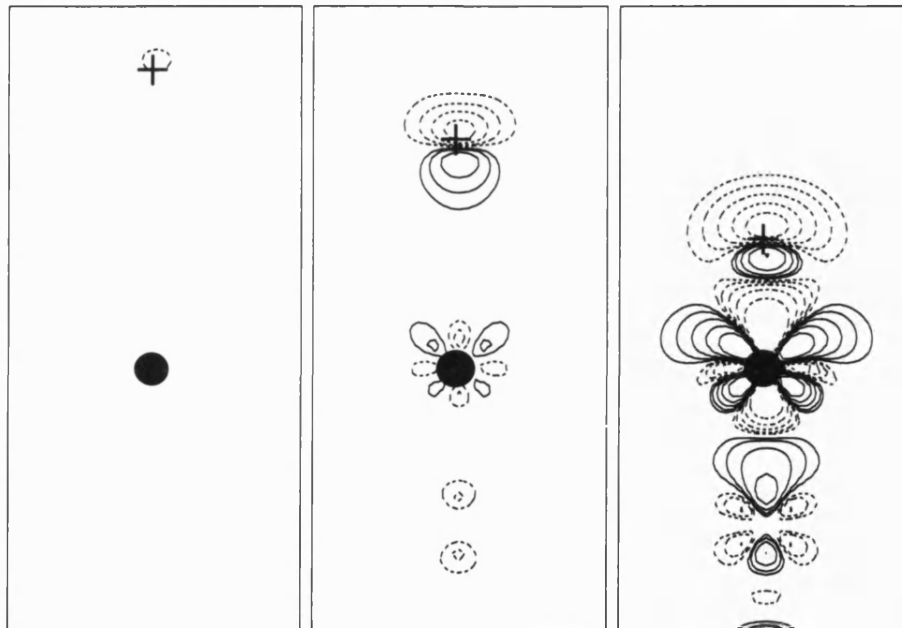


Figure 5.6: Electronic charge density difference induced by an He atom over the on-top site at three different heights from the topmost surface layer. The cut is along $[1\bar{1}0]$, see Figure 5.1. Left panel at 5.0 Å, middle panel at 3.75 Å (equilibrium height) and right panel at 2.16 Å (corresponds to a turning point of 150 meV). Positive values are shown by solid lines and negative values with dashed lines. Contour lines represent electronic charge densities given by $\pm 2^n \times 10^{-4} e \text{ \AA}^{-3}$ $n = 1, \dots, 5$, except for the right panel where each contour is multiplied by 10. The position of the He and Rh atoms are shown by the cross and bullet symbols respectively.

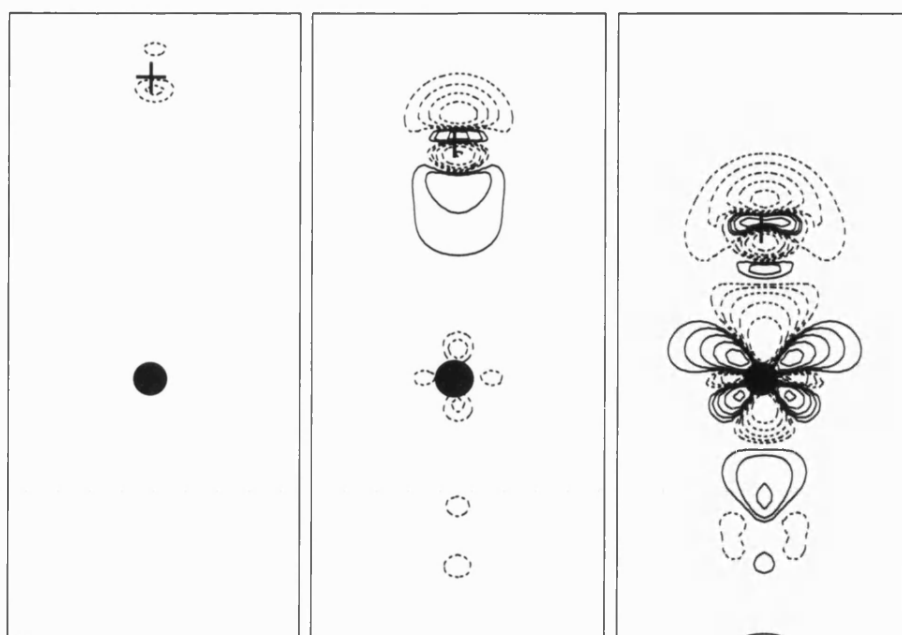


Figure 5.7: Electronic charge density difference induced by a Ne atom over the on-top site at three different heights from the topmost surface layer along $[1\bar{1}0]$, see Figure 5.1. Left panel at 5.0 Å, middle panel 3.61 Å (equilibrium height) and right panel at 2.51 Å (corresponds to a turning point of 150 meV). Positive values are shown by solid lines and negative values with dashed lines. Contour lines represent electronic charge densities given by $\pm 2^n \times 10^{-4} e \text{ \AA}^{-3}$ $n = 1, \dots, 5$, except for the right panel where each contour is multiplied by 10. The position of Ne and Rh atoms are shown by the cross and bullet symbols respectively.

and Ne on a Rh(110) surface. These results are those obtained with the GGA-PBE approximation. It can be observed that the interaction of He and Ne involves only a small change of the charge density at the equilibrium height, but at the selected turning point the changes are more noticeable. In general, we observed that each rare-gas atom produces a similar polarisation of the Rh surface but there are different polarisations on the atoms themselves. According to the calculated induced electronic charge density, it seems that the main change in the surface atoms takes place for d electrons.

In order to identify in more detail which orbitals are affected by the impinging atom, we have calculated the projected density of states, equation (2.62), for the Rh atom below the He and Ne atoms at the three above-mentioned positions. Only

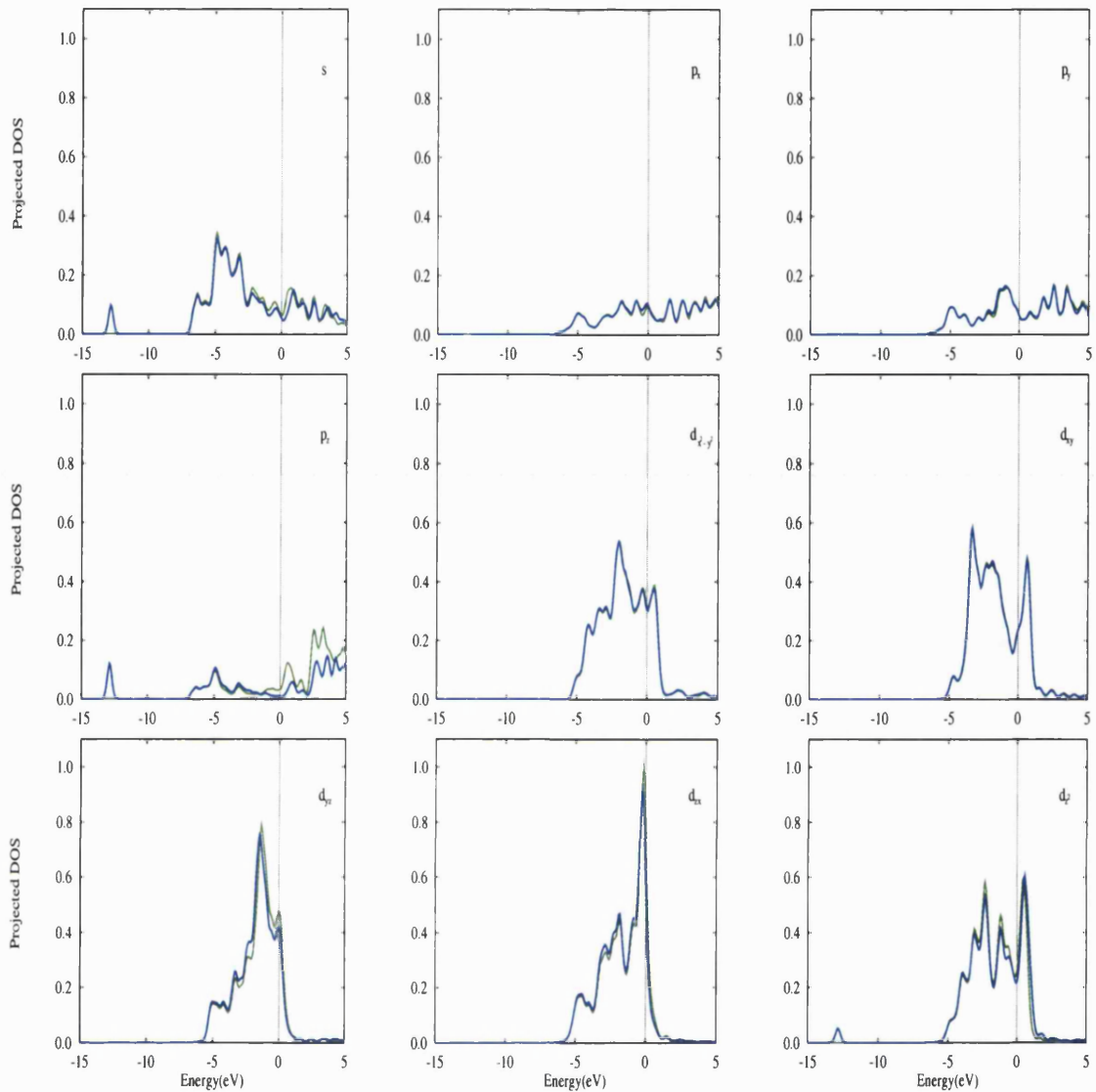


Figure 5.8: Projected density of states for $5s$, $5p$ and $4d$ for the Rh atom below the incoming He atom. Green line corresponds to a He atom placed at a height of 5.0 \AA , blue line corresponds to a turning point of 150 meV (He at a height of 2.16 \AA).

the projected densities of states for the interaction of the probe atoms located at a height of 5.0 \AA and the turning point corresponding to 150 meV are shown (Figure 5.8 and Figure 5.9) because there are no significant differences between the results for the height of 5.0 \AA and the equilibrium height.

In the case of He interaction, Figure 5.8, the projected densities of states shows that the main changes on the Rh surface take place on the $5s$, $5p_z$, $4d_{yz}$, $4d_{zx}$ and

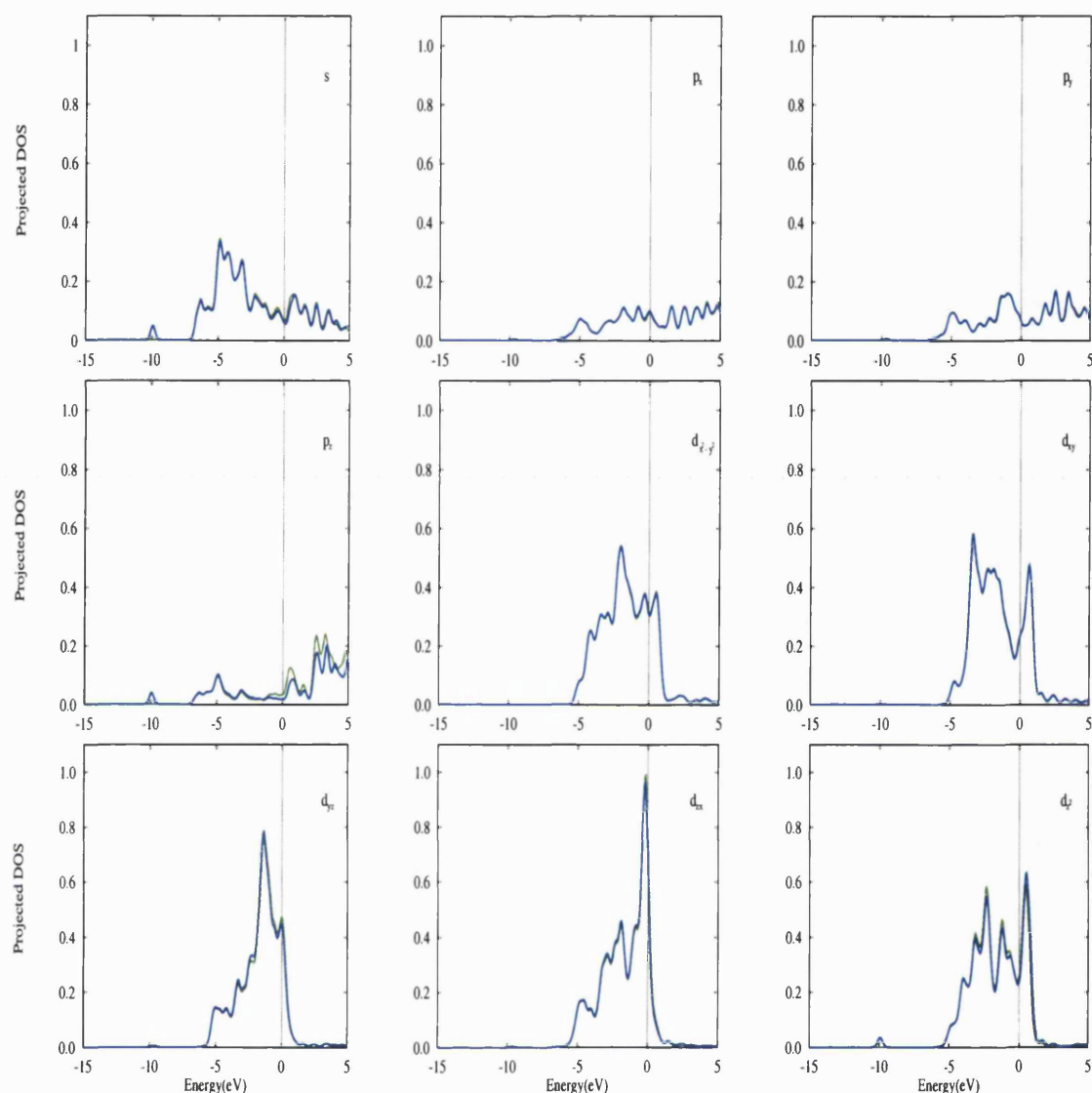


Figure 5.9: Projected density of states for $5s$, $5p$ and $4d$ for the Rh atom below the incoming Ne atom. Green line corresponds to a Ne atom placed at a height of 5.0 \AA , blue line corresponds to a turning point of 150 meV (Ne at a height of 2.51 \AA).

$4d_{z^2}$ orbitals. The interaction with the He $1s$ state (at about -13 eV , see Figure 5.10) can be observed on the $5s$, $5p_z$ and $4d_{z^2}$ orbitals.

In the case of Ne (Figure 5.9), we find results similar to those for He, but the interaction is with the Ne $2p$ orbitals (at about -10 eV , see Figure 5.10 left panel). There is a very small participation of Ne $2s$ (at about -32 eV , it is not shown) particularly with Rh $5s$ and the Rh $5p_z$ orbitals.

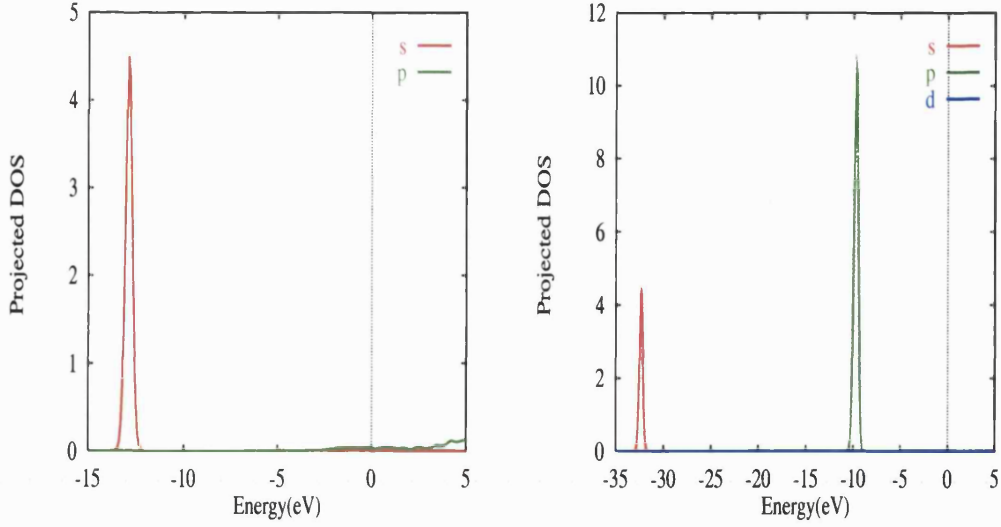


Figure 5.10: Projected density of states for He (left panel) and Ne (right panel).

By summing the projected density of states, we have calculated the charge associated with each orbital using equation (2.63). The change induced in each orbital was determined by taking the difference between the turning point corresponding to 150 meV and a reference position at 5.0 Å. In general, the change induced over the metal surface by both probe atoms was very small. Table 5.5 summarises the charge associated with the top layer Rh atoms for interaction with Ne and He at the on-top and short bridge sites.

For interaction at the on-top site, He and Ne produce an increase in the occupancy of the d_{yz} , d_{zx} and p_z orbitals with a decrease in the d_{z^2} orbital. This is in agreement with our qualitative description given by Figure 5.6 and Figure 5.7. Similar to the Xe/Pt system, we find that the total charge of the system is somewhat greater than the total number of electrons but such over-counting is compensated for by the plane wave charge component. The charge difference associated with all the

System	s	p_x	p_y	p_z	d_{xy}	d_{yz}	d_{zx}	$d_{x^2-y^2}$	d_{z^2}	Total
He/Rh (T)	-0.39	+0.13	+0.15	+0.65	+0.01	+0.33	+0.66	+0.05	-0.71	+0.88
Ne/Rh (T)	-0.21	+0.06	+0.06	+0.24	-0.02	+0.19	+0.33	+0.01	-0.49	+0.17
He/Rh (SB)	-0.15	+0.06	-0.01	+0.02	-0.04	+0.04	+0.11	-0.02	-0.06	-0.05
Ne/Rh (SB)	-0.08	+0.05	0.00	+0.05	-0.02	+0.06	+0.13	+0.01	-0.05	+0.15

Table 5.5: Difference of the charge in $10^{-1}e$ associated with the $5s$, $5p$ and $4d$ orbitals of the Rh atom at the on-top (T) and short bridge (SB) sites.

orbitals of He and Ne was less than the change in the charge associated with the plane wave component which makes it difficult to determine accurately the real induced charge on the probe atom. However, the larger change of occupancy of metal states occurs for He at the top site and for Ne at the short bridge site, which correlates with the lowest energy sites for both atoms (see Table 5.3).

5.5 Conclusions

The interaction of light rare-gas atoms (He and Ne) with Rh(110) has been calculated using first principles DFT calculations. The results show that the interaction potential energy obtained with the LDA is more attractive than that given by the GGA-PBE. In comparison with estimates of the potential well depth made with selective adsorption, the GGA-PBE is better for describing the interaction of He over the Rh(110) surface.

Both the LDA and GGA-PBE approximations show that the potential of He is anticorruagated. Although the results obtained with the GGA-PBE show a better correspondence with experiment still there are discrepancies with the amplitude of corrugation, especially with He along the closed-packed rows. Our calculations reproduce the anticorruagating effect observed experimentally for He, but still a large deviation from the results reported by Rieder *et al.* (1993) is found. On the other hand, along the direction perpendicular to the closed-packed rows, the calculated amplitude of corrugation is in good agreement with experiment, when a comparison is made with the results given by Parschau *et al.* (1989) for a clean Rh(110) surface.

We find that each probe atom induces a similar polarisation in the Rh surface but that each rare-gas atom suffers a different polarisation. Full analysis of the polar-

isation charge on the He and Ne was impossible to carry out using the projected density of states because the charge induced in each atom is smaller than the change in the plane wave component. However, we find in the case of He, its $1s$ orbital shows a strong interaction with Rh $5s$ and Rh $5p_z$ and a moderate interaction with Rh $4d_{z^2}$. In the case of Ne, the main contributions are given by the interaction of its $2p$ orbital with Rh $5s$ and Rh $4d_{z^2}$, and a moderate interaction with the Rh $5p_x$ and Rh $5p_y$ orbitals. In conclusion, these results suggest that the interaction with each rare-gas atom is defined by the changes in the electronic distribution of the substrate.

Chapter 6

Chemisorption of CO on the the Pt(110) surface

6.1 Introduction

Pt is one of the most widely used heterogeneous metal catalysts (Somorjai, 1994). The clean Pt(110) surface is a (2×1) reconstructed structure. The reconstruction is the so-called missing-row structure (see Figure 6.1) where every second atomic row along the $[1\bar{1}0]$ direction is missing in the top layer. X-ray diffraction (Vlieg & Robinson, 1990) and low energy electron diffraction (LEED) (Sowa *et al.*, 1988) reveal a surprisingly high contraction of about 0.3 Å in the top layer spacing and further relaxations in the deeper layers have been also observed, especially a pairing in the second layer and a buckling in the third layer.

An essential effect of CO adsorption on Pt(110) is that it can lift the reconstruction back to its bulk terminated (1×1) structure, depending on the adsorption temperature and coverage (Comrie & Lambert, 1976; Freyer *et al.*, 1986; Imbihl

et al., 1988). At low coverages the (2×1) reconstructed phase coexists with islands of CO on Pt (1×1) . As the coverage is increased, this phase transition is completed. Gritsch *et al.* (1989), using direct imaging by STM have claimed that the mechanism consists of an adsorbate-induced nucleation which breaks up the initial atomic configuration, followed by single atoms or even chains of atoms that move into free sites of the top layer. Additionally, the shape and the size distribution of the domains of the new phase depends on temperature. Schwegmann *et al.* (1995) have found evidence that the lifting of the (2×1) missing-row reconstruction begins with a remarkable change of the Pt substrate relaxation.

The main experimental information about CO-Pt surface bonding has been deduced from vibrational spectroscopy (Freyer *et al.*, 1986; Sharma *et al.*, 1998), but recently this technique has been shown to be oversimplified (Bradshaw, 1997) because a large shift observed in the C-O vibrational frequency as the coverage increases may be from dipole-dipole coupling and not from a change in the adsorption position. At low coverage, RAIRS (Reflection Absorption InfraRed Spectra) experiments (Bare *et al.*, 1984) show that CO is adsorbed at the on-top site while for high coverage, greater than 0.5 ML, the CO is adsorbed on a bridge site. On the other hand, different values of the initial heat of adsorption have been reported. The microcalorimetric experiment carried out by Wartnaby *et al.* (1996) determined a value of the initial heat of adsorption of 183 kJ mol^{-1} (1.90 eV), rather than the lower value of 150 kJ mol^{-1} (1.55 eV) reported by Fair & Madix (1980) and Engstrom & Weinberg (1988).

Few *ab-initio* calculations have been carried to model the CO/Pt(110) structure (Pacchioni *et al.*, 1997; Curulla *et al.*, 1999; Ge & King, 1999) and the majority of them use a cluster model to describe the adsorption. It is found that adsorption parameters are very sensitive to the surface cluster size. This situation encourages us to study the adsorption of CO on Pt(110) using a more realistic model to describe

the surface. We will concentrate on determining the equilibrium geometry structure and will calculate the distortion on the clean surface due to the adsorption a CO molecule. All the calculations were made at a relatively high coverage due to the excessively large computational effort required at lower coverages.

In this chapter we present results for CO chemisorption on both the unreconstructed and reconstructed Pt(110) surfaces at different coverages. We have selected coverages of 1 ML (monolayer) and 0.5 ML for the unreconstructed surface, and coverages of 0.5 (ML) and 0.25 (ML) for the reconstructed surface. For all cases studied, the relaxation of the Pt substrate due to the adsorption of CO molecules was considered. In general, this type of calculation is very demanding, particularly the determination of the equilibrium structure, because well-converged results for the atomic forces are required. Additionally, the elements that form the CO molecule present deep pseudopotentials and, even with optimised pseudopotential schemes, for instance Troullier & Martins' method (Troullier & Martins, 1990), the calculation of the equilibrium structure requires a heavy computational load. For this reason, we have used an ultrasoft pseudopotential method (see section 2.6) which provides a more efficient scheme to calculate the total energy for the CO/Pt system. Non-local corrections to the exchange-correlation functional in the form of the GGA have been used (Perdew & Wang, 1992).

The chapter is organised as follow: in section 6.2, we present computational details of the total energy calculation, together with results for the equilibrium geometry of the CO molecule and the relaxation of the missing row and unreconstructed Pt(110) surface. Chemisorption of CO on both the unreconstructed and missing row structure are treated in section 6.3, where we also discuss the distortion of the Pt substrate due to the adsorption of CO. Finally, the conclusions of the chapter are presented in section 6.4.

6.2 Computational details

All calculations were carried out using an ultrasoft pseudopotential scheme (see section 2.6) with the CASTEP package (an acronym for CAMbride Sequential Total Energy Package). Electronic relaxation was reached by using Pulay's density mixing scheme. The integration over the Brillouin zone was made by using a symmetrised Monkhorst-Pack mesh and a Fermi smearing of 0.2 eV was used. The force on the atoms are calculated according to the Hellman-Feymann theorem (Grosso & Parravicini, 2000). Exchange-correlation effects were described by the GGA-PW91 (Perdew & Wang, 1992).

6.2.1 CO molecule

Previous studies have showed that the GGA approximation is more reliable than the LDA for describing the bond of a CO molecule (Hu *et al.*, 1994; Hammer *et al.*, 1996). In order to verify this statement, we have compared results obtained with the LDA and GGA. Calculations were performed for a CO molecule in a box of size $10 \text{ \AA} \times 10 \text{ \AA} \times 15 \text{ \AA}$ and sampling the Brillouin zone with $2 \times 2 \times 1$ k-points. The Kohn-Sham eigenfunctions were expanded with a plane wave basis set with an energy cut-off of 380 eV. The equilibrium bond length was calculated by relaxing the molecular coordinate until the force was less than 0.01 eV/\AA . In contrast to rare-gas dimers, the CO bond length was not sensitive to the exchange-correlation approximation used. We found bond lengths of 1.144 \AA and 1.146 \AA with the LDA and GGA respectively. However, a significant difference was found in the binding energy, 12.5 eV with the LDA and 11.2 eV with the GGA. The GGA value is in better agreement with the experimental result of 11.1 eV (Huber & Herzberg, 1979) and with the value of 10.9 eV given by Hammer *et al.* (1996) using the LMTO

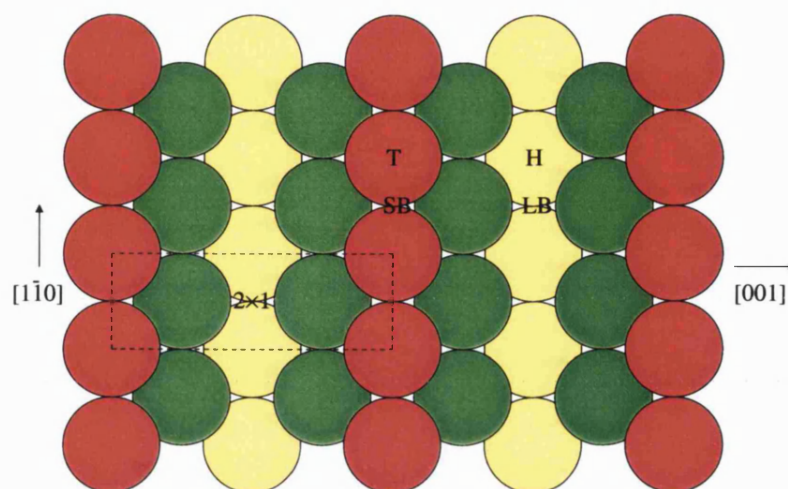


Figure 6.1: Top view of a fcc(110) (2×1) missing row structure and its high symmetry sites. The red circles represent the top layer of atoms, the green circles the second layer and the yellow circles the third. T: atop site, SB: short bridge site, LB: long bridge site and H: four-fold hollow site.

(linear muffin tin orbital) method.

6.2.2 Missing row and unreconstructed (110) surface

Before studying the interaction of the CO molecule on the Pt surface we have calculated the equilibrium geometry of the substrate. These calculations were made for both the missing row and unreconstructed (110) surfaces. In the case of the missing row structure, the surface was represented by a (2×1) structure (see Figure 6.1) with slabs consisting of seven atomic layers separated by a vacuum gap equivalent to another seven layers (≈ 10 Å). The equilibrium structure was determined by allowing the relaxation of the atomic coordinates for the first four layers while the remaining layers were fixed at their equilibrium bulk position. The GGA-PW91 lattice constant calculated with ultrasoft pseudopotentials was 3.97 Å. The cut-off energy was fixed at 180 eV and the Brillouin zone was sampled with

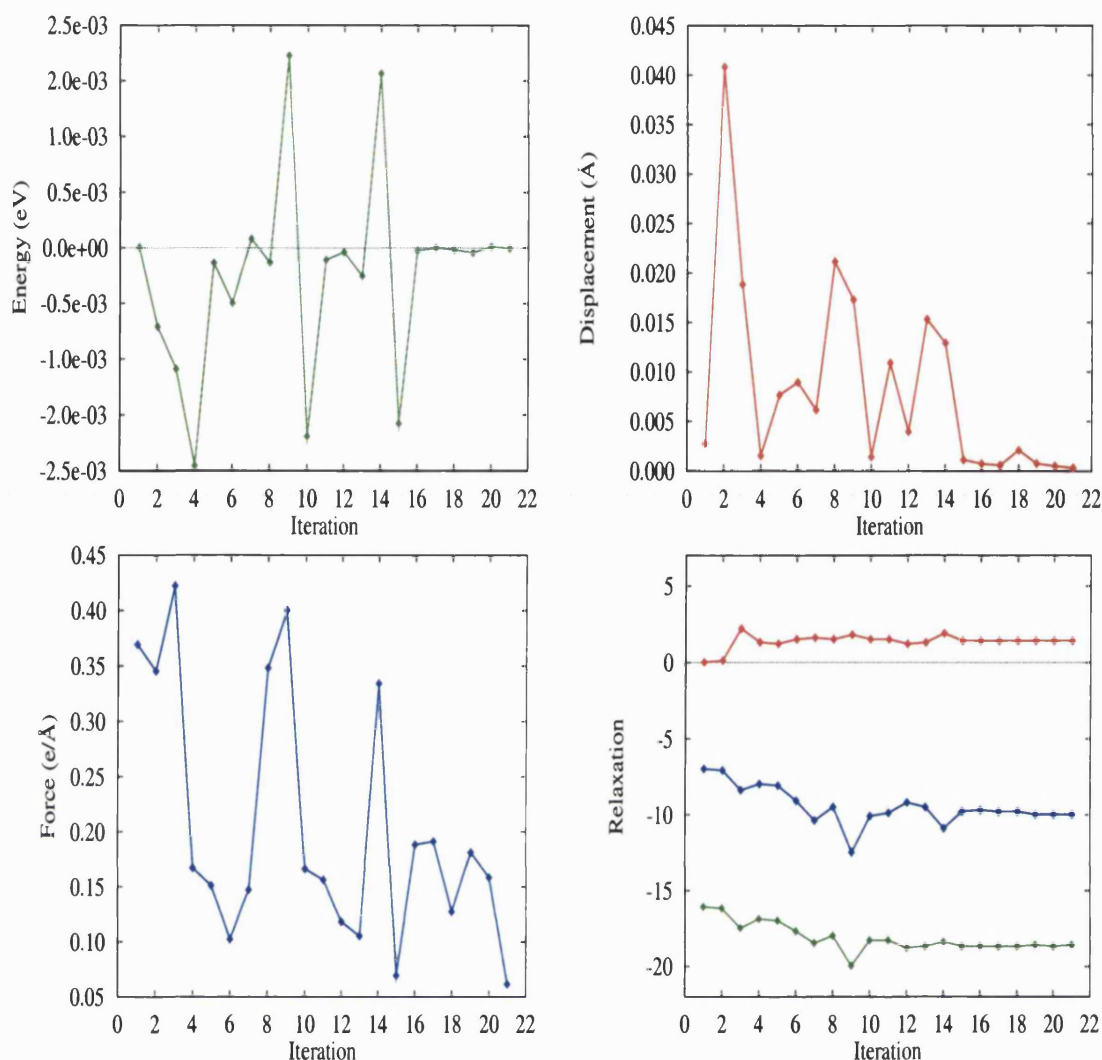


Figure 6.2: Convergence of the total energy (top left), displacement (top right), force on the movable atoms (bottom left), and the contraction/expansion of the separation of three subsequent atomic layers (bottom right) for the Pt(110) missing row structures. For the bottom right panel, green line: contraction of the first atomic layer; blue line: contraction of the second layer and red line: expansion of the third layer. The relaxation was defined as the percentage distortion of the layer divided by the bulk interlayer spacing.

a by 4×12 Monkhorst-Pack mesh (i.e. 12 \mathbf{k} -points in the irreducible wedge).

The iterative procedure was stopped when an error of 1.0×10^{-5} eV in the total energy was reached and the average displacement and force of the movable atoms reached values of 0.005 \AA and 0.1 e/\AA respectively. We have found that with these values the geometry relaxation is well-converged, see Figure 6.2. Note that

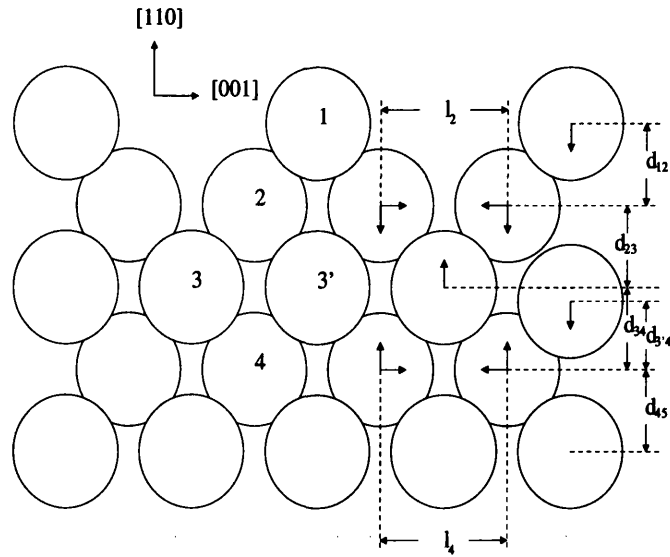


Figure 6.3: Relaxed missing row structure of Pt(110). d_{ij} represents the perpendicular distance between the atoms i and j and l_i is the lateral distance between two equivalent atoms in the same layer. $d_{12} = 1.145 \text{ \AA}$, $d_{23} = 1.268 \text{ \AA}$, $d_{3'4} = 1.223 \text{ \AA}$, $d_{34} = 1.515 \text{ \AA}$, $d_{45} = 1.420 \text{ \AA}$, $l_2 = 4.032 \text{ \AA}$ and $l_4 = 4.117 \text{ \AA}$. The atoms move in the direction indicated by the arrows.

for the first iterations there is an important variation in the total energy, force and displacement which is clearly reflected in the relaxation of the first (green line) and second (blue line) atomic layers. From the sixteenth iteration, a stabilisation of the structural parameters was reached, except for the atomic forces which are sensitive to small changes in the atomic displacements. The calculated equilibrium geometry shows that the separation between the first and second layers is 1.145 \AA , that corresponds to a contraction of -0.26 \AA with respect to the bulk value of 1.405 \AA , (see Figure 6.3). Atoms in the second layers relax inwards by -0.137 \AA and also suffer a lateral displacement of -0.057 \AA with respect to the bulk value of 3.974 \AA . The third atomic layer is buckled, atoms in this layer show separations of 1.223 \AA and 1.515 \AA , which correspond to relaxations of -0.182 \AA and $+0.110 \text{ \AA}$ respectively. For the fourth layer, the lateral displacement was determined to be -0.071 \AA and it relaxes outwards by 0.015 \AA . In general, our results reproduce experimentally observed features of a missing-row structure; a large inward relaxation of the top two layers, row-pairing in the second layer and buckling in the third layer. We find a good agreement with results from experiment

	Δd_{12} (Å)	Δd_{23} (Å)	p_2 (Å)	p_4 (Å)	b_3 (Å)
This work	-0.26	-0.14	0.06	0.07	0.29
X-ray diffraction ^a	-0.27	-0.11	0.05	0.04	-
LEED ^b	-0.26	-0.18	0.07	0.12	0.32
MEIS ^c	-0.22	0.06	0.04	-	0.10
Embedded method ^d	-0.25	-0.07	0.05	0.08	0.11

^a From Vlieg & Robinson (1990).

^b From Sowa *et al.* (1988).

^c Medium-energy ion scattering (MEIS) from Fenter & Gustafsson (1988).

^d From Foiles (1987).

Table 6.1: Distortions of atomic positions for the Pt(110) (2×1) missing row structure. Δd_{ij} is the change in the layer spacing between the i th and j th layers, p_i represents pairing in layer i and b_3 represents buckling in the third layer.

and previous theoretical work, see Table 6.1.

For the unreconstructed Pt(110) surface, the equilibrium geometry was calculated for a (1×1) structure (see Figure 6.4). The surface was represented by seven atomic layers separated by a vacuum gap equivalent to another seven layers. The cut-off energy was equal to that used in the case of the missing row structure (180 eV) but the Brillouin zone was sampling with 8×12 Monkhorst-Pack mesh (24 k-points in the irreducible wedge). The equilibrium geometry was calculated by allowing the relaxation of atomic coordinates for the first three layers and the remaining layers were kept fixed. The iterative process was stopped when the total energy, force and atomic displacement reached the same error as in the case of the missing row structure. The equilibrium separation for the top layers was calculated to be $d_{12} = 1.195$ Å, $d_{23} = 1.521$ Å, and $d_{34} = 1.385$ Å. This represents distortions relative to the bulk lattice of -0.21 Å, $+0.12$ Å, and -0.02 Å (or -14.9 %, $+8.3$ % and -1.5 %) respectively. Due to the fact that the unreconstructed Pt(110) is unstable, there are no experimental results for the structural parameters. However a comparison with theoretical calculations of Ge *et al.* (1999) can be made. They used the GGA with norm-conserving pseudopotentials and calculated the distortion of the first and the second layers to be -14.7 % and $+6.6$ % respectively. Although

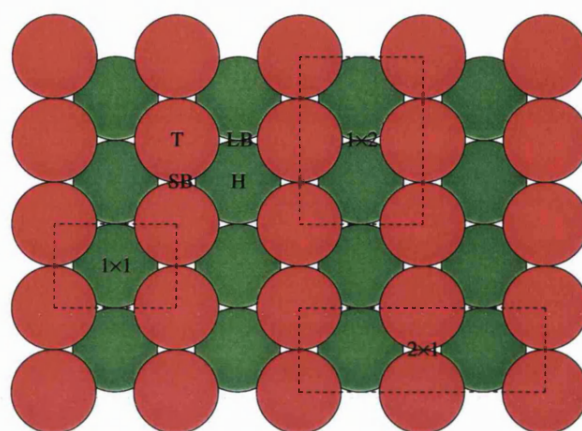


Figure 6.4: Top view of a fcc(110) unreconstructed surface and its high symmetric sites. The red circles represent the first layer of atoms and the green circles the second one. T: atop site, SB: short bridge site, LB: long bridge site and H: four hollow site.

Ge *et al.* also used seven atomic layers, they allowed the relaxation of only the two first layers, which could explain the smaller distortion they found for the second layer.

6.3 Chemisorption of CO

At the high symmetry sites and for selected coverages of CO, we have calculated the binding energy, C-O bond length, C-Pt bond length and the substrate reconstruction for the adsorption of CO molecules on clean Pt(110) surfaces. Two surfaces of Pt(110) were selected; an unreconstructed structure with coverages of 1.0 ML and 0.5 ML and a missing-row structure with coverages of 0.5 ML and 0.25 ML. All calculations were made using a cut-off energy of 380 eV and the GGA-PW91 approximation for the exchange-correlation energy.

The binding energy was calculated using

$$E_b = - \left(\frac{E_{CO+Pt(110)} - E_{Pt(110)} - N_{CO} \times E_{CO}}{N_{CO}} \right), \quad (6.1)$$

where $E_{CO+Pt(110)}$ is the total energy of Pt(110) slab with adsorbed CO molecules, $E_{Pt(110)}$ is the total energy of a bare slab of Pt(110) with its topmost layer relaxed (so that the binding energy includes substrate relaxation), E_{CO} is the total energy of a free CO molecule and N_{CO} is the number of CO molecules per supercell. The energy of an isolated CO molecule was calculated in a $(10 \text{ \AA})^3$ box with the same cut-off energy as for the slab calculations and sampling the Brillouin zone with a $2 \times 2 \times 2$ Monkhorst-Pack mesh.

For all the cases studied, two situations were considered for CO adsorption on the Pt(110) substrate. First, all the Pt atoms were kept at their relaxed, clean-substrate positions. In the second case a full relaxation of the Pt substrate was allowed. In the case of the missing row structure, relaxations of the first four layers were allowed while for the unreconstructed structure the first three layers were allowed to relax. For all calculations of the distortion or relaxation of the substrate due to the CO adsorption were calculated using the clean relaxed surface as a reference.

6.3.1 Adsorption at the unreconstructed surface

Table 6.2 summaries binding energies, C-O bond lengths and the C-Pt bond lengths corresponding to the adsorption of CO molecule on an unreconstructed Pt(110) surface. These calculations were made for coverages of 1 ML and 0.5 ML. The supercell consisted of seven Pt layer slabs separated by a vacuum gap ($\approx 14 \text{ \AA}$) equivalent to nine layers. The Brillouin zones of the (1×1) , (2×1) and (1×2)

	site	E_b (eV)	d_{CO} (Å)	d_{PtC} (Å)
1.0 ML	T	1.881 (1.818)	1.157 (1.156)	1.857 (1.859)
	SB	1.956 (1.808)	1.171 (1.170)	2.033 (2.041)
	LB	0.887 (0.778)	1.175 (1.174)	2.275 (2.260)
	H	-0.107 (-0.137)	1.153 (1.152)	3.011 (3.060)
	T	1.907 (1.843)	1.156 (1.156)	1.853 (1.854)
	SB	2.002 (1.824)	1.173 (1.172)	2.027 (2.041)
0.5 ML	LB	1.582 (0.977)	1.183 (1.185)	2.051 (2.189)
	H	-0.079 (-0.121)	1.153 (1.152)	2.993 (3.061)
	T	2.166 (2.078)	1.156 (1.158)	1.851 (1.852)
	SB	2.231 (2.107)	1.176 (1.176)	2.001 (2.024)
0.5 ML	LB	1.163 (0.957)	1.180 (1.174)	2.821 (2.811)
	H	0.743 (0.645)	1.179 (1.180)	2.585 (2.561)

Table 6.2: Calculated adsorption properties of CO chemisorbed on the unreconstructed Pt (110) surface. Numbers in parentheses refer to calculations with substrate atoms fixed at their clean surface relaxed positions. The CO molecule is upright on the surface with the C end down. E_b denotes the binding energy, d_{CO} represents the C-O bond length and d_{PtC} denotes the C-Pt bond length, that is measured from the nearest Pt atom underneath the C atom (see Figure 6.5).

structures (see Figure 6.4) were sampling with 8×12 , 4×12 , and 8×6 Monkhorst-Pack meshes respectively. The lateral CO-CO energy is found to be +133 meV, +137 meV and +10 meV for the (1×1), (2×1) and (1×2) structures respectively.

For a coverage of 1 ML and assuming a static substrate, the on-top site becomes the most favourable adsorption site, but when the relaxation of the substrate is allowed, the short bridge site is preferred with an energy difference of 75 meV. On the other hand, the substrate relaxation does not induce significant changes in the

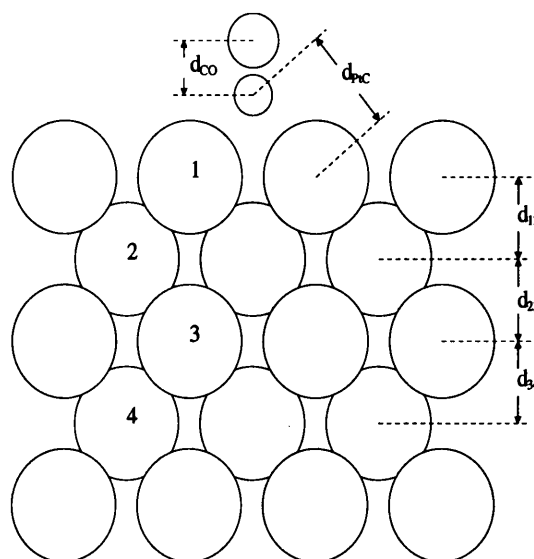


Figure 6.5: Side view of stationary Pt (2×1) substrate and the CO adsorbate. d_{CO} is the distance between C and O, d_{PtC} denotes the distance between Pt and C.

bond lengths. In both cases (static or relaxed substrate), the CO cannot bind at the hollow site, due to the large lateral interaction energy present in the binding energy.

For the case of a 0.5 ML coverage, we have considered both the (2×1) and (1×2) structures (see Figure 6.4). The latter structure reduces by more than 120 meV the lateral interaction between CO molecules, which allows us to determine whether the lateral forces affect the adsorption site. It was observed that the binding energies at the long bridge show a large difference when a comparison is made between relaxed and inert substrates. We found a difference of about 0.6 eV with the (2×1) structure and 0.2 eV with (1×2) structure, which indicates that an important reconstruction occurs in the substrate due to the adsorption of the CO molecule. For these cases, we have calculated the reconstruction of the Pt substrate with respect to the relaxed clean surface (see Figure 6.6). For the (2×1) structure (see Figure 6.6, top), we find that the atoms of the first layer relax outward approximately 0.24 Å and also

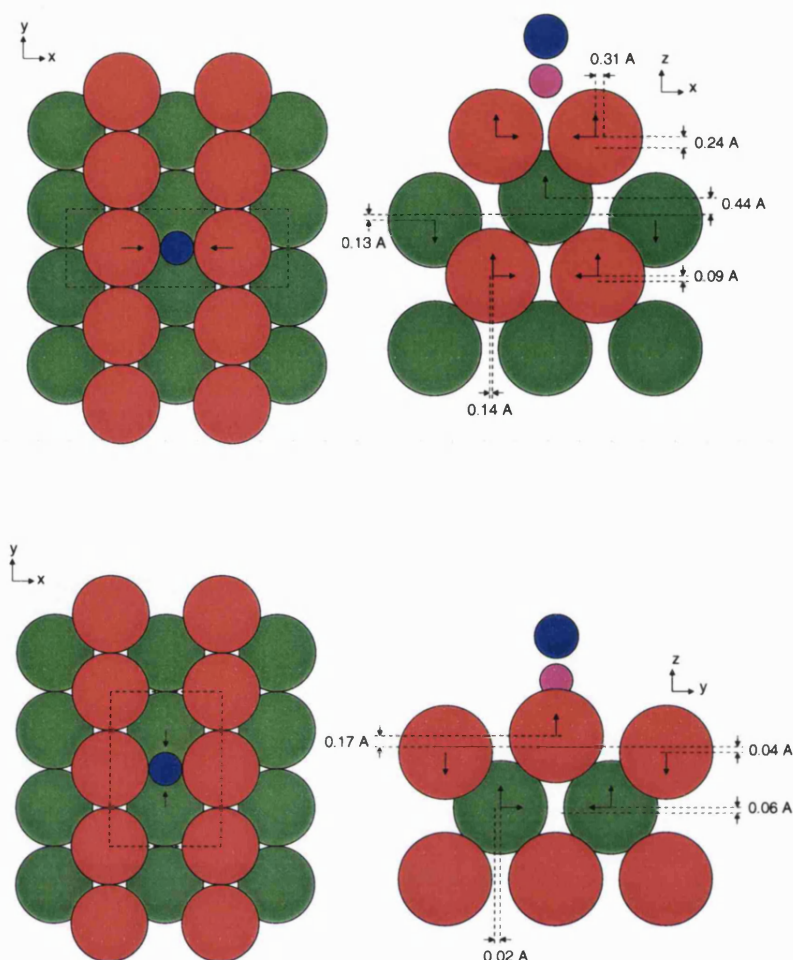


Figure 6.6: A schematic diagram of the relaxation of the Pt(110) unreconstructed surfaces ((2×1) structure top and (1×2) structure bottom) when a CO molecule is adsorbed at the long bridge site. The atoms move in the direction indicated by the arrows.

move a distance of 0.31 Å in the lateral direction (x axis). The positions of the Pt atoms in the second layer also suffer important distortions, particularly the Pt atom located below the CO, that moves a distance of 0.44 Å. This could be explained as a consequence of the increase in the number of coordinations, each one this Pt atom feels the interaction of two CO molecules. In the case of the (1×2) structure (see Figure 6.6, bottom), we find a more moderate distortion in comparison with the (2×1) case. The most important distortion occurs for the Pt atom below of C, this relaxes outwards by 0.17 Å.

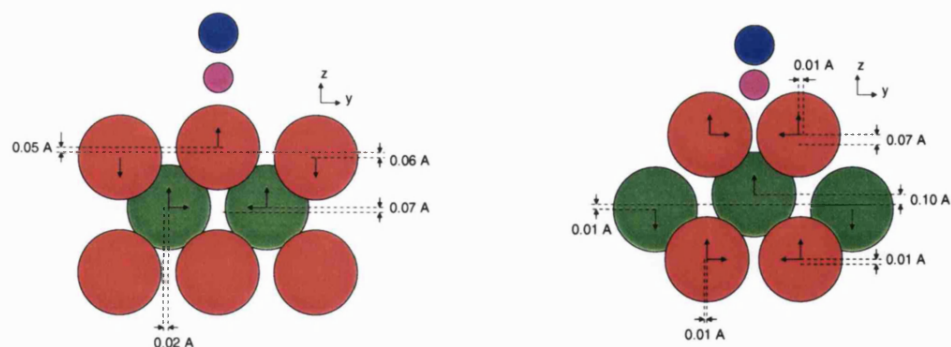


Figure 6.7: A schematic diagram of the relaxation of the Pt(110) unreconstructed surface (1×2) when a CO molecule is adsorbed at the top site (left) and short bridge site (right). The atoms move in the direction indicated by the arrows.

Similar to 1 ML case, for a coverage of 0.5 ML, the short bridge site remains the most favourable adsorption site. Also we find that the CO does not bind at the hollow site with a (2×1) structure but with the (1×2) structure it does. This a consequence of the large lateral energy which is substantially reduced with the (1×2) structure.

In the case of the (1×2) surface and considering the most stable sites (on top site and short bridge site), we found that the substrate suffers a small distortion in comparison with the distortions calculated for the long bridge (see Figure 6.7). The relaxation decreases the energy by 88 meV and 124 meV at the on top site and short bridge site respectively. When CO is adsorbed at the on top site, we find that the Pt below the CO relaxes outwards by approximately 0.05 Å while the neighbouring Pt in the same layer relaxes inwards by 0.06 Å. The atoms in the second layer relax outward by 0.07 Å with a small lateral distortion of 0.02 Å.

Decreasing the CO coverage from 1.0 to 0.5 ML, the binding energy at the short-bridge site increases by 46 meV for the case of the (2×1) structure and 275 meV for the (1×2) structure, indicating an important effect of the lateral repulsive interaction on the binding energy. Also we find that the diffusion barrier between the bridge and on-top sites decreases from 95 meV for the (2×1) structure to 65

		E_b (eV)	d_{CO} (Å)	d_{PtC} (Å)
top	from Pacchioni <i>et al.</i> (1997)	1.46	1.16	1.87
	from Curulla <i>et al.</i> (1999)	1.555	1.155	1.863
	from Ge & King (1999)	2.153	1.157	1.847
	present work	2.166	1.156	1.851
bridge	from Pacchioni <i>et al.</i> (1997)	1.30	1.18	2.02
	from Curulla <i>et al.</i> (1999)	0.705	1.179	2.008
	from Ge & King (1999)	2.129	1.173	2.005
	present work	2.231	1.176	2.001
experiment	from Wartnaby <i>et al.</i> (1996)	1.51	-	-

Table 6.3: Comparison of adsorption properties: binding energy, E_b , C-O bond length, d_{CO} , and C-Pt bond length, d_{PtC} , for CO chemisorbed on the Pt (110) unreconstructed surface at a coverage of 0.5 ML.

meV for the (1×2) structure. On the other hand, the calculations made with (1×2) structure do not show a site-switching from bridge to on-top, i.e., CO in bridge site is still the most energetically most favourable.

Table 6.3 shows a comparison of our results with previous results. In general it is observed that there is a very good agreement with the values of the bond lengths, but large differences in the binding energies. Our estimations of binding energies are higher than those reported by Pacchioni *et al.* (1997) and Curulla *et al.* (1999) using a cluster model and the experimental value of 1.51 eV given by Wartnaby *et al.* (1996) but is in good agreement with the results reported by Ge & King (1999). Although the value of 1.555 eV is in good agreement with experiment, this corresponds to the adsorption at the top, which is in contrast with the experimental fact that for coverage of 0.5 ML the adsorption of CO occurs at short bridge (Bare *et al.*, 1984).

6.3.2 Adsorption at the missing-row surface

Table 6.4 summaries the binding energy and the geometrical parameters of the CO molecule for adsorption at the missing-row surface for coverages of 0.5 ML and

	site	E_b (eV)	d_{CO} (Å)	d_{PtC} (Å)
0.5 ML	T	1.694	1.156	1.866
		(1.650)	(1.156)	(1.877)
	SB	1.857	1.171	2.024
	(2×1)	(1.599)	(1.170)	(2.019)
	LB	1.598	1.183	2.037
		(0.843)	(1.175)	(2.711)
0.25 ML	H	-0.194	1.150	3.131
		(-0.286)	(1.147)	(3.249)
	T	1.955	1.152	1.864
		(1.897)	(1.155)	(1.855)
	SB	2.054	1.177	2.005
	(2×2)	(1.962)	(1.178)	(2.013)
	LB	1.872	1.184	1.876
	H	0.084	1.148	4.084

Table 6.4: Calculated adsorption properties (binding energy, C-O bond length and C-Pt bond length) of CO chemisorbed on the Pt (110) missing row surface. Numbers in parentheses refer to an unrelaxed Pt substrate.

0.25 ML. The Brillouin zone of the (2×1) and (2×2) structures were sampled with 4×12 and 4×6 Monkhorst-Pack meshes respectively. The CO-CO lateral energy for the (2×2) structure is found to be less than 1 meV.

For a coverage of 0.5 ML, we found that binding energies are lower than those energies obtained with the unreconstructed surface. The short bridge site is again the most favourable adsorption place. The diffusion barrier between the short bridge and the on-top sites was calculated to be 163 meV, a value larger than that calculated for the unreconstructed structure.

Similar to the (2×1) unreconstructed structure, we find a large difference between the binding energy for frozen substrate and a fully relaxed one. Again, this seems to be due to large distortion in the second atomic layer (see Figure 6.8). This produces a significant shift in the atomic positions, where the atoms (second layer) relax outwards by approximately 0.2 Å and suffer a lateral distortion of nearly 0.3 Å with respect to the clean relaxed surface. Also we find a significant change in the binding energy due to the reconstruction of the substrate for adsorption at the

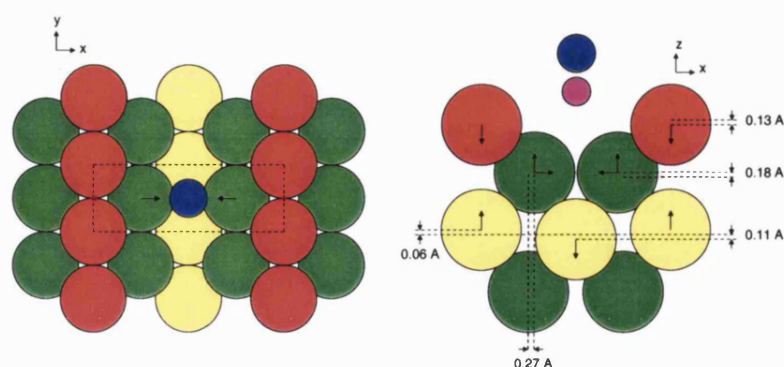


Figure 6.8: A schematic diagram of the relaxation of the Pt(110) (2×1) missing row structure when a CO molecule is adsorbed at the long bridge site.

short bridge site. The relaxation increases the binding energy by approximately 258 meV. Here, we find Pt atoms in the top layer move towards the C atom by 0.18 Å, while the Pt atoms in the second layer relax inwards only by 0.01 Å, and suffer a lateral distortion of 0.07 Å. In the case of the on-top site, the reconstruction only reduces the energy by 44 meV. Here the distortion of the substrate is small, the Pt atoms in the first layer relax outwards by 0.04 Å and the atoms of the second layer move towards the topmost layer by 0.03 Å with a small lateral distortion of 0.01 Å.

In the case of 0.25 ML coverage, we find a similar behaviour to the previous cases, with the short bridge site still preferred as the adsorption site with an energy barrier to the top site of 99 meV. Here we only calculated the effect of the substrate relaxation for the on-top and short bridge sites. In these cases, we find that the reconstruction increases the binding energy by 58 meV and 92 meV for adsorption at the on-top and short bridge sites respectively. When CO is adsorbed at the top site, the Pt atom below the C atom moves 0.05 Å while the Pt atom in the next layer relaxes inwards by 0.09 Å and laterally by 0.04 Å. In the case of the short bridge site the Pt atom in the first layer relaxes outwards by 0.17 Å while the Pt in

the second layer relaxes inwards and laterally by 0.05 Å and 0.04 Å respectively.

When we compare results obtained with structures with a lower lateral interaction potential (i.e. the (1×2) structure for the unreconstructed surface and the (2×2) missing-row structure), we find that the relaxation induces a change in the binding energy of about 100 meV for adsorption at the most favourable sites (on-top and short bridge sites). For both cases, we find a larger relaxation at the short bridge site which is due to the increased coordination of the topmost Pt atoms. On the other hand, the relaxations of these Pt atoms are quite similar for both structures.

By comparing the (2×1) and (2×2) missing row structures (see Table 6.4), we find a difference in the binding energy for the on-top, short bridge and long bridge sites of 0.261 eV, 0.197 eV and 0.274 eV respectively. The difference between CO-CO repulsion energy for these cells is 0.137 eV, which implies a significant extra repulsion energy due to the substrate. On the other hand, according to the results obtained for both the unreconstructed and missing row surface (Table 6.2 and Table 6.4), the general trend is that CO adsorption on the unreconstructed surface is more energetically favourable than on the missing row structure. This suggests an explanation for the adsorbate-induced reconstruction from a missing row to a bulk terminated structure as the CO coverage is increased. It is important to point out that our results show that for low coverage the CO adsorption still takes place at the short bridge, which contrasts with the experimental fact that for a coverage less than 0.2 ML the on-top site is the more favourable adsorption site. We note that several cases have been reported for CO adsorption on metal surfaces where the preferred adsorption site obtained by DFT calculations differs from experiment, for a recent review see Feibelman *et al.* (2000).

6.4 Conclusions

Using ultrasoft pseudopotentials and the GGA we have calculated the adsorption parameters for CO molecules binding to Pt(110) surfaces. Two possible surface structures were considered: an unreconstructed (110) surface and a missing row structure. The study was limited to relatively high coverages.

For both structures (unreconstructed and reconstructed) the short bridge is the most stable adsorption site for CO on Pt(110), but the largest binding energy was found to be for the unreconstructed structure. The atop site is the next most stable site, followed by the long-bridge site and the hollow site. Our binding energy is larger than those reported by experiment and previous theoretical estimations (Engstrom & Weinberg, 1988; Wartnaby *et al.*, 1996; Curulla *et al.*, 1999) using a cluster scheme but is in good agreement with similar *ab initio* calculations (Ge & King, 1999).

For the unreconstructed structure and a coverage of 0.5 ML, the energy difference between the bridge and on-top sites is approximately 95 meV for the (2×1) and 65 meV for the (1×2) structure, indicated a small barrier for CO diffusion.

CO adsorption induces significant changes in the substrate. Relaxations are different for each adsorption site. In general, CO tends to expand the layer spacing, back towards the value for bulk Pt. At the long bridge a large expansion of the second layer occurs with significant changes in the third, which explains the very large change observed in the binding energy. In the cases of adsorption at the on-top and short bridge sites, the relaxation leads to a smaller change in the binding energy and the main structural changes occur in the two first layers.

For the missing-row structures studied, the binding energies obtained are smaller

than those calculated for the unreconstructed structures. However, we find that the short bridge is the most favourable adsorption site for the CO molecule and a there is larger diffusion barrier than that calculated for the unreconstructed surface.

Chapter 7

Conclusions

The interaction of the systems Xe/Pt(111), He/Rh(110), Ne/Rh(110) and CO/Pt(110) have been treated using first principles total energy calculations and *ab-initio* pseudopotentials. Before studying the above-named systems, we have carefully tested the pseudopotentials constructed for the elements He, Ne, Cu, Rh, Pt and Xe, evaluating equilibrium structural properties for their crystalline or molecular form. A good agreement was found with all-electron calculations and experimental results. The key point of the pseudopotential construction procedure consisted of the optimisation of the core radius through the logarithmic derivatives. With such a procedure, we can balance the high transferability due to a small radius and the lower cut-off energy of a large core radius. However, the optimisation of those pseudopotential components without the same component present in the core was not possible. This was the case of $1s$ for He, $2p$ for Ne and $3d$ for Cu. In these cases the selection of the core radii was made by taking into account the best reproduction of the equilibrium structural properties.

The exchange-correlation energy was approximated by the LDA and GGA and the effect of both approximations on the structural properties was determined. Both

were included in the pseudopotential construction procedure and all calculations were made in a self-consistent manner. The equivalence of the GGA-PW91 and GGA-PBE functionals was confirmed. It was also found that oscillations introduced by the GGA-PW91 are substantially reduced with the GGA-PBE. Additionally, an improvement of the transferability of the pseudopotentials was made by the incorporation of core-valence exchange-correlation corrections. For the elements Xe, Pt and Rh, the improvements obtained on the structural properties were small. However, a substantial improvement on the quality of the pseudopotentials constructed with GGA was obtained with the core-valence exchange-correlation correction, which completely removed the oscillations. In the cases of He and Ne, we found that the structural properties of their dimers were better described by the GGA approximation although the binding energies are still overestimated, however our results are in good agreement with all-electron calculations. For Xe neither the LDA nor GGA gave a complete description of the bonding, with the binding energy showing a large deviation from the experimental result.

For the system Xe/Pt(111) we have found that the LDA provides adsorption parameters (binding energy, equilibrium adsorption height and vibrational energy) are in reasonably good agreement with experimental results. On the other hand, the GGA approximation gives a very weak binding. The two approximations also show an important difference in the repulsive part of the potential, predicting a difference in the turning point of almost 0.5 Å for a kinetic energy of about 100 meV. Additionally, both approximations predict that the on-top site is the most favourable adsorption site. Calculations of the projected density of states show that there is an important level of chemisorption. The calculated work function change is greater (−1.27 eV) than the value measured using angle-resolved photoemission (−0.6 eV); this discrepancy seems to be a consequence of the overbinding of the LDA.

In contrast with the results obtained for Xe/Pt(111), the interaction of He and Ne on Rh(110) was better described with the GGA approximation. Both the LDA and GGA show that the potential for He is anticorrugated, with the corrugation amplitude of the potential calculated for Ne being in better agreement with the experimental results than for He. Due to the small change of the polarisation charge and the large change of the charge associated with plane wave component, a full analysis of the polarisation could not be made. However, we find that the interaction of He/Rh(110) and Ne/Rh(110) is not only defined by the interaction of He and Ne orbitals with Rh 5s and Rh 5p, in addition the Rh 4d orbitals have a moderate contribution.

The interaction of a CO molecule on Pt(110) was treated using ultrasoft pseudopotentials and the GGA. Two possible structures were considered for the Pt substrate: an unreconstructed surface and a missing row structure. For both structures the short bridge is found to be the most stable adsorption site which is in conflict with the experimentally determined site. We observed that the relaxation of the substrate can increase the binding energy by as much as 0.5 eV. Also we find that the lateral repulsive energy can significantly affect the binding energy. The unreconstructed structure was found to provide a higher CO binding energy than the missing row structure for the all adsorption sites considered. This could provide an explanation for the adsorbate-induced reconstruction observed in this system.

Appendix A

Generalised Gradient Functionals

In this appendix the generalised gradient approximation functionals used in the present work are presented. The GGA exchange energy is written as

$$E_x[\rho] = \frac{-3}{4} \sqrt[3]{\frac{3}{\pi}} \int F_x(s) \rho^{\frac{4}{3}} d^3r, \quad (\text{A.1})$$

where ρ is the electron charge density; s is reduced density gradient defined by

$$s = \frac{|\nabla\rho|}{2k_F\rho}, \quad (\text{A.2})$$

and k_F is the Fermi vector given by

$$k_F = \sqrt[3]{3\pi^2\rho}. \quad (\text{A.3})$$

The enhancement factor $F_x(s)$ within GGA-PW91 has an analytic parametrisation given by (Perdew & Wang, 1992)

$$F_x^{\text{pw91}} = \frac{1 + 0.19645s \sinh^{-1}(7.7956s) + s^2(0.2743 - 0.1508 \exp(-100s^2))}{1 + 0.19645s \sinh^{-1}(7.7956s) + 0.004s^4}, \quad (\text{A.4})$$

where

$$\sinh^{-1}(x) = \ln \left[x + \sqrt{1 + x^2} \right]. \quad (\text{A.5})$$

The GGA correlation energy functional is defined by (see Burke *et al.* (1998))

$$E_c[\rho] = \int [e_c(r_s) + H(\rho, s, t)] \rho dr, \quad (\text{A.6})$$

where $e_c(r_s)$ is the correlation energy per particle. For an unpolarised system it is given by

$$e_c(r_s) = -0.0621814 (1 + 0.21370r_s) Q, \quad (\text{A.7})$$

with

$$Q = \ln \left[1 + \frac{1}{0.0621814 (7.5957\sqrt{r_s} + 3.5876r_s + 1.6382\sqrt{r_s^3} + 0.49294r_s^2)} \right], \quad (\text{A.8})$$

where the local Seitz radius, r_s , is defined by

$$r_s = \sqrt[3]{\frac{3}{4\pi\rho}}. \quad (\text{A.9})$$

The non-linear contribution $H(n, s, t)$ has the following analytic representation

$$H(\rho, s, t) = \frac{\beta^2}{2\alpha} \ln \left[1 + 2\frac{\alpha}{\beta} \left(\frac{t^2 + At^4}{1 + At^2 + A^2t^4} \right) \right] + 15.75592 (C_c(\rho) - 0.003521) t^2 \exp(-100s^2), \quad (\text{A.10})$$

where t is

$$t = \frac{|\nabla\rho|}{2k_s\rho}, \quad (\text{A.11})$$

the Thomas-Fermi screening vector, k_s , is given by

$$k_s = \sqrt{\frac{4k_F}{\pi}}, \quad (\text{A.12})$$

$$A = 2 \frac{\alpha}{\beta} \left(\frac{1}{\exp\left(\frac{-2\alpha\epsilon_c(\rho)}{\beta^2}\right) - 1} \right), \quad (\text{A.13})$$

and

$$C_c(\rho) = 0.001667 + \frac{0.002568 + 0.023266r_s + 7.386 \times 10^{-6}r_s^2}{1 + 8.723r_s + 0.472r_s^2 + 7.389 \times 10^{-2}r_s^3}. \quad (\text{A.14})$$

In the case of GGA-PBE exchange-correlation, (Perdew *et al.*, 1996b) the enhancement factor and the non-linear contribution for the correlation energy, $H(\rho, s, t)$, have new representations. The enhancement term is given by

$$F_x^{PBE} = 1 + k - \frac{k}{1 + \frac{\mu s^2}{k}}, \quad (\text{A.15})$$

where k and μ are numerical constants, whose values are 0.804 and 0.21951 respectively. $H^{PBE}(\rho, s, t)$ is defined by

$$H^{PBE}(\rho, s, t) = \gamma \ln \left[1 + \frac{\beta}{\gamma} t^2 \frac{1 + At^2}{1 + At^2 + A^2t^4} \right], \quad (\text{A.16})$$

where the parameter A is given as

$$A = \frac{\beta}{\gamma \left(\exp\left(\frac{\epsilon_c}{\gamma}\right) - 1 \right)}, \quad (\text{A.17})$$

β is defined by

$$\beta = \frac{3\mu}{\pi^2}, \quad (\text{A.18})$$

and $\gamma = 0.031091$.

The exchange potential is the functional derivative (Perdew & Wang, 1986)

$$\frac{\delta E_x}{\delta \rho(r)} = \frac{-3}{4} \sqrt[3]{\frac{3\rho}{\pi}} \left[\frac{4}{3} F - \frac{p}{s} \frac{dF}{ds} - \left(u - \frac{4}{3} s^3 \right) \frac{d}{ds} \left(s^{-1} \frac{dF}{ds} \right) \right], \quad (\text{A.19})$$

where

$$p = \frac{\nabla^2 \rho}{(2k_F)^2 \rho}, \quad (\text{A.20})$$

and

$$u = \frac{\nabla \rho \cdot \nabla |\nabla \rho|}{(2k_F)^3 \rho^2}. \quad (\text{A.21})$$

Finally, the correlation potential is given by (Perdew *et al.*, 1996a)

$$\begin{aligned} \frac{\delta E_c}{\delta \rho(r)} = & \epsilon_c + H - \frac{r_s}{3} \left(\frac{\partial \epsilon_c}{\partial r_s} + \frac{\partial H}{\partial r_s} \right) + \frac{r_s}{3} t \frac{\partial^2 H}{\partial r_s \partial t} \\ & + \frac{t}{6} \frac{\partial H}{\partial t} + \left[\left[\frac{7}{6} t^3 - u \right] \frac{\partial}{\partial t} - p \right] \left(\frac{1}{t} \frac{\partial H}{\partial t} \right). \end{aligned} \quad (\text{A.22})$$

References

- Abarenkov, I. V., & Heine, V. 1965. The model potential for positive ions. *Phil. Mag.*, **12**, 529.
- Akai, H., & Dederichs, P. H. 1985. A simple improved iteration scheme for electronic structure calculations. *J. Phys. C*, **18**, 2455.
- Anderson, O. L. 1966. The use of ultrasonic measurements under modest pressure to estimate compression at high pressure. *J. Phys. Chem. Solid*, **27**, 547.
- Andersson, Y., Hult, E., Rydberg, H., Apell, P., Lundqvist, B. I., & Langreth, D. 1998. van der Waals interactions in density functional theory. *Pages 243–260 of: Dobson, J. F., Vignale, G., & Das, M. P. (eds), Electronic Density Functional Theory. Recent Progress and New Directions.* New York: Plenum Press.
- Annett, J. F., & Haydock, R. 1983. Helium diffraction from metal surfaces: Elimination of a class of potential. *Phys. Rev. B*, **29**(6), 3773.
- Annett, J. F., & Haydock, R. 1984. Anticorrugating effect of hybridization on the helium diffraction potential for metal surfaces. *Phys. Rev. Lett.*, **53**(8), 838.
- Annett, J. F., & Haydock, R. 1986. Hybridization interaction between helium and a metal surface. *Phys. Rev. B*, **34**(10), 6860.
- Arfken, G. B., & Weber, H. J. 1995. *Mathematical Methods for Physicists*. Fourth edn. San Diego: Academic Press.

- Ashcroft, N. W., & Mermin, N. D. 1976. *Solid State Physics*. Saunders College Publishing.
- Attard, G., & Barnes, C. 1998. *Surfaces*. Oxford: Oxford University Press.
- Bachelet, G., & Schlüter, M. 1982. Relativistic norm-conserving pseudopotentials. *Phys. Rev. B*, **25**(4), 2103.
- Bachelet, G. B., Hamann, D., & Schlüter, M. 1982. Pseudopotentials that work: From H to Pu. *Phys. Rev. B*, **26**(8), 4199.
- Bare, S. R., Hofmann, P., & King, D. A. 1984. Vibrational studies of the surface phases of CO on Pt{110} at 300 K. *Surf. Sci.*, **144**(2), 347.
- Barker, J. A., & Rettner, C. T. 1992. Accurate potential energy surface for Xe/Pt(111): A benchmark gas/surface interaction potential. *J. Chem. Phys.*, **97**(8), 5844.
- Barker, J. A., Watts, R. O., Lee, J. K., Schafer, T. P., & Lee, T. 1974. Solid-state properties of Xe of 0 °K. *J. Chem. Phys.*, **61**, 3081.
- Becke, A. D. 1988. Density-functional exchange approximation with correct asymptotic behavior. *Phys. Rev. A*, **38**(6), 3098.
- Bendt, P., & Zunger, A. 1982. New approach for solving the density-functional self-consistent-field problem. *Phys. Rev. B*, **26**(6), 3114.
- Bertel, E. 1996. The interaction of rare gases with transition metal surfaces. *Surf. Sci.*, **367**, L61.
- Betancourt, A. E., & Bird, D. M. 2000. First principles calculation of the interaction energy of ($\sqrt{3} \times \sqrt{3}$) R30° Xe/Pt(111). *J. Phys. Condens. Matter*, **12**, 7077.
- Bird, D. M. 1997. *Private communication*.

- Bird, D. M., & Gravil, P. A. 1997. First-principles calculations of molecular dissociation at surfaces. *Surf. Sci.*, **377-379**(1-3), 555.
- Black, J. E., & Janzen, A. 1988. Uniaxial strain events in molecular-dynamics simulations of small rafts of xenon physisorbed on Pt(111). *Phys. Rev. B*, **38**(12), 8494.
- Blyholder, G. 1964. Molecular orbital view of chemisorbed carbon monoxide. *J. Phys. Chem.*, **68**(10), 2772.
- Börnsen, N., Meyer, B., Grotheer, O., & Fähnle, M. 1999. E_{cov} - a new tool for the analysis of electronic structure data in a chemical language. *J. Phys. Condens. Matter*, **11**, L287.
- Bradshaw, A. M. 1997. Structural studies of adsorbed molecules and molecular fragments: the surface-cluster analogy re-visited. *Surf. Sci.*, **331-333**, 978.
- Bruch, L. W., Cole, M. W., & Zaremba, E. 1997. *Physical Adsorption: Force and Phenomena*. Oxford: Clarendon Press.
- Bruch, L. W., Graham, A. P., & Toennies, P. 1998. Vibrations of the commensurate monolayer solid Xe/Pt(111). *Molec. Phys.*, **95**(3), 579.
- Buldum, A., & Ciraci, S. 1996. Controlled lateral and perpendicular motion of atoms on metal surfaces. *Phys. Rev. B*, **54**(3), 2175.
- Burda, B. V., Zahradnik, R., Hobza, P., & Urban, M. 1996. Dimers of rare gas atoms: CCSD(T) and CCSDT calculations on the (He)₂ dimer, CCSD(T) and CCSDT calculations on the (Ne)₂ dimer, and CCSD(T) all-electron and pseudopotential calculations on the dimer from (Ne)₂ through (Xe)₂. *Molec. Phys.*, **89**(2), 425.
- Burke, K., Perdew, J. P., & Wang, Y. 1998. Derivation of a generalized gradient approximation: The PW91 density functional. *Pages 81-111 of: Dobson, J. F.*,

-
- Vignale, G., & Das, M. P. (eds), *Electronic Density Functional Theory. Recent Progress and New Directions*. New York: Plenum Press.
- Callaway, J., & March, N.H. 1984. Density functional methods: Theory and applications. *Pages 135-221 of: Ehrenreich, H., & Turnbull, D. (eds), Solid State Physics*, vol. 38. New York: Academic Press.
- Car, R., & Parrinello, M. 1985. Unified approach for molecular dynamics and density-functional theory. *Phys. Rev. Lett.*, **55**(22), 2471.
- Cassuto, A., & Erhardt, J. J. 1988. Angle-resolved photoemission of xenon adsorbed on Pt(111): commensurate and incommensurate monolayers. *J. Phys. (France)*, **49**, 1753.
- Ceperly, D. M., & Alder, B. J. 1980. Ground state of the electron gas by a stochastic method. *Phys. Rev. Lett.*, **45**(7), 566.
- Chadi, D. J., & Cohen, M. L. 1973. Special points in the Brillouin zone. *Phys. Rev. B*, **8**(12), 5747.
- Clarke, S., Nekovee, M., de Boer, P. K., & Inglesfield, J. E. 1998. The effect of electric fields on Ag(001) c(2×2)-Xe. *J. Phys. Condens. Matter*, **10**, 7777.
- Comrie, C. M., & Lambert, R. M. 1976. Chemisorption and surface structural chemistry of carbon monoxide on Pt(110). *J. Chem. Soc. Faraday Trans.*, **72**, 1659.
- Cunningham, S. L. 1974. Special points in two-dimensional Brillouin zone. *Phys. Rev. B*, **10**(12), 4988.
- Curulla, D., Clotet, A., Ricart, M., & Illas, F. 1999. Ab initio cluster model study of the chemisorption of CO on low-index platinum. *J. Phys. Chem. B*, **103**, 5246.
- Darling, G. R., & Holloway, S. 1995. The dissociation diatomic molecules at surface. *Rep. Prog. Phys.*, **58**, 1595.

-
- de Vita, A., & Gillan, M. J. 1991. The *ab initio* calculation of defect energetics in aluminium. *J. Phys. Condens. Matter*, **3**, 6225.
- Dobson, J. F., Dinte, B. P., & Wang, J. 1998. van der Waals functionals via local approximations for susceptibilities. *Pages 261–284 of: Dobson, J. F., Vignale, G., & Das, M. P. (eds), Electronic Density Functional Theory. Recent Progress and New Directions.* New York: Plenum Press.
- Eichler, A., Hafner, J., Kresse, G., & Furthmüller, J. 1996. Relaxation and electronic surface states of rhodium surfaces. *Surf. Sci.*, **352-354**, 689.
- Eigler, D. M., Weiss, P. S., Schweitzer, E. K., & Lang, N. D. 1991. Imaging Xe with a low-temperature scanning tunneling microscope. *Phys. Rev. Lett.*, **66**(9), 1189.
- Ellis, J., Graham, A. P., & Toennies, J. P. 1999. Quasielastic helium atom scattering from a two-dimensional gas of Xe atoms on Pt(111). *Phys. Rev. Lett.*, **82**(25), 5072.
- Elsässer, C., Takeuchi, N., Ho, K. M., Chan, C. T., Braun, P., & Fähnle, F. 1990. Relativistic effects on ground state properties of 4d and 5d transition metals. *J. Phys. Condens. Matter*, **2**, 4371.
- Engstrom, J. R., & Weinberg, W. H. 1988. Analysis of gas-surface reactions by surface temperature modulation: Experimental applications to the adsorption and oxidation of carbon monoxide on the Pt(110)-(1×2) surface. *Surf. Sci.*, **201**, 145.
- Esbjerg, N., & Nørskov, J. K. 1980. Dependence of the He-scattering potential at surfaces on the surface-electron-density profile. *Phys. Rev. Lett.*, **45**(10), 807.
- Eyert, V. 1996. A comparative study on methods for convergence acceleration of iterative vector sequences. *J. Compt. Phys.*, **124**, 271.

- Fair, J., & Madix, R. J. 1980. Low and high coverage determinations of the rate of carbon monoxide adsorption and desorption from Pt(110). *J. Chem. Phys.*, **73**(7), 3480.
- Fariás, D., & Rieder, K. H. 1998. Atomic beam diffraction from solid surfaces. *Rep. Prog. Phys.*, **61**, 1575.
- Feibelman, P. J., Hammer, B., Nørskov, J. K., Wagner, F., Scheffler, M., Stumpf, R., Watwe, R., & Dumesic, J. 2000. The CO/Pt(111) puzzle. in press.
- Fenter, P., & Gustafsson, T. 1988. Structural analysis of the Pt(110)-(1×2) surface using medium-energy ion scattering. *Phys. Rev. B*, **38**(15), 10197.
- Ferreira, L. G. 1980. Theory and method for accelerating the convergence of self-consistent electronic structure calculations. *J. Comput. Phys.*, **36**, 199.
- Flynn, C. P., & Chen, Y. C. 1981. Work function and bonding energy of rare-gas atoms adsorbed on metals. *Phys. Rev. Lett.*, **46**(6), 447.
- Foiles, S. M. 1987. Reconstruction of fcc(110) surface. *Surf. Sci.*, **191**(1-2), L779.
- Freyer, N., Kiskinova, M., Pirug, G., & Bonzel, H. P. 1986. Site-specific core level spectroscopy of CO and NO adsorption on Pt(110)(1×2) and (1×1) surfaces. *Appl. Phys. A*, **39**, 209.
- Fu, C. L., & Ho, K. M. 1983. First-principles calculation of the equilibrium ground-state properties of transition metals: Applications to Nb and Mo. *Phys. Rev. B*, **28**(10), 5480.
- Fuchs, M., & Scheffler, M. 1999. Ab initio pseudopotentials for electronic structure calculations of poly-atomic systems using density-functional theory. *Comput. Phys. Commun.*, **119**, 67.

- Fuchs, M., Bockstedte, M., Pehlke, E., & Scheffler, M. 1998. Pseudopotential study of binding properties of solids within generalized gradient approximations: The role of core-valence exchange correlation. *Phys. Rev. B*, **57**(4), 2134.
- Fujiwara, T., & Hoshi, T. 1997. Optimized ultrasoft pseudopotentials. *J. Phys. Soc. Japan*, **66**(6), 1723.
- García, A., Elsässer, C., Zhu, J., & Louie, S. G. 1992. Use of gradient-corrected functionals in total-energy calculations for solids. *Phys. Rev. B*, **46**(15), 9829.
- Ge, Q., & King, D. A. 1999. Surface diffusion potential energy surfaces from first principles: CO chemisorbed on Pt{110}. *J. Chem. Phys.*, **111**(21), 9461.
- Ge, Q., Brown, A., Sharma, R. K., & King, D. A. 1999. NO monomer and (NO)_x polymeric chain chemisorption on Pt{110}. *J. Chem. Phys.*, **110**(24), 12082.
- Gidopoulos, N. 1998. Kohn-Sham equations for multicomponent systems: The exchange and correlation energy functional. *Phys. Rev. B*, **57**(4), 2146.
- Gillan, M. J. 1989. Calculation of the vacancy formation energy in aluminium. *J. Phys. C*, **1**, 689.
- Gonze, X., Käckell, P., & Scheffler, M. 1990. Ghost states for separable, norm-conserving, *ab initio* pseudopotentials. *Phys. Rev. B*, **41**(17), 12264.
- Gonze, X., Stumpf, R., & Scheffler, M. 1991. Analysis of separable potentials. *Phys. Rev. B*, **44**(16), 8503.
- Gordon, R. G., & Kim, Y. S. 1972. Theory for the forces between closed-shell atoms and molecules. *J. Chem. Phys.*, **56**(6), 3122.
- Gottlieb, J. M. 1990. Energy and structure of uniaxial incommensurate monolayer solid: Application to Xe/Pt(111). *Phys. Rev. B*, **42**(8), 5377.
- Graham, A. P., , McCash, E. M., & Allison, W. 1995. Adsorbate structure in the H-induced p4g reconstruction of the Cu(001) surface. *Phys. Rev. B*, **51**, 5306.

- Graham, A. P., Fang, D., McCash, E. M., & Allison, W. 1998. Adsorption of atomic hydrogen on Cu(001) studied with helium-atom scattering. *Phys. Rev. B*, **57**(20), 13158.
- Gritsch, T., Coulman, D., Behm, R. J., & Ertl, G. 1989. Mechanism of CO-induced $1\times 2 \rightarrow 1\times 1$ structural transformation of Pt(110). *Phys. Rev. Lett.*, **63**(10), 1087.
- Gross, E. K.U., Kurth, S., Cappelle, K., & Lüders, M. 1995. Density functional theory of superconducting state. *Pages 431–460 of: Gross, E. K. U., & Dreizler, R. M. (eds), Density Functional Theory.*, vol. 337. New York: Plenum Press.
- Grosso, G., & Parravicini, G. Pastori. 2000. *Solid State Physics*. Cambridge: Academic Press.
- Gülseren, O., Bird, D. M., & Humphreys, S. E. 1998. A mixed-basis approach for the efficient calculation of potential energy surfaces. *Surf. Sci.*, **402-404**, 827.
- Hall, B., Mills, D. L., Zeppenfeld, P., Kern, K., Becher, U., & Comsa, G. 1989. Anharmonic damping in rare-gas multilayers. *Phys. Rev. B*, **40**(9), 6326.
- Hama, J., & Watanabe, M. 1992. General formulae for the special points and their weighting factors in k -space integration. *J. Phys. Condens. Matter*, 4583.
- Hamman, D., Schlüter, M., & Chiang, C. 1979. Norm-conserving pseudopotentials. *Phys. Rev. Lett.*, **43**(20), 1494.
- Hammer, B., & Nørskov, J. K. 1997. Theory of adsorption and surface reactions. *Pages 285–351 of: Lambert, R.M., & Pacchioni, G. (eds), Chemisorption and Reactivity on Supported Clusters and Thin Films*, vol. 331. Dordrecht: Kluwer Academic.
- Hammer, B., Morikawa, Y., & Nørskov, J. K. 1996. CO chemisorption at metal surfaces and overlayers. *Phys. Rev. Lett.*, **76**(12), 2141.

-
- Hammer, B., Nielsen, O. H., & Nørskov, J. K. 1997. Structure sensitivity in adsorption: CO interaction with stepped and reconstructed Pt surfaces. *Catal. Lett.*, **46**, 31.
- Hammer, B., Hansen, L. B., & Nørskov, J. K. 1999. Improved adsorption energetics within density-functional theory using revised Perdew-Burke-Ernzerhof functionals. *Phys. Rev. B*, **59**(11), 7413.
- Harris, J., & Zaremba, E. 1985. Comment on "Anticorrugating effect of hybridization on the helium diffraction potential for metal surfaces". *Phys. Rev. Lett.*, **55**(18), 1940.
- Hedin, L., & Lundqvist, B. I. 1971. Explicit local exchange-correlation potentials. *J. Phys. C*, **4**, 2064.
- Heinonen, O., Lubin, M. I., & Johnson, M. D. 1998. Ensemble density functional theory for inhomogeneous fractional quantum hall systems. *Pages 311–325 of: Dobson, J. F., Vignale, G., & Das, M. P. (eds), Electronic Density Functional Theory. Recent Progress and New Directions.* New York: Plenum Press.
- Hohenberg, P., & Kohn, W. 1964. Inhomogeneous electron gas. *Phys. Rev.*, **136**(3B), B864.
- Hoinkes, H. 1980. The physical interaction potential of gas atoms with single-crystal surfaces, determined from gas-surface diffraction experiments. *Rev. Mod. Phys.*, **52**(4), 933.
- Holmberg, C., & Apell, P. 1984. van der Waals interaction in atom-surface scattering. *Phys. Rev. B*, **30**(10), 5721.
- Horch, S., Zeppenfeld, P., & Cosma, G. 1995. Temperature dependence of the xenon-layer morphology on platinum (111) studied with scanning tunneling microscopy. *Surf. Sci.*, **331-333**, 908.

-
- Hu, P., King, D. A., Crampin, S., Lee, M. H., & Payne, M. C. 1994. Gradient corrections in density functional theory calculations for surfaces: CO on Pd {110}. *Chem. Phys. Lett.*, **230**, 501.
- Huber, K. P., & Herzberg, G. 1979. *Constants of diatomic molecules. Molecular spectra and molecular structure*. Vol. IV. New York: Van Nostrand Reinhold.
- Hult, E., Rydberg, H., Lundqvist, B., & D, Langreth. 1999. Unified treatment of asymptotic van der Waals forces. *Phys. Rev. B*, **59**(7), 4708.
- Ihm, J. 1988. Total energy calculations in solid state physics. *Rep. Prog. Phys.*, **51**, 4105.
- Ihm, J., Zunger, A., & Cohen, M. L. 1979. Momentum-space formalism for the total energy of solids. *J. Phys. C*, **12**, 4409.
- Imbihl, R., Ladas, S., & Ertl, G. 1988. The CO-induced $1 \times 2 \leftrightarrow 1 \times 1$ phase transition of Pt(110) studied by LEED and work function measurements. *Surf. Sci.*, **206**, L903.
- Ishi, S., & Viswanathan, B. 1991. Adsorption of xenon atoms on metal surfaces. *Thin Solid Films*, **201**, 373.
- Johnson, D. D. 1988. Modified Broyden's method for accelerating convergence in self-consistent calculations. *Phys. Rev. B*, **38**(18), 12807.
- Jones, R. O., & Gunnarsson, O. 1989. The density functional formalism, its applications and prospects. *Rev. Mod. Phys.*, **61**(3), 689.
- Juan, Y-M, & Kaxiras, E. 1993. Application of gradient corrections to density-functional theory for atoms and solids. *Phys. Rev. B*, **48**(20), 14944.
- Kerker, G. P. 1980a. Efficient iteration scheme for self-consistent pseudopotential calculations. *Phys. Rev. B*, **23**(6), 3082.

-
- Kerker, G. P. 1980b. Non-singular atomic pseudopotential for solid state applications. *J. Phys. C*, **13**, L189.
- Kern, K., David, R., Zeppenfeld, P., & Cosma, G. 1988. Registry effects in the thermodynamic quantities of Xe adsorption on Pt(111). *Surf. Sci.*, **195**(1-2), 353.
- Khein, A., Singh, D. J., & Umrigar, C. J. 1995. All-electron study of gradient corrections to the local-density functional in metallic systems. *Phys. Rev. B*, **51**(7), 4105.
- Kleinman, K. 1980. Relativistic norm-conserving pseudopotential. *Phys. Rev. B*, **21**(6), 2630.
- Kleinman, L., & Bylander, D. M. 1982. Efficacious form for model pseudopotentials. *Phys. Rev. Lett.*, **48**(20), 1425.
- Kohn, W. 1999. Electronic structure of matter-wave functions and density functionals. *Rev. Mod. Phys.*, **71**(5), 1253.
- Kohn, W., & Sham, L. J. 1965. Self-consistent equation including exchange and correlation effects. *Phys. Rev.*, **140**(4A), A1133.
- Kresse, G., & Furthmüller, J. 1996a. Efficient iterative schemes for *ab initio* total-energy calculations for metals and semiconductors using a plane-wave basis set. *Compt. Mater. Sci.*, **6**, 15.
- Kresse, G., & Furthmüller, J. 1996b. Efficient iterative schemes for *ab initio* total-energy calculations using a plane-wave basis set. *Phys. Rev. B*, **54**(16), 11169.
- Kulginov, D., Persson, M., & Rettner, C. T. 1996. Dynamics of collision-induced desorption: Ar-Xe/Pt(111). *J. Chem. Phys.*, **106**, 3370.
- Küppers, J., Nitschké, F., Wandelt, R., & Ertl, G. 1979. The adsorption of Xe on Pd(110). *Surf. Sci.*, **87**, 295.

-
- Laasonen, K., Pasquarello, A., Car, R., Lee, C., & Vanderbilt, D. 1993. Car-Parrinello molecular dynamics with Vanderbilt ultrasoft pseudopotentials. *Phys. Rev. B*, **47**(16), 10142.
- Lang, N. D. 1981. Interaction between closed-shell system and metal surfaces. *Phys. Rev. Lett.*, **46**(13), 842.
- Lang, N. D., & Nørskov, J. K. 1983. Interaction of helium with a metal surface. *Phys. Rev. B*, **27**(8), 4612.
- Lang, N. D., Willians, A. R., Himpsel, F. J., Reihl, B., & Eastman, D. E. 1982. Absence of a charge-transfer instability for rare-gas atoms adsorbed on metals. *Phys. Rev. B*, **26**(4), 1728.
- Langreth, D. C., & Mehl, J. 1983. Beyond the local-density approximation in calculations of ground-state electronic properties. *Phys. Rev. B*, **28**(4), 1809.
- Lapujoulade, J., & Perreau, J. 1983. The diffraction of molecular hydrogen from copper surfaces. *Phys. Scr.*, **T4**, 138.
- Lee, C., Yang, W., & Parr, R. G. 1988. Development of the Colle-Salvetti correlation-energy formula into a functional of the electron density. *Phys. Rev. B*, **37**(2), 785.
- Lee, I. H., & Martin, R. M. 1997. Applications of the generalized-gradient approximation to atoms, clusters and solids. *Phys. Rev. B*, **56**(12), 7197.
- Lide, D. R., & Frederikse, H. P.R. (eds). 1997. *CRC Handbook of Chemistry and Physics*. 78th edn. New York: CRC Press.
- Liebsch, A. 1987. Density-functional calculation of quadrupolar contributions to the atom-metal van der Waals interaction. *Phys. Rev. B*, **35**(17), 9030.
- Lin, J.S., Qteish, A., Payne, M. C., & Heine, V. 1993. Optimized and transferable nonlocal separable *ab initio* pseudopotentials. *Phys. Rev. B*, **47**(8), 4174.

- Louie, S. G., Ho, K. M., & Cohen, M. L. 1979. Self-consistent mixed-basis approach to the electronic structure of solid. *Phys. Rev. B*, **19**(4), 1774.
- Louie, S. G., Froyen, S., & Cohen, M. L. 1982. Nonlinear ionic pseudopotentials in spin-density-functional calculations. *Phys. Rev. B*, **26**(4), 1738.
- Lundqvist, B. I. 1990. Theoretical aspects of adsorption. *Pages 213–254 of: Bor-tolani, V., March, N. H., & Tosi, M. P. (eds), Interaction of Atoms and Molecules with Solid Surfaces.* New York: Plenum Press.
- Lundqvist, B. I., Hult, E., Rydberg, H., Bogicevic, A., Strömquist, J., & Langreth, D. 1998. Density functionals and van der Waals interactions at surfaces. *Prog. Surf. Sci.*, **59**(1-4), 149.
- Lynch, M., & Hu, P. 2000. A density functional theory study of CO and atomic oxygen chemisorption on Pt(111). *Surf. Sci.*, **458**, 1.
- Ma, J., Xiao, X., DiNardo, N. J., & Loy, M. M. T. 1998. Diffusion of CO on Pt(111) studied by an optical diffraction method. *Phys. Rev. B*, **58**(8), 4977.
- Malafsky, G. P. 1992. Influence of the xenon induced work function change on the xenon binding energy in photoemission of adsorbed xenon. *J. Vac. Sci. Technol. A*, **11**(4), 2158.
- Masel, R. 1996. *Principles of Adsorption and Reaction on Solid Surfaces.* New York: Wiley.
- Mermin, N. D. 1965. Thermal properties of the inhomogeneous electron gas. *Phys. Rev.*, **137**(5A), A1441.
- Monkhorst, H. J., & Pack, J. D. 1976. Special points for Brillouin-zone integrations. *Phys. Rev. B*, **13**(12), 5188.

- Montalenti, F., Trioni, M. I., Brivio, G. P., & Crampin, S. 1996. Ab initio results for the adiabatic atom-surface interaction for helium and neon on a simple metal. *Surf. Sci.*, **364**, L595.
- Moreno, J., & Soler, J. M. 1992. Optimal meshes for integrals in real- and reciprocal-space unit cells. *Phys. Rev. B*, **45**(24), 13891.
- Morrison, I. A., Kang, M. H., & Mele, E. J. 1989. First-principles determination of the bulk phase diagram for body-centered-tetragonal copper: Application to epitaxial growth of Cu on Fe{100}. *Phys. Rev. B*, **39**(3), 1575.
- Moruzzi, V. L., & Sommers, C. B. 1995. *Calculated Electronic Properties of Ordered Alloy*. Singapore: World Scientific.
- Müller, J. E. 1990. Interaction of the Pt(111) surface with adsorbed Xe atoms. *Phys. Rev. Lett.*, **65**(24), 3021.
- Mulliken, R. S. 1955. Electronic population analysis on LCAO-MO molecular wave functions. I. *J. Chem. Phys.*, **23**(10), 1833.
- Murnaghan, F. D. 1944. The compressibility of media under extreme pressures. *Proc. N. A. S.*, **30**, 244.
- Narloch, B., & Menzel, D. 1998. The geometry of Xe and Krypton on Ru(001): a LEED IV investigation. *Surf. Sci.*, **412**, 562.
- Nichtl, W., Bickel, N., Hammer, L., Heinz, K., & Müller, K. 1987. Surface relaxation change by hydrogen adsorption on Rh(110). *Surf. Sci.*, **188**, L729.
- Nørskov, J. K. 1990. Chemisorption on metal surface. *Rep. Prog. Phys.*, **53**, 1253.
- Ortiz, G., & Ballone, P. 1991. Pseudopotentials for non-local density functionals. *Phys. Rev. B*, **43**(8), 6376.

-
- Ozoliņš, V., & Körling, M. 1993. Full-potential calculations using the generalized gradient approximation: Structural properties of transition metals. *Phys. Rev. B*, **48**(24), 19304.
- Pacchioni, G., Chung, S. C., Krüger, S., & Rösch, N. 1997. Is CO chemisorbed on Pt anomalous compared with Ni and Pd? An example of surface chemistry dominated by relativistic effects. *Surf. Sci.*, **392**, 173.
- Parr, R., & Yang, W. 1989. *Density-Functional Theory of Atoms and Molecules*. Series of monographs on chemistry - 16. New York: Oxford University Press.
- Parschau, G., Kirsten, E., Bischof, A., & Rieder, K. H. 1989. Diffraction of He and Ne and selective adsorption of He on Rh(110). *Phys. Rev. B*, **40**(9), 6012.
- Patchett, A. J., Meißner, F., Engel, W., Bradshaw, A. M., & Imbihl, R. 2000. The anatomy of reaction diffusion fronts in the catalytic oxidation of carbon monoxide on platinum (110). *Surf. Sci.*, **341-346**, 454.
- Patton, D. C., & Pederson, M. R. 1997. Application of the generalized-gradient approximation to rare-gas dimers. *Phys. Rev. A*, **56**(4), R2495.
- Patton, D. C., Porezag, D. V., & Pederson, M. R. 1997. Simplified generalized-gradient approximation and anharmonicity: Benchmark calculations on molecules. *Phys. Rev. B*, **55**(12), 7454.
- Payne, M. C., Teter, M. P., Allan, D. C., Arias, T. A., & Joannopoulos, J. D. 1992. Iterative minimization techniques for *ab initio* total-energy calculations: molecular dynamics and conjugate gradients. *Rev. Mod. Phys.*, **64**, 1045.
- Perdew, J. P. 1995. Density gradient expansion of the electronic exchange-correlation energy, and its generalization. *Pages 51-65 of: Gross, E. K. U., & Dreizler, R. M. (eds), Density Functional Theory.*, vol. 337. New York: Plenum Press.

-
- Perdew, J. P., & Wang, Y. 1986. Accurate and simple density functional for the electronic exchange energy: Generalized gradient approximation. *Phys. Rev. B*, **33**(12), 8800.
- Perdew, J. P., & Wang, Y. 1992. Accurate and simple analytic representation of the electron-gas correlation energy. *Phys. Rev. B*, **45**(23), 13244.
- Perdew, J. P., & Zunger, A. 1981. Self-interaction correction to density-functional approximations for many-electron systems. *Phys. Rev. B*, **23**(10), 5048.
- Perdew, J. P., Chevary, J. A., Vosko, S. H., Jackson, K. A., Pederson, M. R., Singh, D. J., C., & Fiolhais. 1992. Atoms, molecules, solids, and surfaces: Applications of the generalized gradient approximation for exchange and correlation. *Phys. Rev. B*, **46**(11), 6671.
- Perdew, J. P., Burke, K., & Wang, Y. 1996a. Generalized gradient approximation for the exchange-correlation hole of a many-electron system. *Phys. Rev. B*, **54**(23), 16533.
- Perdew, J. P., Burke, K., & Ernzerhof, M. 1996b. Generalized gradient approximation made simple. *Phys. Rev. Lett.*, **77**(18), 3865.
- Perdew, J. P., Burke, K., & Ernzerhof, M. 1998. Perdew, Burke, and Ernzerhof reply. *Phys. Rev. Lett.*, **80**(4), 891.
- Perdew, J. P., Kurth, S., Zupan, A., & Blaha, P. 1999. Accurate density functional with correct formal properties: A step beyond the generalized gradient approximation. *Phys. Rev. Lett.*, **82**(12), 2544.
- Pérez, R., García-Vidal, J.J., de Andrés, P. L., & Flores, F. 1994. Adsorption of Xe on metals: a theoretical analysis. *Surf. Sci.*, **307-309**, 704.
- Petersen, M., Wilke, S, Ruggerone, P., Kohler, B., & Scheffler, M. 1996. Scattering of rare-gas atoms at a metal surface: Evidence of anticorrugation of the helium-

- atom potential energy surface and the surface electron density. *Phys. Rev. Lett.*, **76**(6), 995.
- Phillips, J. C., & Kleinman, L. 1959. New method for calculating wave function in crystals and molecules. *Phys. Rev.*, **116**(2), 287.
- Potthoff, M., Hilgers, G., Müller, N., Heinzmann, U., Haunert, L., Braun, J., & Borstel, G. 1995. Structure investigation of the Xe-adsorbate layers by spin-polarized low-energy electron diffraction I. ($\sqrt{3} \times \sqrt{3}$)R30° – Xe/Pt(111). *Surf. Sci.*, **332**, 193.
- Press, W. H., Teukolsky, S. A., Vetterling, W. T., & Flannery, B. P. 1992. *Numerical Recipes in FORTRAN The Art of Scientific Computing*. Cambridge: Cambridge University Press.
- Pulay, P. 1969. *Ab initio* calculation of force constants and equilibrium geometries in polyatomic molecules. I. Theory. *Mol. Phys.*, **17**(2), 197.
- Rajagopal, A. K. 1998. A functional theory of interacting local spins, spin polarized electrons, and ions: Half metallic magnets. *Pages 361–371 of: Dobson, J. F., Vignale, G., & Das, M. P. (eds), Electronic Density Functional Theory. Recent Progress and New Directions*. New York: Plenum Press.
- Rappe, A., Rabe, K., Kaxiras, E., & Joannopoulos, J. 1990. Optimized pseudopotentials. *Phys. Rev. B*, **41**(2), 1227.
- Rieder, K. H., & García, N. 1982. Energy dependence and softness of the potential for He scattering from Ni(110). *Phys. Rev. Lett.*, **49**(1), 43.
- Rieder, K. H., & Stocker, W. 1984. Observation of pronounced neon diffraction from low-index metal-surfaces. *Phys. Rev. Lett.*, **52**(5), 352.
- Rieder, K. H., & Stocker, W. 1985. Scattering of He, Ne, Ar, H₂, and N₂ from Cu(110). *Phys. Rev. B*, **31**(6), 3392.

-
- Rieder, K. H., Parschau, G., & Burg, B. 1993. Experimental-evidence for anti-corrugating effects in He-metal interactions at surfaces. *Phys. Rev. Lett.*, **71**(7), 1059.
- Rowntree, P. A., Scoles, G., & Ruiz-Suárez, J. C. 1990. Low-energy helium scattering from ordered physisorbed layers of polar molecules. *J. Phys. C*, **94**(23), 8511.
- Ruiz-Suárez, J. C., Klein, M. L., Moller, M. A., Rowntree, P. A., Scoles, G., & Xu, J. 1988. Structure of physisorbed overlayers of dipolar molecules: a combined study by atomic-beam scattering and molecular dynamics. *Phys. Rev. Lett.*, **61**(6), 710.
- Salanon, B. 1984. Ne diffraction from Cu(110). *J. Physique*, **45**(8), 1373.
- Sánchez-Portal, D., Artacho, E., & Soler, J. M. 1996. Analysis of atomic orbital basis sets from the projection of plane-wave results. *J. Phys. Condens. Matter*, **8**, 3859.
- Scheffler, M., & Stampfl, C. 1999. Theory of adsorption on metal substrate. In: Horn, K., & Scheffler, M. (eds), *Handbook of Surface Science*, vol. 2. Amsterdam: Elsevier Science.
- Schiff, L. I. 1968. *Quantum Mechanics*. Third edn. Physics series. Singapore: McGraw-Hill.
- Schlüter, M., Chelikowsky, J. R., Louie, S. G., & Cohen, M. L. 1975. Self-consistent pseudopotential calculations for Si(111) surfaces: unreconstructed (1×1) and reconstructed (2 × 1) model structures. *Phys. Rev. B*, **12**(10), 4200.
- Schwegmann, S., Tappe, W., & Korte, U. 1995. Quantitative structure analysis of a disordered system: RHEED study of the CO induced (1×2) → (1×1) structure transition of Pt(110). *Surf. Sci.*, **334**, 55.

- Segall, M. D., Shah, R., Pickard, C. J., & Payne, M. C. 1996. Population analysis of plane-wave electronic structure calculations of bulk materials. *Phys. Rev. B*, **54**(23), 16317.
- Seyller, Th., Caragiu, M., Diehl, R. D., Kaukasoina, P., & Lindroos, M. 1999. Dynamical LEED study of Pt(111)- ($\sqrt{3} \times \sqrt{3}$) R30° -Xe. *Phys. Rev. B*, **60**(15).
- Sharma, R. K., Brown, W. A., & King, D. A. 1998. Adsorbed CO chain condensation and evaporation on Pt(110)-(1×2) at 30-70 K studied by RAIRS. *Chem. Phys. Lett.*, **291**, 1.
- Slater, J. C. 1974. *The Self-consistent Field for Molecules and Solids*. New York: Mc Graw Hill.
- Somorjai, G. A. 1994. *Introduction to Surface Chemistry and Catalysis*. New York: Wiley.
- Sowa, E. C., Hove, M. A. Van, & Adams, D. L. 1988. The missing-row model for the reconstructed Pt(110)-(1×2). A LEED intensity analysis showing multilayer distortions. *Surf. Sci.*, **199**(1-2), 174.
- Spanjaard, D, & Desjonquères, M. C. 1990. Electronic theory of chemisorption. *Pages 255-323 of: Bortolani, V., March, N. H., & Tosi, M. P. (eds), Interaction of Atoms and Molecules with Solid Surfaces*. New York: Plenum Press.
- Štich, I., R. Car, M. Parrinello, & Baroni, S. 1989. Conjugate gradient minimization of the energy functional: A new method for electronic structure calculation. *Phys. Rev. B*, **39**(8), 4997.
- Stokbro, K. 1996. Mixed ultrasoft norm-conserved pseudopotential scheme. *Phys. Rev. B*, **53**(11), 6869.
- Sutton, A. P. 1996. *Electronic Structure of Materials*. Oxford Science Publication. Oxford: Oxford University Press.

-
- Tappe, W., Korte, U., & Meyer-Ehmsen, G. 1997. RHEED structure analysis of the oscillatory catalytic CO oxidation at Pt(110) surfaces. *Surf. Sci.*, **388**, 162.
- Teter, M. P., Payne, M. C., & Allan, D. C. 1989. Solution of Schrödinger equation for large systems. *Phys. Rev. B*, **40**(18), 12255.
- Trioni, M. I., Montalenti, F., & Brivio, G. P. 1998a. Ab-initio adiabatic noble gas-metal interaction: the role of the induced polarization charge. *Surf. Sci.*, **401**, L383.
- Trioni, M. I., Marcotulio, S., Santoro, G., Bortolani, V., Palumbo, G., & Brivio, G. P. 1998b. *Ab initio* adiabatic He and Ne interaction on Ag: An all-electron calculation. *Phys. Rev. B*, **58**(15), 11043.
- Troullier, N., & Martins, J. 1990. A straightforward method for generating soft transferable pseudopotentials. *Solid State Commum.*, **74**(7), 613.
- Troullier, N., & Martins, J. 1991. Efficient pseudopotentials for plane-wave calculations. *Phys. Rev. B*, **43**(3), 1993.
- Vanderbilt, D. 1985. Optimally smooth norm-conserving pseudopotentials. *Phys. Rev. B*, **32**(12), 8412.
- Vanderbilt, D. 1990. Soft self-consistent pseudopotentials in a generalized eigenvalue formalism. *Phys. Rev. B*, **41**(11), 7892.
- Vanderbilt, D., & Louie, S. G. 1984. Total energies of diamond(111) surface reconstructions by a linear combination of atomic orbitals method. *Phys. Rev. B*, **30**(10), 6118.
- van't Klooster, P., Trappeniers, N. J., & Biswas, S. N. 1979. Effect of pressure on the elastic constants of noble metals from -196 to +25°C and up to 2500 bar. *Physica B*, **97**, 65.

- Vlieg, E., & Robinson, I. K. 1990. Relaxations in the missing-row structure of the (1×2) reconstructed surface of Au(110) and Pt(110). *Surf. Sci.*, **233**(3), 248.
- von Oertzen, A., Mikhailov, A. S., Rotermund, H. H., & Ertl, G. 1998. Subsurface oxygen in the CO oxidation reaction on Pt(110): Experiments and modeling of pattern formation. *J. Phys. Chem. B*, **102**, 4966.
- Wartnaby, C. E., Stuck, A., Yeo, Y. Y., & King, D. A. 1996. Microcalorimetric heats of adsorption for CO, NO, and oxygen on Pt{110}. *J. Phys. Chem.*, **100**, 12483.
- White, J. A., Bird, D. M., & Payne, M. C. 1996. Dissociation of H₂ on W(100). *Phys. Rev. B*, **53**(3), 1667.
- Whitten, J. L., & Yang, H. 1996. Theory of chemisorption and reactions on metal surfaces. *Surf. Sci. Rep.*, **24**, 55.
- Widdra, W., Trischberger, P., Friess, W., Menzel, D., Payne, S. H., & Kreuzer, H. J. 1998. Rare-gas thermal desorption from flat and stepped platinum surface: Lateral interactions and the influence of dimensionality. *Phys. Rev. B*, **57**(7), 4111.
- Wigner, E. 1933. On the interaction of electrons in metals. *Phys. Rev.*, **46**, 1002.
- Witte, G., Toennies, J. P., & Wöll, Ch. 1995. Comparison of surface phonon dispersion curves for clean and covered Rh(111) surface. *Surf. Sci.*, **323**(3), 228.
- Zaremba, E., & Kohn, W. 1977. Theory of helium adsorption on simple and noble-metals surfaces. *Phys. Rev. B*, **15**(4), 1769.
- Zeppenfeld, P., Cosma, G., & Barker, J. 1992. Critical analysis of the possible experimental evidence for an on-top adsorption site for xenon on Pt(111). *Phys. Rev. B*, **46**(14), 8806.

Zhang, & Yang. 1998. Comment on “generalized gradient approximation made simple”. *Phys. Rev. Lett.*, **80**(4), 890.

Zhang, Y., Pan, W., & Yang, W. 1997. Describing van der Waals interaction in diatomic molecules with generalized gradient approximations: The role of the exchange functional. *J. Chem. Phys.*, **107**(19), 7921.